AGARDograph 113

AGARDograph 113

AGARD

ADVISORY GROUP FOR AEROSPACE RESEARCH & DEVELOPMENT

Free-flight testing in high-speed wind tunnels

by Bain Dayman, Jr

★

MAY 1966

AGARDograph 113

NORTH ATLANTIC TREATY ORGANIZATION

ADVISORY GROUP FOR AEROSPACE RESEARCH AND DEVELOPMENT

(ORGANISATION DU TRAITE DE L'ATLANTIQUE NORD)

FREE-FLIGHT TESTING IN HIGH-SPEED WIND TUNNELS

by

Bain Dayman, Jr

Jet Propulsion Laboratory,
California Institute of Technology,
Pasadena, California, USA

This is one of a series of publications by the NATO-AGARD Fluid Dynamics Panel.
Professor Wilbur C. Nelson of The University of Michigan is the editor.

SUMMARY

The adaptation of free-flight techniques to testing in a conventional wind tunnel was made operational recently at the California Institute of Technology Jet Propulsion Laboratory. This AGARDograph describes this technique in enough detail that it can be applied to other facilities with a minimum amount of development. Examples and results of many applications are included in order to demonstrate the need and advantages for using this free-flight technique.

RESUME

L'adaptation des techniques de vol libre aux essais en tunnel aérodynamique a atteinte l'état de marche au California Institute of Technology Jet Propulsion Laboratory. L'AGARDograph ci-dessous présente la technique en detail suffisant pour qu'on peut l'appliquer à d'autres installations avec une mise au point minimum. On a donné des exemples et les résultats des applications diverses afin de démontrer la nécessité et les avantages d'emploi de cette technique en vol libre.

533.6.055:533.6.071

CONTENTS

Page

LIST OF TABLES

LIST OF FIGURES

Page

NOTATION

a	model acceleration
A	model reference area = $\frac{1}{4}\pi d^2$
b_i	non-linear coefficients in C_L
cg	center of gravity
c_i	non-linear coefficients in C_D
C_D	local drag coefficient = drag/qA
C_{DD}	drogue drag coefficient (based on drag area)
$C_{D\ eff}$	effective drag coefficient of an oscillating model
C_{D0}	total drag coefficient at zero angle of attack
C_L	local lift coefficient = lift/qAd
$C_{L\alpha}$	lift slope at zero angle of attack (per radian)
C_m	local pitching moment coefficient = (pitching moment)/qAd
$C_{m\alpha}$	pitching moment slope at zero angle of attack
$(C_{m\alpha})_{eff}$	effective pitching moment slope of an oscillating model
$C_{mq} + C_{m\dot{\alpha}}$	effective dynamic damping coefficient (assumed constant during a cycle of oscillation) = $\left[\frac{\partial C_m}{\partial \dot{\theta}} + \frac{\partial C_m}{\partial \dot{\alpha}}\right] \frac{V_\infty}{d}$
$(C_{N\alpha})_{eff}$	effective normal force slope coefficient (per radian) of an oscillating model = (normal force slope)/qAd
d	model base (reference) diameter
E	Legendre canonical form of the elliptic integral of the second kind
f	frequency of oscillation (cycles per second)
F	Legendre canonical form of the elliptic integral of the first kind
g	acceleration due to gravity
I	model moment of inertia
I_c	calibrating body moment of inertia

k	=	$-\dfrac{\rho_0 r_m}{C_{m\alpha} + r_m \rho_0^2}$
K		wire torsional constant
l		model length
m		mass of free-flight model
M		freestream Mach number
M_D		dynamic damping term $= (C_{mq} + C_{m\dot{\alpha}})\, qA \dfrac{d^2}{V_\infty}$
M_S		static damping term $= (C_{D\ eff} - C_{L\alpha})\, q \dfrac{A}{V_\infty}$
N		number of oscillation cycles
p_B		base pressure
p_∞		freestream static pressure
p_0		freestream total pressure
P_0'		pitot pressure
q		freestream dynamic pressure
r_c		ballast core radius of hypothetical spherical shape
r_m		non-linear coefficient in C_m
r_s		outside radius of hypothetical spherical shape
r_B		base radius of cone model
r_N		nose radius of spherical blunted cone model
R		correction factor for non-linear pitching moment effect on reduction for dynamic stability coefficient
Re		freestream unit Reynolds number
R_d		freestream Reynolds number based on model diameter
S		length of useful trajectory of free-flight model
t		time

T_0	freestream stagnation temperature
T_w	model wall temperature
T_∞	freestream static temperature
V	model longitudinal velocity relative to freestream
V_m	model longitudinal velocity relative to ground
V_∞	freestream flow velocity relative to ground
W	weight of free-flight model = mg
x	longitudinal location of model relative to ground
x_{cg}	center-of-gravity location (from nose of model) $()_M$ measured; $()_{th}$ calculated
x_{cp}	center-of-pressure location (from nose of model)
X	distance model travels longitudinally relative to freestream
X_0	value of X at some arbitrary initial condition
X_L	distance X for one quarter oscillation cycle (linear pitching moment)
X_N	distance X for one quarter oscillation cycle (non-linear pitching moment)
y	lateral location of model relative to ground
Δy	peak-to-peak model swerve motion
α	angle of attack
α_{env}	angle-of-attack oscillation envelope
α_0	initial oscillation envelope
$\bar{\alpha}_0$	effective oscillation envelope
α_t	angle of attack oscillation envelope at time t
α_x	angle of attack oscillation envelope at distance x
δ^2	root-mean-squared angle of attack
θ	angle between freestream velocity vector and model centerline
θ_0	θ at arbitrary initial condition $(X = X_0)$. Also, equivalent to $\bar{\alpha}_0$

$\delta\theta$	amplitude decay during a half cycle of oscillation
ρ	gas freestream density
σ	cone apex half-angle
$\overline{\chi}$	hypersonic viscous interaction parameter based on cone surface conditions and model length = $M_c^3(C_c/R_{lc})^{\frac{1}{2}}$ where C_c is the Chapman-Rubesin coefficient, and $()_c$ represents cone surface conditions
ψ	angle of yaw
Ω	distance oscillation frequency; radians (2π cycles) per unit distance (X) of model travel
$(\dot{\ })$	derivative with respect to time
$(\ )'$	derivative with respect to distance

FREE-FLIGHT TESTING IN HIGH-SPEED WIND TUNNELS

Bain Dayman Jr

1. INTRODUCTION

The need for and the advantages of support interference-free aerodynamic data has been recognized from the very start of aerodynamic testing. Also, the attainment of realistic model motion during free-flight trajectory has always been an important requirement. As flight vehicles become more complex and expensive, the greater becomes the need for a better understanding of the factors which go into the design of the actual vehicle and the manner in which they affect its predicted performance. Consequently, a great deal of effort has been put into observing the motion of bodies having all six-degrees-of-freedom and obtaining valid interference-free data.

During the past four years at the Jet Propulsion Laboratory, a considerable amount of effort has been put into developing the techniques of free-flight testing in conventional wind tunnels and the acquisition of useful quantitative data. A conventional wind tunnel is defined as a tunnel having starting times in the order of a second and run times of at least several seconds. In order to explain the reasons for this development program, it would be useful to give a brief chronological description of free-flight testing over the years.

Both internally- and externally-mounted stores have been dropped from supported models during subsonic wind tunnel tests for many years. The free-flight motion of these stores was studied with the aid of medium-speed movie cameras. Attempts were made to obtain quantitative data from setups which were essentially qualitative in nature. Nevertheless, a better understanding of the store-drop problems was achieved which aided the development of techniques for successful release of stores from full-scale aircraft. There is no doubt that this use of the free-flight technique was essential for minimizing both the cost and time in arriving at the final satisfactory design.

Many subsonic vertical wind tunnels[1,2*] have been used for model spin tests and recently for dynamic stability studies on several re-entry shapes with and without trailing devices such as drogue parachutes. The spin tests were a powerful tool in developing and proving the design of airplanes.

However, it was in the ballistic ranges[3-6] that the large variety and high quality of data retrieval techniques were developed from free-flight models in ground-based facilities under controlled conditions. In addition to the aerodynamic coefficient

* Reference 2 contains references to several vertical spin tunnels and to many other free-flight testing techniques

data (drag, lift and pitching moment slope, and dynamic stability), information was obtained on the wake structure[7]. This wake information (ablation, transition, diffusion, electrical properties, etc.) is being obtained currently in specialized facilities[8-10].

Shock tunnels[11,12] are also used to measure drag and static stability derivatives. Low Reynolds number drag information at high Mach numbers has been obtained in both arc-discharge tunnels[13,14] and in a low-density hyper-velocity wind tunnel[15]. Movies have been made of vehicle motion characteristics when dropped from airplanes. Actual flight tests[16], dependent mainly upon internal instrumentation, have produced a large quantity of valuable data, but usually of below-desired quality. The information gained per dollar is extremely low compared with that from ground-based facilities, and the time scale is not only large, but unpredictable. Nevertheless flight data are valuable for purposes of validation. Sometimes, it is the only way to obtain certain information because it is impractical or even impossible to simulate the necessary conditions in ground-based facilities.

Recently a new approach to obtaining actual flight data made use of the "sky-diving" technique. The motion of spheres dropped from an airplane was studied by a sky-diver filming the descent from close range[17]. Until parachute deployment, the sky-diver has considerable control over both descent velocity and lateral position.

The use of magnetic suspension as a technique for obtaining interference-free data in a wind tunnel, was initiated quite some time ago[18,19]. Recently, the capability of this technique has been extended from only drag measurements to lift and static stability[20,21]. Pressure measurements[22,23] are made on magnetically supported models as well as wake characteristics studies[24].

The free-flight technique as presented in this report was successfully employed[25] as early as 1954. Here simple models (from which drag measurements were made) were blown out of tubes against the airstream in a vertical supersonic wind tunnel. The high-speed wind tunnel free flight testing technique is intended only to complement the many other interference-free and supported-model testing methods. Also, it serves to validate or show limitations in the information obtained in wind tunnels with supported models. This, in itself, is a very valuable capability.

2. DESCRIPTION OF MOTION STUDIES*

2.1 Detailed History During One Cycle of Oscillatory Motion

A description of the data obtained from a model during one complete cycle of oscillation serves as an introduction to the many basic types of vehicle motion studies that are practical in a conventional wind tunnel. Both the angle of attack and velocity can be precisely determined by the use of high-speed (5000 frames/sec) motion pictures.

Although the model can be gun-launched, the use of the wire-release technique is usually satisfactory. The model size should be fairly large in order to obtain a

---

* Some expressions used in this section may be unclear. They will be defined in later sections during the discussion of specific aspects of the free-flight techniques

relatively large film image and to limit (by means of a low ratio of mass to moment of inertia) the oscillation to slightly more than one complete cycle. In this manner, some 300 separate frames of model motion during one cycle of oscillation can be obtained. Very detailed analysis during a small portion of the trajectory can be made. The angle of attack can be measured to about ±0.1 deg and the model location to about 0.1% of model length. An example of an angle-of-attack history[26] is shown in Figure 1(a). Note should be taken of the negligible data scatter. The picture quality obtainable is shown in Figure 1(b).

By spinning up the models prior to gun-launch, the models can be given desired rate of roll about the axial centerline. In this case, it is necessary to record the model motion in the horizontal plane, as well as the usual vertical plane. In general, when the models are not specifically given roll rates, their motion is contained entirely in the vertical plane, and pictures of one plane are adequate.

2.2 Drag Studies

The presence of a sting support affects the model base pressure. At low Mach numbers, the base pressure can be a substantial portion of the total drag, especially for low form-drag models. Thus, under an appreciable range of testing conditions, it becomes virtually impossible to measure the total drag of certain models accurately (say, within ±2%) when they are supported on a sting. For purposes of illustration, Table I indicates the importance of the base-pressure drag on several cones. For simplicity, skin friction was neglected. The base pressure was taken as one-half the freestream pressure; this is not exactly the actual case, but is probably within a factor of two of the usual condition. These are certainly adequate assumptions to point out the importance of an error in the base pressure when correct total drag is a test requirement.

It is readily apparent that a 10% error in the base pressure, which can be a realistic situation because of sting interference, can cause a significant error in the total drag at the lower Mach numbers. The base-pressure effect on total drag is considerably more serious, and extends further into the higher Mach number region as the cone becomes more slender.

2.2.1 Zero Angle of Attack

Figure 2 shows a typical actual size film image and an enlargement of a cone model used for drag data. Examples[28] of free-flight cone drag data appear in Figure 3(a) (the effect of Mach number) and Figure 3(b) (the effect of nose bluntness). Because of their relatively high acceleration, it was not practical to use the simplified ds/dt versus t approach in making the drag measurements. The $\log_e (1 + V_m/V_\infty)$ versus X approach[29] is required because of the substantial variation of dynamic pressure on the model during the free-flight trajectory. Figure 4 demonstrates the linearity obtained from the drag data reduction using this more universal method. Figure 5 shows an example for drag reduction when the model has low (< 10 g) acceleration.

2.2.2 Oscillatory Motion

In many cases, drag is required from oscillating models. For slender models, the drag can be a strong function of angle of attack. In order to obtain the average drag during one oscillation cycle, it is desirable to analyze the linear motion during several complete cycles. This permits considerable relaxation of the position measurement requirements. For example, the model axial location need be measured only at zero angle of attack. The design of the models should be such that the oscillation amplitude is essentially unaffected by the various factors contributing to decay (lift, drag, and dynamic damping). This allows for extremely simple data reduction without compromising final data accuracy. Of course, the suggested design requirement is not a necessity; but if deviations (i.e., the amplitude of oscillation varies during trajectory or the model has high acceleration) do occur, the simplified approach to data reduction may not be adequate. This is not necessarily a disadvantage, because a slight complication in the data reduction may be more than offset by the simplification of model design or the ability to obtain a wider variety of data during a single trajectory. The variation of velocity with angle of attack is quite noticeable in Figure 6, where the velocity is compared with the local angle of attack.

The drag at zero angle of attack may be deduced from the total average drag at several amplitudes of oscillation in a manner similar to that used in ballistic ranges; the total drag is a linear function of the square of the oscillation envelope and, hence, the data may be extrapolated to zero angle.

2.2.3 Decaying Oscillatory Motion

Trajectories of slender models designed especially for dynamic stability studies are expected to have substantial decay in the oscillatory envelope and consequently will have a large variation in the average drag from the beginning to the end of the flight. The effective average drag coefficient as a function of some particular angle-of-attack amplitude is not the ultimate in accuracy, but drag as a function of several angle-of-attack amplitudes can be obtained during a single flight[30]. The variation of $\log_e (1 + V_m/V_\infty)$ with X (and amplitude) is shown in Figure 7 and the resulting total drag coefficients for this type of trajectory is shown as a function of the square of the angle-of-attack envelope in Figure 8.

2.2.4 Low Reynolds Number

The accurate measurement of drag at low Reynolds numbers is extremely complicated due to the magnitude of the force involved. It is difficult to build, maintain, and successfully use appropriate balances. However, by free-flighting small models (as small as 0.05 in. D, or even smaller for spherical models) at low tunnel dynamic pressures (about 0.1 lb/in.^2 abs.), it is practical[31] to measure drag levels down to 10^{-4} lb to within ±2%. Figure 9 presents a drag study of slender cones at low Reynolds numbers.

Interference effects on the base pressure due to the presence of a sting support is normally expected. An example of such an interference appears in Figure 10. An increase in the ratio of the sting to model base diameter from 0.25 to 0.50 doubles the base pressure for this particular case. It is possible that the most significant effect of the sting interference is not limited to the base area. As the boundary-layer thickness on cones in low Reynolds number flow can be on the order of the model radius, a pressure disturbance on the base may feed forward through the subsonic portion of the thick boundary layer and consequently distort the boundary layer on the cone surface. The magnitude of the resulting effect on drag and stability data has not yet been determined. This effect should not be assumed to be negligible until so demonstrated.

A similar situation exists in the use of low density wind tunnels where the boundary-layer thickness may be about half of the nozzle radius. Any variation in the test chamber (plenum) pressure affects the nozzle exit Mach number[32]. The only way that this could occur would be for the pressure variation to feed upstream into the nozzle through the subsonic portion of the boundary layer and change its characteristics. A change in Mach number from this cause is shown in Figure 11.

2.2.5 Undistorted Configuration

In order to study airplane configurations experimentally in wind tunnels, it is usually necessary to alter the basic shape in the region of the base to accommodate a sting support and balance (Fig. 12). The effect of this alteration can be studied by the use of the free-flight technique. Another similar problem is the study of boat-tailing effects on drag. In many instances, this study is limited by the presence of the sting and the housing of the balance. Consequently, the desired variation of the boat-tailing cannot be achieved. This problem, which also applies to pitching moment studies, can be solved by free-flight testing.

2.3 Static Stability Studies

2.3.1 Basic Static Stability

The one cycle angle-of-attack history of Figure 1(a) can be used to obtain pitching-moment slope data. The large number of accurate data points may even permit the determination of the local pitching moment throughout the angle-of-attack oscillation. An even higher degree of accuracy for the effective pitching moment slope can be achieved by having several complete cycles of oscillation recorded during the trajectory. Rather than requiring an extremely careful curve fit to the single cycle of data, only the times (or distances) at several successive zero angles of attack are then needed. Figure 13 shows a typical example of non-decaying angle-of-attack history for a model having over five cycles of oscillation. The effect of oscillation amplitude on the pitching moment slope[30] appears in Figure 14.

The models designed for free-flight testing in a wind tunnel usually do not swerve (vary in a lift direction away from a zero-lift trajectory) enough to determine accurately the lift-curve slope as is typically done in a ballistic range. But, by placing the center of gravity at several locations, the center-of-pressure location, as well as the normal force slope, can be determined[31] (Fig. 15).

2.3.2 Low Reynolds Number

As with the measurement of drag at low Reynolds number, there is considerable difficulty in developing and using balances for measurement of very small magnitudes of pitching moment. Effective pitching moment, as deduced from the oscillation frequency, can be measured for values as low as 10^{-5} in.lb to within 5%. Figure 15 is an example of such data, the smallest r.m.s. moments measured being about 1.5×10^{-4} in. lb.

2.3.3 *Effects of Hysteresis*

Some shapes have flow characteristics which may be a function of the angle of attack and the motion history. Separation ahead of a step or a flare is a typical example of such flow. Ablation and mass injection can also have a significant effect on flow over a body. At low Reynolds numbers, the boundary layer ahead of a flare (Fig.16) is likely to be separated[33,34]. The amount of separation at a particular angle of attack may depend upon the direction in which the angle is approached, and at what rate.

One way of investigating the effect of boundary-layer separation hysteresis on static stability is the free-flight technique, where the pitching moment slope can be determined to within 2%. The oscillation amplitude can be controlled, and the oscillation frequency can be varied.

2.3.4 *Lifting Bodies*

It is practical to study the motion of a lifting body by the use of the free-flight technique in a conventional wind tunnel. It is not particularly important whether the trajectory is longitudinal (as with a zero-lift body) or lateral. In either case the motion can be adequately photographed on high-speed movie film. However, for the lifting body, the use of a full-frame rather than half-frame camera is required as the entire viewing area (not just the horizontal center-line region) must be recorded. The lifting body can be wire released. A possibly more satisfactory method would be to employ some sort of a simple, quick-release model holder located at the floor of the test section. The shock waves from such a device would not intersect with the crucial region of the model trajectory except at low Mach numbers or low lift-to-drag ratio bodies. This technique permits direct measurement of the interference-free trim angle, lift-to-drag ratio, and drag.

2.4 Dynamic Pitch Damping

Although it may be practical to measure dynamic damping at high amplitudes of oscillation by using models cross-supported on gas or mechanical (ball or roller) bearings, the effect of the disturbances caused by the support is not always negligible. In such cases, it is necessary to rely upon the free-flight technique for such data in order to at least establish a confidence level for the supported model. Many damping studies have been made for oscillation amplitudes up to 90 deg and a few up to 150 deg. In Figure 17 are shown two cases of damped motion at high amplitudes of oscillation; one is for a model having very small and the other (slender cone) having fairly large dynamic stability damping. Figure 18 gives some typical results[30] of the damping coefficient for a 10-deg half-angle sharp-nose cone at moderate angle-of-attack envelopes.

The practicality of this technique for obtaining dynamic damping in pitch can be illustrated by describing hypothetical results for two extremes in model design: Model A (minimum radius of gyration) – light-weight foam shape, ballasted with a gold sphere at the center of gravity; Model B (maximum radius of gyration) – thin-shell aluminum shape, ballasted at the forward tip with gold. The hypothetical model and test conditions are as follows:

σ = 10 deg (cone half-angle)

r_N/r_B = 0 (sharp nose)

cg at 50% of model length

α_0 = 0.1 rad (initial angle-of-attack amplitude)

S = 2 ft (length of wire-release trajectory)

M = 8

V_∞ = 3880 ft/sec (900°F supply temperature).

For models with varying base diameters, the trajectories of the two methods of construction are compared in Table II. Also, the effect of an order of magnitude in the tunnel dynamic pressure on the ½ in. D Model A is shown. In all cases, the dynamic-damping effect on the amplitude is based upon an assumed value of $C_{mq} = C_{m\dot{\alpha}} = -2$. Low radius of gyration and high tunnel dynamic pressure are important requirements for the measurement of dynamic damping. For gun-launched models, having trajectories in both directions across the viewing area, the values for t and N are doubled, and the values for $(\alpha_t/\alpha_0)_{env}$ are squared.

2.5 Flow Discontinuity Effects

The effect of flow non-uniformities, such as a gust or a nuclear blast upon the motion of a vehicle, can be studied in detail. A pressure-gust can be simulated in a wind tunnel by the use of a flow-turning wedge. The effects of small pressure disturbances on free-flighted cones have been observed. A nuclear blast condition could be created by use of "electrically exploding" wires, an explosive charge, or by aiming a shock tube at the wind tunnel model trajectory region.

2.6 Multibody Studies

Definitive experimental studies of the motion of bodies while in the aerodynamic influence of other bodies are virtually non-existent. The use of free-flight techniques makes it practical to study the motion of conditions such as: removal of base cover on re-entering vehicles; separation of launch vehicle stages; flight of a salvo of closely spaced missiles. An example of the motion of two closely spaced, gun-launched slender cones is shown in Figure 19.

One simple device[35] that can be used to separate a tandem configuration (two models in series) while in free-flight is shown in Figure 20(a). The rod is free to slide within the forward spherical ballast. The vertical wire used for wire-launch goes through the ballast sphere and through a hole in the left-hand end of the rod. In this position the rod is in a forward position, thus forcing the wire fingers together. The trailing cone is centered on the right-hand end of the rod with the fingers squeezed into holes on the cone nose. In this manner, the trailing cone is held in position against the base of the forward cone. When the vertical wire breaks within the forward model, the rod springs aft due to the spring-action of the fingers, allowing the models to separate. A flight example of the separation of these tandem cones is shown in Figure 20(b).

2.7 Drogued Configurations

Up to now, the motion study of drogued configurations has been hampered by the effects of support interference (see Figure 21 for an example of the severe shock wave patterns caused by a single small transverse wire support) and the lack of complete motion simulation. Both simple drag studies and the more complicated motion studies of drogued configurations have been carried out[36]. An example of the effect of a small drogue body upon the angle-of-attack history of the main (forward) body is shown in Figure 22. The drag of a trailing sphere without support interference is shown in Figure 23.

2.8 Base Measurements

The presence of any type of support has been shown to affect model base pressure and heating. Much of the theoretical work being done in this field also lacks definitive experimental data. With the free-flight models, telemetry is relatively simple because of the low accelerations (< 100 g). A variety of releases, including gun-launch and wire-release, can be used. Examples of base pressure data obtained by the wire-release[37] and the gun-launch[38] are shown in Figure 24.

2.9 Wake Studies

2.9.1 Optical

Two techniques are practical for obtaining schlieren pictures of free-flight model wakes. For non-oscillating models (which, for this purpose, are wire-released into their trajectory), one 4 in. × 5 in. spark schlieren photograph can be taken per flight. For the JPL optical system the model image size is quite large, about 1/6 actual size. Examples of such wake schlierens[39] are in Figure 25. However, since the spark technique is not practical for an oscillating model, use is made of high-speed schlieren movies on 35 mm half-frame film. In this case, the film image is about 1/30 actual size. A schlieren sequence of an oscillating cone wake taken on high-speed (4000 frames/sec) 35 mm film[30] is shown in Figure 26. In spite of the small model film image (0.03 in. base diameter), the resolution is surprisingly good. Model diameters up to 3 in. have been used in order to improve the definition and increase the number of pictures per cycle.

It has been customary to support a model from the side, rather than from the base, in order to observe wake properties. Under most conditions, this is not a satisfactory approach for such data. Comparisons[40] of cone wakes with and without single-transverse wire support (0.020 in. D wire for 1.5 in. D cone) are shown in Figure 27. At $M = 2$, when the wake of the free-flight cone appears to be turbulent, the presence of the wire support has negligible effect on the wake shape; at $M = 4.7$, the wire substantially alters the laminar wake*. A similar wire interference effect,

* It should not be assumed that the presence of a wire has no effect on a turbulent wake just because there is no major effect on the schlieren-observed wake shape. Detailed pitot and static pressure probing in the wakes of large cones with turbulent boundary layers at $M = 4$ indicate appreciable differences in the pressure profile between those taken in the plane of the supporting wire and cross-wise to the wire[41]. The wire diameter was 0.7% of the model base diameter. The optical wakes of these wire-supported models compared favorably with the equivalent free-flight wakes.

movement of the wake neck toward the model, has been noticed for sphere models. The variation of the sphere wake neck location with wire diameter is shown in Figure 28. The schlieren pictures indicate that the flow field in the plane of the wire support has no obvious major disturbance due to the wire. But, as can be seen in Figure 21, the flow field in the plane normal to the wire support is severely disturbed by the presence of the wire. Hence, it is not surprising that a seemingly insignificant wire support can materially alter the wake shape.

The effect of model ablation on the free-flight wake can be conveniently studied. The use of low temperature ablators such as carbon dioxide or "moth balls" permit sufficient variation in the mass ratio for meaningful studies. Even intricate models capable of ejecting gas through the surfaces are feasible.

2.9.2 *Surveys*

Pressure surveys, and perhaps temperature or hot-wire surveys can be made through the wake of a free-falling, heavily ballasted model. Two-inch diameter, lead-filled aluminum cones weighing several pounds have been dropped, and near-vertical pitot pressure surveys have been made through the wake at various stations aft of the base. This technique will give realistic, interference-free measurements at locations considerably downstream of the wake neck. How close to the base such probing can be done must be carefully investigated for each particular case (model shape, Mach and Reynolds numbers, probe geometry, etc.). Two methods are available to assess the degree of interference. Recourse may be made to the use of high-speed 35 mm film schlierens and/or the history of the telemetered base pressure as the model drops down and its wake becomes clear of the probe.

The pressure probe can be designed for a response time on the order of 1-2 millisec. As the vertical travel is only 0.08 in. during 2 millisec after the model has already dropped two inches, this lag time is acceptable. An example of a pressure survey through a cone wake[42] is illustrated in Figure 29. This free-fall technique is very useful when the axial acceleration is less than the acceleration due to gravity, but becomes less productive as the model axial acceleration increases.

3. MODEL LAUNCHING

3.1 General

For free-flight testing in conventional wind tunnels, the models can be launched into free-flight trajectories in several ways. The two most common techniques are wire-release and gun-launch. Another technique which has important advantages, as well as severe limitations, consists of dropping the model through the flow. Additional techniques are used for both specialized and general applications at other facilities.

3.2 Wire-Release

The model can be supported on a wire strung across the test section at the forward end of the viewing area[43]. Normally the wire is in the same plane as the windows. If it is desired to have a wire support in a plane orthogonal to a window, either of two cautions must be observed. The window must be recessed from the flow or protected in some manner such that the ruptured wire will not come in contact with the window, for if it does, damage to the window may occur. This window damage can be prevented by substituting monofilament string for the wire, such as 0.040 in. diameter fishing line. It is necessary to knot the string inside the model in order to create a stress point; when an impulse load is added to the normal tension load, the string will break within the model.

The wire normally used for launching is piano wire ranging from 0.008 to 0.026 in. diameter, notched on one side only to a depth of 0.003 to 0.007 in. at a point within the model. Should the stagnation temperature be above 300°F, it is preferable to use a high-temperature steel wire. Although the piano wire has a higher yield strength at room temperature, at elevated temperatures it is substantially weaker than the high-temperature steel wire. At stagnation temperatures above 1000°F, and when the heat input to the wire is high enough to cause the wire to break at its intersection with the model bow shock wave, it is necessary to use a hollow-tube (e.g., 0.036 in. diameter, 0.006 in. wall thickness, and a 0.001 in. circumferential notch), which is internally cooled with either water or some gas such as nitrogen or air.

A shield can be used to cool a model which is located in a flow having a high stagnation temperature. This wedge-shaped shield can encompass the model, but can even be located entirely upstream of the model. Gaseous nitrogen ejected from this shield over the model will cool the model down to about 0°F. Liquid nitrogen ejected over the model will cool the model to approximately -320°F. The shield is rapidly removed from the flow just prior to model launch. The depth of the notch on the wire or tube must be increased in order to retain a proper strength balance of the wire between the cooled notch region and the remainder of the wire which is at a higher temperature. If this is not done the notch may be the strong point, and the rupture of the wire will occur at another location.

Table III lists several wire-tunnel conditions which have been proven to be operational at JPL. It will serve as a basis for incorporating such a launch technique without an undue amount of development.

A typical wire-launch installation is shown in Figure 30. A shield, from which either liquid or gaseous nitrogen can be ejected over the model for cooling purposes, is shown in the down position. This shield can be raised completely out of the flow in 0.1 to 0.2 seconds. The wire tension and the impulse load to rupture the wire is generally applied in either of two methods. Originally weights were used to preload the wire and then additional weights were dropped (about 6-8 in.) in order to supply the impulse load. The current method uses a pneumatic piston for both the tension preload and the wire-breaking impulse load. An example of a wire-release model flight is shown in the high speed movie sequence of Figure 31.

It is not necessary to rupture a support wire by the use of tension acting at a pre-determined stress point. Another very satisfactory method would be to explode the wire, or at least a limited region of it, by using electrical energy. Controlled wire rupture by the use of electrical energy at a desired region (pyro-fuse) has been successfully developed by Lockheed-California Company[44] for use in a shock tunnel. This technique can be readily adapted to conventional wind tunnels.

3.3 Gun-Launch

The resulting trajectory of a wire-launch model is once across the viewing area in a downstream direction. By launching a model upstream against the air flow, both an upstream and a downstream trajectory across the viewing area are obtained. To optimize the information from such a trajectory, the model must be propelled to the upstream edge of the viewing area. A trajectory which goes considerably forward of the window usually penalizes the quality of the data. A trajectory which is too short generally penalizes the data a lesser amount.

Several means can be used to propel the model forward into the test section. Consideration was given to a "pelton-type" revolving launch wheel. This, however, would require a great deal of room and a considerable degree of precisely timed actuating mechanism. Therefore, it was discarded. The use of some type of launch gun seemed to be more appropriate: pneumatic power was chosen over several other approaches such as spring or gun-powder.

The design criteria used for the pneumatic launcher are as follows:

(i) The launcher had to be able to propel the model from a point downstream of the viewing window to the upstream edge of the window (a distance of approximately 34 in. in the JPL supersonic wind tunnel).

(ii) The angle of attack at release could be set from 0 to 180 deg for both slender models and for short, blunt models.

(iii) The mass of the models could vary from ½ to 100 grams.

(iv) Since the trajectory is determined by the model shape, mass, and tunnel dynamic pressure, the launch velocities must vary from 10 to 150 ft/sec.

Because of the structural geometry of the supersonic wind tunnel, the pneumatic launcher assembly was mounted 3 in. to the side of the tunnel centerline. In order to compensate for the gravity effect and maintain the model's flight as near centered in the viewing window as possible, the assembly was mounted 2 in. above the tunnel centerline. An alternative method would be to tilt the gun upward several degrees. The model separated from the launcher 7 in. downstream of the trailing edge of the viewing window. This was done to insure that the near-wake of the model would be free from any influence of the projecting mechanism.

In general the model is mounted on the launcher at the desired angle of attack and is secured by a set of fasteners or holding device[45] while tunnel flow conditions are established. An installation of a model at 20 deg angle of attack is shown in Figure 32. A cam-actuated micro-switch coupled to the fastener or holding device shaft, opens the holding device and also starts a high-speed camera. An event switch, synchronized with the camera, actuates the piston release mechanism approximately one quarter of a second later, starting the model on its way. This delay is necessary to allow for the high speed camera reaching the selected speed of 5000 frames/sec before the model appears in the viewing area. The picture sequence in Figure 26 shows the flight of a model released at positive angle of attack. As many as thirteen complete cycles of oscillatory model motion in a given flight have been filmed using this technique.

The original launch system supported the model on a piston-sabot within the launch tube and projected the models at 0 deg angle of attack only. Examination of the high-speed movies indicated that the models were being influenced by the bow shock of the launch tube and would pitch or yaw as they passed through this shock. To correct this, the supporting piston-sabot combination was extended to release the model upstream of the bow shock from the launch-tube. Another problem was a resonant-air condition in the interior of the tube which at times could blow the model off the support before launch if it was not firmly held in position. This approach was abandoned in favor of supporting the models in the airstream, as shown in Figure 32. Modifications were also made in the method of releasing the piston. This included an air-actuated auxiliary piston in conjunction with the launch tube.

Development was concentrated next to the support and release of the models at discrete angles of attack. The difficulties encountered in supporting the model at angle of attack, for instance, were shock interference from adjacent tunnel structure and a force-moment couple during the acceleration phase. Both of these problems were solved with the use of a triangular-shaped blade, placed on the launch gun rod (Fig.33). This type of support gives maximum side-load resistance to shock waves from the diffuser centerbody leading edge. This centerbody is a slender, metal plate spanning from the tunnel floor to the ceiling, along the length of the contraction section. The same support also resists the vertical-force couple by extending into the plastic model and holding it firmly in place. Figure 33 illustrates the triangular support which was used for angles of attack that varied from 0 to 30 deg. While this method of supporting is adequate for cones, other model shapes may require further support development. It was found that it is not absolutely necessary to recess the model when launching with the pneumatic gun. The model can be held on a concave support and launched against the airstream in a manner similar to that used by a shot-putter. In this case the model is held against the form-fitted support with a rubber band or nylon string. This tie is then cut by a razor blade when the launch-stroke is about at the half-way point. The model is free to release itself from the launch tube at the end of the stroke. Although it is convenient to launch models in this manner up to angles of attack of 120 deg, yaw motion is likely to be introduced in addition to the planned pitch motion. Then pictures taken in two planes (ideally orthogonal) are required to reduce the data during the trajectory. The recessed models very rarely have non-planar trajectories. That is to say, the motion is confined to the vertical plane for releases up to 90 deg angle of attack.

In order to prevent the model holder from rotating about the launch tube axis during the launching, the tube was fabricated from square tubing. The piston was then made to seal by incorporating vacuum-formed square cups of polyethylene sheet plastic. The various sections of the pneumatic launch tube are shown in Figure 34. The drive-piston packing seals off the exhaust ports near the end of the stroke, which is accompanied by an increase of pressure in the tube. A combination of a pneumatic dash pot and a coiled spring is used to stop the acceleration rod*. This system is effective in decelerating the piston and rod assembly within 1 in. (from a velocity of 100 ft/sec to rest). This deceleration has been adequate for most models tested.

Bench calibrations have been performed to evaluate the system's repeatability at various piston-supply pressures. The calibration equipment consists of two

---

* This rod is actually a hollow-tube in order to minimize the mass which must be decelerated at the end of the stroke

photo-multiplier tubes, light sources, and an oscilloscope. The plotted data of supply pressure versus velocity are shown in Figure 35, with an insert of a typical trace from the oscilloscope. With this information, it is possible to predict the pressures required to project the models at desired velocities. A first approximation (which neglects friction) for the required pressure is based upon the equations of motion, Section 4.2, using the model's velocity (V_m):

$$P = \frac{V_m^2 (m + m_1)}{2S_1 A_1} , \tag{1}$$

where A_1 = area of launch-tube piston

m = mass of free-flight model

m_1 = mass of launch-tube accelerating parts (piston, rod, model holder)

S_1 = length of launch-tube piston stroke.

In order to utilize the wind tunnel more efficiently, several launch assemblies can be installed, thus allowing two or more launches per tunnel entry. A remote-loading launch gun may be preferable. The wind tunnels at the Ballistic Research Laboratories use a gun incorporating a technique for landing several models during a single tunnel entry[46]. At Arnold Engineering Development Center (AEDC) a launch gun has been developed which can be retracted from the tunnel flow to be reloaded with a model without interrupting the flow[47].

3.3.1 Spinning Models

Models can be gun-launched with desired roll rates[48]. Cone models have been launched with spin rates up to 200 revolutions per second. Substantially higher rates have been demonstrated during bench tests but have not yet been required for actual model tests. Initial angles of pitch at launch have varied from zero to 30 deg. Launch success is not decreased by the incorporation of spin.

Spin is achieved by an air-driven motor. This small motor (about 1 in. D by 1 in. long, mounted on the end of the launch rod) is adjustable in angle of pitch. The pre-launch spin rate is indicated by a magnetic pick-up incorporated in the motor. The air to the motor is automatically disconnected when the launch gun first begins to drive the rod forward. A setup of this system is shown in Figure 36. The air jet tube is used to give the model desired amounts of yaw rates. This additional capability makes it possible to vary the pitch-yaw motion history of a spinning model through a wide spectrum. Similar techniques for launching spinning models are used by the Naval Ordnance Laboratory[49] and the Ballistic Research Laboratories[50].

3.4 Vertical Drop

Under some conditions, dropping the model from the top of the test section is a very useful technique. This approach has been successfully applied to spherical[15] and conical models[51] in the AEDC wind tunnel facilities. In order for the vertical-drop to be useful, the acceleration due to the drag force cannot be substantially greater than the gravity acceleration.

If the physical arrangement of a wind tunnel is such that a model can be dropped into the flow from above the test section and the model can be conveniently caught below the test section, the vertical-drop is very valuable for a model having drag acceleration small compared to that of gravity. An intricate model, such as one containing considerable amounts of internal mechanism (properly packaged telemetry equipment, etc.) can be flown many times without serious damage to the instrumentation*.

3.5 Vertical Tunnel

When it is practical to closely match the model drag force with the model weight, a vertical tunnel is very useful in the study of model dynamic stability. This technique has been successfully used in the arc-heated wind tunnel at the NASA Ames Research Center for the study of ablation effects on very short, high-drag model configurations[53]. The model is held against a hollow sting with a monofilament line. Once the tunnel has reached the desired operating conditions, the protective shield is removed laterally from ahead of the model. Then, when steady-state ablation is achieved, the monofilament line is electrically burned at the model base and the sting is quickly retracted, leaving the model in free-flight. Orthogonal-plane cameras are used to record the motion of the flights, which can be several seconds long.

4. MODELS

4.1 General

Due to the low accelerations (usually less than 100 g) that models are subjected to in a conventional wind tu. ' free-flight test, there is a large variety of applicable model design and construction techniques. This low acceleration is in direct contrast to the high acceleration for a ballistic range test (approximately 10^5 g). Before discussing the major model designs which are currently in use, it would be appropriate to go into the effects of the various model mass characteristics (mass, center of gravity, and moment of inertia) which affect the model motion during its free-flight trajectory. The significance of model design parameters upon the trajectory will then become apparent.

4.2 Simplified Equations of Motion

In order to guide the preparation of a test program, simplified planar-motion equations are adequate. They are based upon linearized theory and small amplitude of oscillation with the dynamic pressure on the model remaining constant during the entire trajectory (the model velocity is negligible compared to the freestream flow velocity). The following equations describe the trajectory as a function of the model mass and flow characteristics:

Model acceleration:

$$a = \frac{qAC_{D_{eff}}}{W} g \qquad (2)$$

---

* Heavily-instrumented models can be caught with no internal damage and minor external even when flown under conditions of high axial acceleration. Such a special model catcher has been developed for use in the General Dynamics San Diego wind tunnels[52]

Model velocity after traveling distance S :

$$V_m = \left(\frac{2SqAC_{Deff}}{m}\right)^{\frac{1}{2}} \tag{3}$$

Time to travel distance S :

$$t = \left(\frac{2Sm}{qAC_{Deff}}\right)^{\frac{1}{2}} \tag{4}$$

Cycles of oscillation while traveling distance S :

$$N = \frac{1}{\pi}\left(-\frac{C_{m\alpha}}{C_{Deff}} S \frac{d}{2} \frac{m}{I}\right)^{\frac{1}{2}} \tag{5}$$

Frequency of oscillation (c/s):

$$f = \frac{1}{2\pi}\left(-\frac{AdqC_{m\alpha}}{I}\right)^{\frac{1}{2}} \tag{6}$$

Peak-to-peak model vertical motion:

$$\Delta y = \frac{2\alpha_0 I}{md}\left(\frac{C_{L\alpha}}{C_{m\alpha}}\right) \tag{7}$$

Angle-of-attack oscillation envelope at end of distance S :

$$\left(\frac{\alpha_t}{\alpha_0}\right)_{env} = e^{\frac{t}{2}\left(\frac{M_D}{I} + \frac{M_S}{m}\right)} . \tag{8}$$

4.3 Materials

A great number of solid materials can be used to build free-flight models. The material density can range from light-weight plastics to platinum. A list of practical and familiar materials is included in Table IV. The specific heats and the thermal conductivities of the metals are included as well as the densities of all materials. The thermal properties aid in the choice of a material for models which are to have wall temperatures differing from adiabatic. The three light metals (magnesium, beryllium, aluminum) are good choices for light-weight model shells whether the models are adiabatic, cooled, or heated.

Materials that are usually used for the model core are lead, copper (adiabatic models at high temperature), and gold (the optimum choice for the maximum ratio of mass to moment of inertia). The choice of material for the core, as well as for the model-shell, is generally limited to plastics or malleable metals which minimize damage to the wind tunnel structure. The use of hard materials such as chromium, steel tungsten, platinum, or hevimet should be avoided even though they do have certain advantages. Since a model can contain several different metals, the thermal expansion coefficient is listed in Table IV in order to point out possible problems when the model wall temperature during the test is different from room temperature.

4.4 Equations for Body Mass Characteristics

Equations useful in computing model mass, center of gravity, and moment of inertia are presented. In model design it is necessary to have a suitable total weight, proper center-of-gravity location, and an upper or lower limit for the moment of inertia. Additional information may be found in Reference 55.

4.4.1 Mass: $m = \rho \int dx\,dy\,dz$

4.4.1.1 Circular cylinder

Solid: $m = \rho\pi r^2 h$

Thin wall: $m = \rho\pi d t h$ (open ends).

4.4.1.2 Circular cone

Solid: $m = \frac{1}{3}\rho\pi r^2 h$

Thin wall: $m = \rho\pi r t (r^2 + h^2)^{\frac{1}{2}}$ (open base).

4.4.1.3 Sphere

Solid: $m = \frac{4}{3}\rho\pi r^3$

Thin wall: $m = 4\rho\pi r^2 t$.

4.4.1.4 Ellipsoid

Solid: $m = \frac{4}{3}\rho\pi abc$

Thin wall: $m = \frac{4}{3}\rho\pi t(ab + ac + bc)$.

4.4.2 Center of Gravity: $X_{cg} = \frac{1}{V}\int x\,dV$

4.4.2.1 Circular cone

Solid: $X_{cg} = \frac{1}{4}h$ from base

Thin wall: $X_{cg} = \frac{1}{3}h$ from base (open base).

4.4.2.2 Truncated Circular Cone

Solid: $X_{cg} = \frac{h}{4}\frac{(R^2 + 2rR + 3r^2)}{(R^2 + rR + r^2)}$ from base

Thin wall: $X_{cg} = \frac{h}{3}\frac{R + 2r}{R + r}$ (open ends).

4.4.2.3 Hemisphere

Solid: $X_{cg} = \frac{3}{8} r$ from base

Thin wall: $X_{cg} = \frac{1}{2} r$ (open base).

4.4.2.4 Segment of a sphere

Solid: $X_{cg} = \frac{3}{4} \frac{(2r - h)^2}{(3r - h)}$ (from sphere center)

Thin wall: $X_{cg} = \frac{1}{2} h$ (flat, open base body).

4.4.2.5 Hemi-ellipsoid

Solid: $X_{cg} = \frac{3}{8}$ length of semi-axis normal to base from base

Thin wall: $X_{cg} = \frac{1}{2}$ length of semi-axis normal to base from base (open base).

4.4.3 Moment of Inertia: $I = \int x^2 \rho \, dm$

4.4.3.1 Circular cylinder (about an axis through c.g. perpendicular to axis of symmetry)

Solid: $I = \frac{m}{12} (3r^2 + h^2)$

Thin wall: $I = \frac{m}{2} (r^2 + \frac{1}{6} h^2)$ (open ends).

4.4.3.2 Right circular cone (about an axis through its c.g. and perpendicular to axis of symmetry)

Solid: $I = \frac{3}{80} m (4r^2 + h^2)$

Thin wall: $I = m \left(\frac{r^2}{4} + \frac{h^2}{18} \right)$ (open base).

4.4.3.3 Sphere (about a diameter)

Solid: $I = \frac{2}{5} mr^2$

Thin wall: $I = \frac{2}{3} mr^2$.

4.4.3.4 Ellipsoid (about semi-axis c)

Solid: $I = \frac{m}{5} (a^2 + b^2)$

Thin wall: $I = \frac{m}{5} \left(\frac{a^3 b + a^3 c + b^3 a + b^3 c + 3a^2 bc + 3ab^2 c}{ab + ac + bc} \right)$.

4.4.3.5 Hemisphere (about an axis through c.g. perpendicular to axis of symmetry)

Solid: $I = \frac{83}{320} mr^2$

Thin wall: $I = \frac{5}{12} mr^2$ (open base).

Symbol Definiton for Model Mass Characteristics

a, b, c	semi-axes of ellipsoid
d	diameter
h	height
m	mass
r	radius
R	base radius of truncated cone
t	wall thickness
V	volume of material

4.5 Design and Construction

Numerous methods of model design and construction have already been successfully employed. As the maximum acceleration experienced by the models prior to and during the data acquisition period are usually below 10^2 g, the models can be of very delicate, yet simple, construction. For example, the center of gravity can be located near the forward end of the model. In addition, airplane models having delicate surfaces can be easily built and successfully tested. Construction of the Apollo abort configuration (re-entry vehicle with tower and escape rocket) is not difficult, even though the tower design consists of a fine skeletal framework. These examples serve to illustrate the wide variety of materials and model configurations which can be used because of the low loads that models experience during free-flight testing (launch and trajectory) in a wind tunnel.

The acceleration of the models should not be so low as to have the flight path drop out of view before sufficient information is acquired. On the other hand, too high an acceleration will decrease the number of high-speed movie frames of the flight below the desired number (say 200 frames at 4000 frames/sec). If a steady light source is used for the movies, the model image may be elongated due to excessive model movement during one frame (60-80 μsec exposure). Model acceleration and the resulting flight time and velocity (relative to ground) at the termination of a wire-release trajectory are shown in Figures 37, 38, and 39. These values also apply to each half of a gun-launch trajectory.

The model design can be somewhat complicated when dynamic stability and/or pitch-moment data are desired. This becomes evident from the approximate equations of motion. The amplitude decay and the number of oscillation cycles during the model's travel across the viewing area are all a function of the model size and the ratio of the model mass to the moment of inertia about its center of gravity. For similarly constructed models, a decrease in model size results in an increase in both the amplitude decay (or growth) and the number of cycles of oscillation during a certain distance (relative to ground) that the model travels.

In order to obtain the required ratio of mass to moment of inertia, the model shape can be a thin shell or else a very light-weight solid material (such as 2 lb/ft^3 polyurethane foam) with a spherical core of lead or, preferably gold. The size of the core can be chosen to optimize the ratio m/I . For purposes of illustration, Figure 40 shows the variation of the value $r_s(m/I)$ with r_c/r_s for various diameters of spherical models (½ in. to 3 in. diameter) made of a heavy core, such as lead or gold, at the center of a light-weight substance. Polyurethane foam can be used such that the density of the core is 100 or 200 times the density of the homogenous outer shell. Usually it is desirable to choose a somewhat larger ratio of r_c/r_s than optimum for maximum $r_s m/I$ in order to increase the model weight and thus increase the total flight time.

The most simple model can be formed out of a single piece of material, usually aluminum or magnesium. The base of the model can be hollowed out in order to place the center of gravity at the desired location. An example of this type of construction is in Figure 41(a). In order to increase the number of cycles of oscillatory motion while the model is in the viewing area, it is necessary to increase the ratio of the model mass to the moment of inertia (m/I). This is done by adding a core of some relatively soft but dense material such as copper, lead or gold. Figure 41(b) shows an aluminum model with a copper cylindrical slug for ballast. Usually the shell can be made as thin as 1% of the local diameter. Using the process of electrolysis, 1 in. diameter models have been made with copper shell of 0.003 in. thick wall.

Models are often constructed of some plastic material and then ballasted with a lead or gold core. Originally, models were cast from polyurethane foam (Fig. 41(c)), but, due to the lack of ability to duplicate the foam density and uniformity from model to model, injection-molded polystyrene model construction was developed. Not only were the injection-molded models considerably more uniform, they were stronger and took far less time to construct. By experiment, it was found that models could be molded with walls as thin as 0.015 in. which, when compared with a polyurethane-foam model of the same shape, had less than one half the mass (before ballast was added). Injection-molding presses are shown in Figure 42. The smaller one shown is hand operated and is used principally for sample runs or small models. It will inject up to ¾ oz of polystyrene per cycle. Only up to 20 models per hour can be made with this small press. It is limited to models which have a diameter below 1½ in. The larger press is semi-automatic and, with this one, it is possible to make in excess of one-hundred models per hour. The ability to inject 3 oz of polystyrene makes it possible to mold larger models. Figure 43 shows the various molding dies required for one type of model and Figure 41(d) shows a typical completed model with a section removed.

4.6 Measurement of Mass Characteristics

An item of major importance to the quality of the final data is the measurement of the mass characteristics of the models. The care required for satisfactory measurements is more severe than for ballistic range models because the wind tunnel models are, as a rule, very light-weight.

4.6.1 *Mass*

Fortunately, the availability of precision analytical balances makes very accurate determination of the model mass convenient. However, extreme caution should be exercised in applying the measured model reference lengths to the data reduction process. Since the linear dimensions are obtained at room temperature, coefficient-of-expansion corrections must be included in order to compensate for the different-from-room model temperature which may exist during the flight trajectory. This temperature consideration must also be applied to the moment of inertia measurement, and, if not in dimensionless form, to the model center-of-gravity location.

4.6.2 *Center of Gravity*

The instrument for locating the model center of gravity consists of two analytical balances[45] each capable of measuring to 0.1 mgm. One balance is used to measure the mass. The left-hand beam of the other balance has been altered to provide a reference pad and platform to support the model (Fig.44). The accuracy to which the balance point could be determined was markedly improved by the addition of a microscope for viewing the pointer. Precision ball bearings ranging in diameter from 0.250 in. (1.047 gm) to 1.000 in. (65.690 gm) were used to calibrate the system. A series of bars, rods, tubes, and flat plates were then used to demonstrate the degree of accuracy when the center-of-gravity measurement system was applied to a typical model. This result is shown in Figure 45. The inaccuracies of this system are within 1% for calibrating bodies as light as 0.3 gm. As the weight increases the accuracy increases, and for model weights of 10 gm, the error is insignificant.

4.6.3 *Moment of Inertia*

The instrument complex[45] for measuring the moment of inertia is composed of a wire and its overhead support, model support, light source, photo cell, electronic frequency divider, and a counter (Fig.46). The sensitivity of this system for measuring the oscillation period of a model is ±0.2 msec. Viscous effects on the system do not appear to be significant. There is generally no need for performing this measurement in a vacuum. An atmospheric-pressure, still-air environment is usually adequate.

Calibration of this system is accomplished by inserting precision shapes, such as discs, rods, tubes, and flat plates, for which the moments of inertia have been calculated (based upon their dimension and mass). In order to increase the overall accuracy of the system the model holder should be of minimum moment of inertia. This is especially true for the very small and light models. The reference period of the system and model holder, with no model in place, is determined at frequency intervals. This provides a comparison when the same procedure is followed during the measurement of the actual models. The calibrating bodies are designed to bracket the expected moments of inertia of the free-flight models and should be of the same weight and the same general shape or length. Such an approach minimizes both the effect of wire tension on the wire torsional constant and the effect of viscosity. Although both of these effects are usually small (less than 1%), it is always desirable to eliminate any possible source of error.

The results of an extensive calibration study are presented in Figure 47. Here the effect of the calibrating body weight on the wire torsional constant can be seen.

Regardless of the shape of the calibrating body, the data fall within a 1% band throughout the entire range of weights. Using data in the form in Figure 47, the equation used to obtain the moment of inertia of a model is

$$I = K_{(m+h)} t^2_{(m+h)} - I_h \quad , \tag{9}$$

where I = model moment of inertia

I_h = model holder moment of inertia

$K_{(m+h)}$ = wire torsional constant for model in holder

$t_{(m+h)}$ = oscillation period for model in holder.

An acceptable, but somewhat less accurate, alternative approach is simply to plot the square of the oscillation period against the calculated moments of inertia for the calibrating bodies, arbitrarily setting the empty holder condition to zero moment of inertia. If the calibration points plot up as a straight line (see Figure 47), then the equation

$$I = I_c \left[\frac{t^2_{(m+h)} - t^2_h}{t^2_{(c+h)} - t^2_h} \right] \quad , \tag{10}$$

where I_c = calibrating body moment of inertia

$t_{(c+h)}$ = oscillation period for calibrating body in holder

t_h = oscillation period for empty holder,

can be used to calculate the model moment of inertia. If the curve is not linear, then the values of the model moment of inertia can be interpolated from the faired data points.

5. DATA ACQUISITION

5.1 General

The types of data which can be obtained from free-flight testing fall into three general categories: model motion studies, flow field studies, and telemetry information. The basic aerodynamic coefficients (drag, static and dynamic stability, and lift) are deduced from motion studies in much the same manner as is done in normal ballistic range testing. The flow field studies can be of two distinct types, visual and probe surveys. Telemetry is used to determine model base pressure and heating, and can also be employed to deduce model motion characteristics from accelerometer data. To date, visual model motion studies form the bulk of information gathered from free-flight testing. Nevertheless, the other types of information are extremely important and do depend, in mar cases, upon interference-free testing techniques.

5.2 Model Motion Studies

The model motion is normally recorded on movie film at 2000 to 5000 frames per second. The larger 35 mm film generally is preferred to 16 mm film. If only several views of the model (up to ten) are required during its trajectory, discreet views as a function of time may be superimposed upon a single large film sheet (11 in. × 14 in.)

by the use of a multiple strobe light. This procedure has two distinct advantages: (i) all of the motion is recorded on a single sheet of film, and (ii) the model image appears full-scale rather than at a greatly reduced scale for the usual parallel light movie film system.

Two electronic-type means are also used in order to record the model motion. An electronic-visual system, such as a cathode-ray tube follower unit, can be used to measure axial displacement from which the acceleration, and consequently the pertinent coefficients, can be determined. In order to have the model independent of any visual access, the model can be instrumented with accelerometers which use telemetry techniques to transmit the information[56].

5.2.1 Non-Planar Motion

When the model motion is not planar, such as would be expected for spinning models, it is necessary to record its motion in two planes in order to obtain the aerodynamic characteristics from film data.

To install an orthogonal optical system in an open jet wind tunnel, generally minor modifications are required[46]. But for a two-dimensional tunnel having a flush-walled test section, modifications become more difficult.

Rather than perform major alterations on the upper and lower walls in the test section of the JPL Supersonic Wind Tunnel, in order to make a two-plane parallax-free optical system, the conventional horizontal optical beam was split in two parts and re-directed through the vertical windows. Figure 49 shows the mirror system which generates an "X" optical path inside the test section. Due to hardware limitations, it was not possible to have these two planes at right angles to each other. However, the included angle of 60 deg does not significantly degrade the determination of the model angular orientation relative to that with an orthogonal system. Simple trigonometric functions convert the data to the normal orthogonal system. Then conventional ballistic range techniques (linearized aerodynamics) can be used to reduce the data[4].

5.3 High Speed Movies (HSM)

5.3.1 Film Size and Frame Rate

Since the image size is 2¼ times larger, the use of 35 mm film* is preferred to 16 mm. The 5000 frame/sec speed of the 35 mm half-frame is more than adequate for free-flight motion studies. There does not seem to be any requirement for the 8000 frame/sec rate achievable with the 16 mm film. One advantage of a high frame speed is to minimize the model motion during the exposure time of each frame if a steady light source is being used. At 5000 frames/sec the film frame exposure time is about 67 μsec. With a model velocity relative to ground of 100 ft/sec, this would result in model movement of 0.08 in. during an exposure. This is a large amount since model-position reading accuracy on the film is about 0.01 in. This model motion during exposure can be decreased well below the film reading error by using a multi-flash strobe light having 1-2 μsec exposure. The reluctance pickup on the movie camera sprocket is used to synchronize the strobe with the camera shutter.

---

* For many types of tests 70 mm, even at its lower frame rate, may be the optimum choice

5.3.2 Lighting

The model can be front-lighted if multiple exposures are desired upon a single sheet of film. Due to the usual model curvature, this type of illumination does not give optimum contrast between the model edges and the dark background. If multiple exposures on a single picture are not desired, then the model should be back-lighted in preference to front-lighting. Back-lighting, either silhouette or schlieren, outlines the model adequately. The silhouette lighting gives the highest and most consistent definition between the model edges and the background. However, the schlieren lighting for defining the flow field about the model is usually a desirable capability and is required for certain tests. The multiple strobe equipment which is capable of 500-1000 consecutive flashes at a rate of 5000 per second can be used either to silhouette the model or to create the schlieren lighting. The silhouette effect can be achieved by either of two approaches. The first employs light from schlieren system light-house with the knife-edge cut-off removed. The second takes advantage of a ground glass which is illuminated by a light source, and can be located outside the viewing area away from the camera.

When it is required to observe reference marks on the model, white marks are put on a black model. The front lighting will make it possible to observe these reference marks without decreasing the contrast between the model edge and the back lighting. This technique is required for spinning models.

5.3.3 Trajectory Reference Marks

For convenience in film reading, a precision grid of fine, taut wires (0.010-0.020 in. diameter) can be incorporated in one of the viewing areas. This grid serves both to locate the model in space and to determine the model attitude. By having a grid cover the entire viewing area, distortions which can occur in the optical system and photographic processing are not serious since the model measurements can always be related to known reference lines in the immediate vicinity of the model image. An example of the actual size of a recorded image and a subsequent enlargement are in Figure 2.

5.3.4 Film Emulsion Type

Surprisingly enough, a high-speed film emulsion is not required for this application. The lighting, either steady or strobe, is of high enough intensity such that the choice of a medium speed (ASA $\approx$ 100) is the best choice. This is a compromise between the contrast of a high speed film and the fine grain of a low speed film. Perhaps the lighting may vary enough from various wind tunnel facilities that the optimum film choice will have to be evaluated. Serious consideration should always be given to the lower speed films.

5.3.5 Camera and Location

Any of the several high speed (greater than 1000 frames per second) motion picture cameras can be used for recording the model motion during its trajectory across the viewing areas. In testing, the camera must be started up at the proper time relative to the trajectory. Allowance should be made to have the film transport process come up to full steady speed at the time the model trajectory is first recorded. It is important to have provisions for putting accurate timing marks on the film. In addition, it is desirable to have the camera shutter synchronized with the strobe light.

The camera is normally located outside of the wind tunnel flow channel. Should the size of a tunnel permit, it may be useful to install a camera within the tunnel at the downstream end of the model trajectory in order to view the model motion along its axis of motion. The camera outside the tunnel can be incorporated in the schlieren system. Using the schlieren system in conjunction with the movies, parallax can be eliminated. Otherwise, a correction must be made for parallax. This is a simple matter if the camera distance from the model is large compared to the length of the viewing area and the camera axis is normal to the model trajectory.

5.4 Wake Studies

5.4.1 Optical

As schlieren and shadowgraph techniques are quite widely used, there is no need to go into the specific details here. The other additional requirement is for timing the optical spark source to obtain a picture of the flow field when the model is in a desired location or attitude. The use of a high speed movie camera greatly simplifies this timing problem, but only at the cost of degradation in the quality of the data. The use of a single large sheet of film will give excellent optical definition. The timing of the spark source for trim-angle trajectories can be done by employing a timing delay at launch or by a photocell system which lies in a plane normal to the data plane and intersects the model trajectory.

5.4.2 Survey Probe

There are several major criteria which must be established in order to obtain valid data. The instrument (pressure, temperature, etc.) must have response times of no more than several milliseconds. The data accuracy required and the extent of the data desired during the model trajectory determine the maximum instrument response time. The instrument must be designed such that the portions immersed in the model wake do not disrupt the interference-free flow conditions upstream of the probe leading edge (see Figure 29). This minimum interference requirement is not compatible with minimum response time. Therefore, compromises must be made. In the case of a pressure probe, the transducer container should be located just above the initial wake position and a pressure probe is "offset" to the desired location in the wake. Care must be exercised in the calibration of the instrument. Usually the sensitivity is stable, so the level is the only item requiring on-the-spot calibration. This can generally be done by traversing the instrument into the undisturbed free-stream or by having a dual-probe system, one being used for establishing a reference pressure but having a very long response time. The remaining required information is knowledge of the model position relative to the instrument as a function of the instrument reading. High speed movies, taken in the normal manner, along with correlating timing identifications take care of this requirement.

5.5 Base Studies

Since a sting, or any other physical support such as wires and side mounts, is likely to alter the flow in the base region, it is necessary to use an interference-free technique, such as free-flight, in order to measure valid model base conditions (pressure and heat transfer). This can be done very conveniently by the use of telemetry techniques. Since the model maximum acceleration rarely exceeds 100 g, it is relatively simple to design, build, and operate telemetry systems including the measuring transducers, compared to the problems which would be involved in taking similar measurements in a ballistic range model, where the accelerations can exceed 10^5 g. A typical setup for a gun-launch free-flight base pressure telemetry test is shown in Figure 51.

A typical telemetry package (0.80 in. long by 0.80 in. diameter, weighing about 10 gm) with its pressure transducer is shown in Figure 52. Its circuit diagram and details of its design[58] appear in Figure 53. The electronic circuit used is a colpitts oscillator, consisting of a printed circuit inductor, a pressure sensitive capacitor, two small mercury cells, and other circuit components of the micro-miniature pellet type construction. The inductor also serves as the transmitter antenna. A frequency range of 98-118 Mc is used. Further details on this system can be found in Reference 58. This telemetry technique is also operational at AEDC[51] and the NASA Ames Research Center[59].

A sample oscilloscope trace from a gun-launch free-flight base pressure trajectory is shown in Figure 54. In addition, a reference run is presented in which the pressure sensor is sealed off. In order to increase the accuracy of the interference-free base pressure measurement, the initial reference pressure can be lowered to the expected value of the desired base pressure measurement. The use of the wire-release technique can also be used to obtain interference-free base pressure values. However, this method does not permit any convenient control over the magnitude of the reference pressure. The reference pressure can be measured by a minimal interference pitot tube which can be rapidly removed from the flow just prior to model release. An example of data using this approach is in Figure 29. By replacing the pressure transducer with a heat meter, the same telemetry package can be used to measure base heating.

It may be necessary to use telemetry along with probes mounted on the model base in order to make measurements in the wake region between the model base and the wake neck. This is due to the possibility that any protrusion into this region from downstream will disturb the flow. Although the use of telemetry eliminates the interference problems caused by an externally mounted probe, it may not be adequate because of the possible interference from the probe which extends aft from the base. In any case, the base pressure can be measured and observed in order to indicate the presence of flow disturbance caused by any probe within the wake. Optical studies should not solely be used to give a qualitative indication as to whether or not a probe within the wake regic disturbs the flow being studied.

6. TRAJECTORY MOTION DATA REDUCTION

6.1 Introduction

For convenience, only the planar* trajectory runs are generally reduced. Linear pitching moment is usually assumed in order to reduce the data. The resulting dynamic

---

* By obtaining motion studies in orthogonal (or near-orthogonal) planes, non-planar trajectory runs caused by spinning models or by non-ideal launches can be handled by the use of normal ballistic range data reduction programs

damping stability is assumed to be an effective constant over a particular oscillation cycle during a limited oscillation range. However, as the oscillation amplitude approaches 90 deg (and can even go nearly to 180 deg), the assumption of a linear pitching moment curve is no longer valid. For such cases, a more complex theoretical approach is required as a basis to obtain dynamic stability data of acceptable accuracy. However, the actual data reduction process is not materially complicated for the non-linear pitching moment case.

In this report both the linear and non-linear pitching moment, planar trajectory data reduction approaches and procedures will be discussed. No discussion will be included on the non-planar, spinning model.

6.2 Film Reading

Orthogonal-view high-speed movie records are made of each run. The upper camera, which views the motion in the horizontal plane, is normally used only to confirm that the trajectory motion is planar and lies entirely in the vertical plane. Its field of view covers just a portion of the useful trajectory and non-parallax problems are severe. The film from the side camera, which records the model motion in the vertical plane, is used for the detailed data reduction. However, if the trajectory does not achieve the desired degree of planar motion, use can be made of the film from the upper camera in order to augment the side view for data reduction. Of course, if the model has spin, then data reduction must be accomplished by using both planes of view.

When the runs are few, it is convenient to make photographic prints for a selected number of frames from the high speed movie film. These enlargements, which can be about half of actual model size, can be read by use of a scale and protractor. But first it is necessary to construct a template the same size as the enlarged model image. This template serves to integrate the edges of the image in order to obtain the best consistency and accuracy in reading the model angle of attack and center-of-gravity location. For large quantities of data, the enlarged photograph approach is not convenient, and use of a semi-automatic film-image projection-type data reading equipment is desirable. Here again the procedure requires the use of a template to optimize the quality of the data.

Regardless of the approach used to read the film, it is usually not necessary to read every frame of data. The type of model trajectory guides the choice as to how many frames of obtained data need be read. For zero oscillation drag runs, perhaps only every tenth frame need be read. For the usual damped motion oscillating trajectories, every second or third frame is sufficient. For obtaining the best accuracy of the oscillation envelope, it is best to read the model angle for every frame of data in the region of the peak amplitude. A typical plot of oscillation amplitude for a model with highly damped motion is shown in Figure 55. A sample raw data tabulation is in Table V.

Once the raw data (model c.g. longitudinal and lateral locations, along with model angular attitude) are obtained as a function of the film frame number, it is necessary to convert it to a function of time. This is accomplished by relating the film frames to time by use of the timing marks which are put on the film edge every millisecond. If two separate rolls of film are obtained for a particular trajectory in order to record the motion in two planes, it is necessary to put additional marks on the film in order to match the films together at just a few points during a trajectory. This serves as a direct check on any other attempt to link the two films together.

The raw data, whether it be frame, model position, or attitude versus time is then smoothed by any convenient data smoothing process. This procedure pinpoints any major film reading error and also results in data of nominally higher accuracy than can be obtained from the original raw data. The smoothed model c.g. axial position data can then be curve-fitted. This facilitates the calculation of the model horizontal velocity as a function of time or the relative distance the model travels in the airstream.

6.3 Drag Reduction

The coordinate system used for the reduction of data is one which references the model position to the moving gas media; X is the longitudinal distance between the model and the media and is the independent variable for the angular and translational equations of motion[29,60-62]. The instantaneous drag coefficient may be obtained directly from the translational equation of motion

$$m\ddot{X} = -\tfrac{1}{2}\rho V^2 A C_D \qquad (11)$$

by changing the independent variable from time to distance. This results in

$$C_D = -\frac{2m}{\rho A}\,\frac{d[\log_e(1 + V_m/V_\infty)]}{dX} \ . \qquad (12)$$

A linear fit through a section of the $\log_e(1 + V_m/V_\infty)$ versus X data yields an effective constant drag coefficient for that section. When there are sufficient data at a range of amplitudes, due to the decay, several effective drag points as a function of various amplitudes of oscillation per flight may be obtained.

6.4 Static and Dynamic Stability Data Reduction*

For an axisymmetric body with first-order linear aerodynamic coefficients ($C_m = C_{m\alpha}\alpha$; $C_L = C_{L\alpha}\alpha$; $C_D = C_{D0}$) and small angular excursions, the equation of planar angular motion may be written as a second-order differential equation with constant coefficients:

$$I\ddot{\theta} = \tfrac{1}{2}\rho V^2 A d C_m + \tfrac{1}{2}\rho V^2 A d(C_{mq} + C_{m\dot{\alpha}})\left(\frac{\dot{\theta}d}{V}\right) \ . \qquad (13)$$

The translational equation in the X direction (longitudinal) is Equation (11), and in the Z direction (vertical) is

$$m\ddot{Z} = \tfrac{1}{2}\rho V^2 C_L + mg \ . \qquad (14)$$

The solution to Equation (13) is

$$\alpha = \alpha_0 e^{\lambda X}\cos\left[\left(-\frac{\rho A d}{2I}\,C_{m\alpha} + \lambda^2\right)^{\frac{1}{2}} X\right] \ , \qquad (15)$$

* This data reduction analysis is a condensation of that appearing in Reference 60

where

$$\lambda = \frac{\rho A}{4m}\left[C_{D0} - C_{L\alpha} + \frac{md^2}{I}(C_{mq} + C_{m\dot{\alpha}})\right] \quad . \tag{16}$$

In general

$$-\frac{\rho Ad}{2I} C_{m\alpha} \gg \lambda^2 \tag{17}$$

and therefore

$$C_{m\alpha} = -\frac{2I}{\rho Ad}\Omega^2 \quad , \tag{18}$$

where Ω is the distance frequency of oscillation (2π cycles per unit distance of X). The dynamic stability coefficient may be obtained from the amplitude envelope:

$$(C_{mq} + C_{m\dot{\alpha}})\frac{md^2}{I} = \frac{4m}{\rho A}\left(\frac{1}{X - X_0}\right)\log_e\left(\frac{\alpha_X}{\alpha_0}\right) + C_{L\alpha} - C_{D0} \quad , \tag{19}$$

where α_X is the particular amplitude corresponding to the distance X , and α_0 is the amplitude at $X = X_0$.

However, the conditions imposed upon this solution for the damping coefficient are, in general, too restrictive, and more applicable solutions are used. An unrestricted integral equation for determining the dynamic stability (pitch damping) coefficient from energy considerations has been developed[61,62]:

$$C_{mq} + C_{m\dot{\alpha}} = \frac{-\frac{md}{I}\int_{-(\theta_0-\delta\theta)}^{\theta_0} C_m(\alpha)\, d\theta - \int_{-(\theta_0-\delta\theta)}^{\theta_0} C_D(\alpha)\theta'\, d\theta}{\frac{md^2}{I}\int_{-(\theta_0-\delta\theta)}^{\theta_0} \theta'\, d\theta} \quad , \tag{20}$$

where θ_0 is the initial amplitude, $-(\theta_0-\delta\theta)$ is the amplitude after one half cycle, C_m and C_D are functions of α , and $(C_{mq} + C_{m\dot{\alpha}})$ is the effective constant damping coefficient. Using small angle assumption and assuming negligible effect of gravity in Equation (14), the terms α and θ are related by

$$\alpha = \theta + (\alpha - \theta) = \theta - \frac{\rho A}{2m}\int_{\theta_0}^{\theta} \frac{C_L(\alpha)}{\theta'}\, d\theta \quad . \tag{21}$$

Expanding $C_m(\alpha)$ in a Taylor series about θ , and considering only the first-order derivatives,

$$C_m(\alpha) = C_m(\theta) - \frac{\rho A}{2m} \frac{dC_m(\theta)}{d\theta} \int_{\theta_0}^{\theta} \frac{C_L(\alpha)}{\theta'} \, d\theta \quad . \tag{22}$$

The lift and drag coefficients will be assumed to be functions of θ directly instead of α. This is equivalent to saying the second terms in their Taylor series expansions are quite small. Since, in general, lift and drag have second-order effects on the amplitude decay, a small error in their contribution will lead to only negligible errors in the final solution for the dynamic stability coefficient. Furthermore, since the decay is very small, $\delta\theta << \theta_0$, in all terms except that containing the prime moment function, $C_m(\theta)$, the lower limit of integration, $-(\theta_0-\delta\theta)$, will be replaced by θ_0. Again, the error introduced by this approximation will be a small part of a second-order effect. Introducing these into Equation (20) results in a working form of the energy integral equation:

$$(C_{mq} + C_{m\dot{\alpha}}) \frac{md^2}{I} = \frac{-\frac{md}{I} \int_{-(\theta_0-\delta\theta)}^{\theta_0} C_m(\theta) \, d\theta + \frac{\rho Ad}{2I} \int_{-\theta_0}^{\theta_0} \frac{dC_m(\theta)}{d\theta} \int_{\theta_0}^{\theta} \frac{C_L(\theta)}{\theta'} \, d\theta - \int_{-\theta_0}^{\theta_0} C_D(\theta)\theta' \, d\theta}{\int_{-\theta_0}^{\theta_0} \theta' \, d\theta} \tag{23}$$

In solving particular problems with this energy integral equation, it will be assumed that the model angular velocity, θ', is a function primarily of the pitching moment, and other contributions can be neglected. In the linear case this is equivalent to the condition of Equation (17). In most physically probable situations this assumption proves excellent. In general, then, the following approximation for θ' obtained from the basic equation of motion by neglecting all terms except the pitching moment, is quite good:

$$\theta' = \pm \left[\frac{\rho Ad}{I} \int_{\theta_0}^{\theta} C_m(\theta) \, d\theta \right]^{\frac{1}{2}} \quad , \tag{24}$$

where the sign of θ' is dependent on the sign of θ_0.

Using this expression for the angular velocity, a solution for the dynamic stability coefficient of an axisymmetric body with general lift and drag curves at any oscillation amplitude can be developed for linear and non-linear pitching moments.

6.4.1 Linear Pitching Moment: $C_m(\alpha) = C_{m\alpha}\alpha$

Integration of Equation (24) gives

$$\theta' = \pm\left[\frac{\rho Ad}{I}\int_{\theta_0}^{\theta} C_{m\alpha}\theta\, d\theta\right]^{\frac{1}{2}} = \pm\left[\left(-\frac{\rho Ad}{2I}C_{m\alpha}\right)^{\frac{1}{2}}(\theta_0^2 - \theta^2)^{\frac{1}{2}}\right] . \qquad (25)$$

Arbitrary lift and drag curves may be approximated to any desired accuracy by power series in θ. For an axisymmetric body the two series will be odd and even respectively.

$$C_L(\alpha) = C_L(\theta) = C_{L\alpha}\theta + \sum_{i=1}^{m} b_i\theta^{2i+1} \qquad (26)$$

$$C_D(\alpha) = C_D(\theta) = C_{D0} + \sum_{i=1}^{n} c_i\theta^{2i} . \qquad (27)$$

Inserting these in the energy equation and performing the indicated integrations yields the following solution for a half oscillation cycle:

$$(C_{mq} + C_{m\dot{\alpha}})\frac{md^2}{I} = -\frac{4m}{\rho A}\frac{\Omega}{\pi}\frac{\delta\theta}{\theta_0} + \left[C_{L\alpha} + 2\sum_{i=1}^{m}\left(\prod_{j=1}^{i+1}\frac{2j-1}{2j}\right)b_i\theta_0^{2i}\right] - \left[C_{D0} + 2\sum_{i-1}^{n}\frac{1}{2(i+1)}\left(\prod_{j=1}^{i}\frac{2j-1}{2j}\right)c_i\theta_0^{2i}\right] . \qquad (28)$$

Notice that this solution is equivalent to the solution of the linear differential equation (Eqn.(19)) when the c_i and k_i terms are set equal to zero. By extension then, this solution provides a correction to the linear solution which will account for non-linear lift and drag over an arbitrary number of cycles. However, the corrections are based on an amplitude value which changes during the flight due to the decay. It is, therefore, necessary to define a new amplitude value to be used for calculations and data correlation. The mean-square resultant angle of attack, δ^2, is defined as

$$\delta^2 = \frac{1}{X}\int_0^X \alpha^2\, dX . \qquad (29)$$

For a constant decay which is small in comparison with the oscillatory frequency, integration gives

$$\delta^2 = \frac{\alpha_X^2 - \alpha_0^2}{4\log_e(\alpha_X/\alpha_0)} . \qquad (30)$$

The mean amplitude for the flight will be defined in terms of δ^2 :

$$\bar{\alpha}_0^2 = 2\delta^2 = \frac{\alpha_X^2 - \alpha_0^2}{2\log_e(\alpha_X/\alpha_0)} . \tag{31}$$

In the limit, as the decay approaches zero, $\bar{\alpha}_0 = \alpha_0$. In the same manner that δ^2 best represents the mean square angle-of-attack, $\bar{\alpha}_0^2$ best represents the mean amplitude.

The usable solution for the dynamic stability coefficient for a body with a linear pitching moment is then

$$(C_{mq} + C_{m\dot{\alpha}})\frac{md^2}{I} = \frac{4m}{\rho A}\left(\frac{1}{X - X_0}\right)\log_e\left(\frac{\alpha_X}{\alpha_0}\right) + \left[C_{L\alpha} + 2\sum_{i=1}^{n}\left(\prod_{j=1}^{i+1}\frac{2j-1}{2j}\right)b_i\bar{\alpha}_0^{2i}\right] -$$

$$- \left[C_{D0} + 2\sum_{i=1}^{n}\frac{1}{2(i+1)}\left(\prod_{j=1}^{i}\frac{2j-1}{2j}\right)c_i\bar{\alpha}_0^{2i}\right] . \tag{32}$$

As an example, if the lift and drag are given by the expressions

$$C_L = C_{L\alpha}\alpha + b_1\alpha^3 + b_2\alpha^5 \quad \text{and} \quad C_D = C_{D0} + c_1\alpha^2 + c_2\alpha^4 , \tag{33}$$

the lift and drag terms in the solution are, respectively,

$$C_{L\alpha} + \tfrac{3}{4}b_1\bar{\alpha}_0^2 + \tfrac{5}{8}b_2\bar{\alpha}_0^4 \quad \text{and} \quad C_{D0} + \tfrac{1}{4}c_1\bar{\alpha}_0^2 + \tfrac{1}{8}c_2\bar{\alpha}_0^4 . \tag{34}$$

The final forms of the damping coefficient for the linear pitching moment case is then

$$(C_{mq} + C_{m\dot{\alpha}})\frac{md^2}{I} = \frac{4m}{\rho A}\left(\frac{1}{X - X_0}\right)\log_e\left(\frac{\alpha_X}{\alpha_0}\right) + (C_{L\alpha} + \tfrac{3}{4}b_1\bar{\alpha}_0^2 + \tfrac{5}{8}b_2\bar{\alpha}_0^4) -$$

$$- (C_{D0} + \tfrac{1}{4}c_1\bar{\alpha}_0^2 + \tfrac{1}{8}c_2\bar{\alpha}_0^4) . \tag{35}$$

The applicability of this solution for several specific lift and drag curves has been verified with an "exact" computer solution of the equations of motion. The analytical forms of the aerodynamic coefficients were entered into the program and the resulting motion computed. The value of $(C_{mq} + C_{m\dot{\alpha}})$ was then calculated with the above solution using the computer decay. The deviation between the result and the input value of $(C_{mq} + C_{m\dot{\alpha}})$ was less than 1% in all cases.

6.4.2 Non-Linear Pitching Moment

The oscillation frequency of a model is noticeably affected by the amount the pitching moment diverges from being linear. In addition, the effect of the dynamic stability upon the oscillation envelope may be dependent upon the amount that the pitching moment is non-linear. A closed-form analytic solution for these effects is not a straightforward matter, and does require both a simple form of a non-linear pitching moment and simplifying assumptions in solving the equations of motion. If the the pitching moment is either trigonometric or cubic in form, then a first integration yielding an expression for θ' may be performed as for the linear case. However, second integrations, such as those involved in Equation (23), generally lead to elliptic integrals of the first and second kinds.

An analysis of a cubic non-linear pitching moment of the form

$$C_m(\theta) = C_{m\alpha}\theta + 2r_m\theta^3 \quad , \tag{36}$$

where $r_m > 0$ (a destabilizing effect) will be described here*. Figure 56 shows the shapes of various cubic pitching moment curves as a function of $C_{m\alpha}/r_m$. Equation (13), neglecting all terms except the pitching moment, can be completely solved for both a linear and the cubic pitching moment. By equating distance frequencies over a quarter cycle, the effect of the non-linear moment on θ and θ' may be determined. Converting Equation (13) to distance,

$$I\theta'' = [\tfrac{1}{2}\rho Ad]C_m(\theta) + \theta' \frac{\rho A}{2m} \quad . \tag{37}$$

In the linear case where $C_m(\theta) = C_{m\alpha}\theta$, by neglecting the θ' term, double integration of Equation (37) yields the quarter-cycle distance

$$X_L = \tfrac{1}{2}\pi\left(-\frac{2I}{\rho AdC_{m\alpha}}\right)^{\frac{1}{2}} \quad . \tag{38}$$

In the non-linear cubic case, by neglecting the second-order θ' term, double integration of Equation (37) yields the quarter-cycle distance

$$X_N = \left(\frac{2I}{\rho Ad}\right)^{\frac{1}{2}}\left(-\frac{1}{C_{m\alpha} + r_m\theta_0^2}\right)^{\frac{1}{2}} F(k, \tfrac{1}{2}\pi) \quad , \tag{39}$$

where $F(k, \frac{1}{2}\pi)$ is the Legendre canonical form of the elliptic integral of the first kind and

$$k^2 = -\frac{\theta_0^2 r_m}{C_{m\alpha} + r_m\theta_0^2} \quad \text{(with } \theta_0 \text{ in radians).} \tag{40}$$

An expression for the effective linear pitching moment slope, $(C_{m\alpha})_{eff}$, which would give the same distance period of oscillation over a quarter cycle as does the non-linear cubic moment can be obtained by setting $X_L = X_N$ and algebraically solving for $(C_{m\alpha})_{eff}$, letting $(C_{m\alpha})_{eff}$ be equivalent to $C_{m\alpha}$ for the linear case. Then

---

* An analysis for the sinusoidal pitching moment $C_m(\theta) = M_r \sin(r\theta)$ can be found in Reference 61

$$(C_{m\alpha})_{eff} = \frac{\pi^2(C_{m\alpha} + r_m\theta_0^2)}{4[F(k, \frac{1}{2}\pi)]^2} \quad . \qquad (41)$$

The ratio of $(C_{m\alpha})_{eff}/C_{m\alpha}$ as a function of θ_0 with $C_{m\alpha}/r_m$ as a parameter appears in Figure 57.

Figure 57 (or Equation (41)) provides a convenient method for obtaining the coefficients of a cubic pitching moment from a set of experimental data. The value of $C_{m\alpha}$ at $\alpha = 0^o$ can be determined by extrapolating $(C_{m\alpha})_{eff}$ (as obtained from Equation (18)). Oscillation data for amplitudes near zero, say θ_0 = 2-3 deg, are required in addition to the large amplitude data. Then the ratios of experimental $(C_{m\alpha})_{eff}/C_{m\alpha}$ as a function of θ_0 may be calculated. The factor $C_{m\alpha}/r_m$ is then obtained by matching the equivalent $(C_{m\alpha})_{eff}/C_{m\alpha}$ curve in Figure 57 with the experimental ratio.

The derivation of the form of the dynamic stability term for the case of the cubic pitching moment is quite involved. The correction factor required in the reduction of dynamic stability data is generally small. Only the final results of the complete solution[60] will be given here. They are based upon the assumption that the lift and drag terms in the solution for the dynamic stability coefficient are not affected by the non-linearity of the pitching moment. Since these terms are second order, this is an acceptable simplification.

The dynamic stability data reduction equation for a cubic pitching moment is the same as Equation (28), except that a correction factor is included in the oscillation amplitude decay term. This correction factor, which can be expressed as a function of k^2, is shown in Figure 58 as a function of θ_0 with $C_{m\alpha}/r_m$ as a parameter. The dynamic stability equation is

$$(C_{mq} + C_{m\dot{\alpha}})\frac{md^2}{I} = R\,\frac{4m}{\rho A}\left(\frac{1}{X - X_0}\right)\log_e\left(\frac{\alpha_x}{\alpha_0}\right) + \left[C_{L\alpha} + 2\sum_{i=1}^{n}\left(\prod_{j=1}^{i+1}\frac{2j-1}{2j}\right)b_i\bar{\alpha}_0^{2i}\right] - \left[C_{D0} + 2\sum_{i=1}^{n}\frac{1}{2(i+1)}\left(\prod_{j=1}^{i}\frac{2j-1}{2j}\right)c_i\bar{\alpha}_0^{2i}\right] \quad , \qquad (42)$$

where

$$R = \frac{\frac{3}{2}k^2(1 - k^2)F(k, \frac{1}{2}\pi)}{[(1 + k^2)E(k, \frac{1}{2}\pi) - (1 - k^2)F(k, \frac{1}{2}\pi)]} \quad . \qquad (43)$$

6.4.3 Other Forms of the Non-Linear Pitching Moment

The destabilizing cubic form of a non-linear pitching moment gives the proper gross shape of a pitching moment over a wide range of angles of attack. But its form may not be applicable at the smaller angles of attack, say less than 30 deg. For example, a slender cone model will exhibit $C_{m\alpha}$ which increases in magnitude as the oscillation envelope increases to 30 deg (see Figure 14). In such a region, a stabilizing form of the cubic pitching moment is required; that is $r_m < 0$ in

$$C_m(\theta) = C_{m\alpha}\theta + 2r_m\theta^3 \quad . \tag{36}$$

As per Reference 63, the effect on the $(C_{m\alpha})_{eff}/C_{m\alpha}$ as a function of θ_0 is merely to make a "mirror image" about the $(C_{m\alpha})_{eff}/C_{m\alpha} = 1$ line of the curves in Figure 57. This "mirror image" assumption is good for $\theta_0 \leqslant 90$ deg and $|C_{m\alpha}/r_m| \geqslant 10$.

The effect of the stabilizing cubic term in the pitching moment on the damping parameter is significantly less than the effect of a destabilizing term. But, for $|C_{m\alpha}/r_m| \geqslant 10$ and $\theta_0 \leqslant 60$ deg , the "mirror image" about R = 1 of the curves in Figure 58 is an adequate approximation[63]. No more than a 1% error in the value of R will occur in this range of $C_{m\alpha}/r_m$ and θ_0 . Beyond these limits, the "mirror image" approximation becomes progressively worse.

A more universal form of a non-linear pitching moment would be a fifth-order equation. This will accomplish both pitching moment features of a slender cone: increasing pitching moment slope with increasing oscillation envelope for the lower range of angles; then decreasing pitching moment slope with further increase in oscillation angle, reaching a maximum value of stabilizing pitching moment near $\theta = 90$ deg . Information on free-flight data reduction for the quintic form of the non-linear pitching moment can be obtained from Reference 63.

6.5 Summary of Data Reduction Equations

6.5.1 Drag

$$C_D = -\frac{2m}{\rho A}\,\frac{d\left[\log_e\left(1 + \frac{V_m}{V_\infty}\right)\right]}{dX} \quad .$$

6.5.2 Pitching Moment Slope

$$(C_{m\alpha})_{eff} = -\frac{2I}{\rho A d}\,\Omega^2 \quad ,$$

where $\Omega = 2\pi \times$ oscillation cycles per unit distance .

6.5.3 Pitching Moment

Assuming cubic pitching moment in the form

$$C_m(\theta) = C_{m\alpha}\theta + 2r_m\theta^3 \quad ,$$

determine ratio of $C_{m\alpha}/r_m$ by matching equivalent $(C_{m\alpha})_{eff}/C_{m\alpha}$ curve in Figure 57 with $(C_{m\alpha})_{eff}/\left[(C_{m\alpha})_{eff}\right]_{\theta_0=0}$. The value of $\left[(C_{m\alpha})_{eff}\right]_{\theta_0=0}$ is determined by extrapolating experimental $(C_{m\alpha})_{eff}$ versus θ_0 curve to $\theta_0 = 0$. Oscillation data for amplitudes near zero, say θ_0 = 2-3 deg , is required in addition to the large amplitude data.

6.5.4 *Center of Pressure*

Obtain $(C_{m\alpha})_{eff}$ at the same oscillation amplitude for two or more locations of the model center of gravity. Then the distance of the center of pressure from the model nose is

$$(x_{cp})_{nose} = \frac{x_{cg1}(C_{m\alpha 2})_{eff} - x_{cg2}(C_{m\alpha 1})_{eff}}{(C_{m\alpha 2})_{eff} - (C_{m\alpha 1})_{eff}} ,$$

where the subscripts "1" and "2" refer to the two different center-of-gravity locations (measured from the model nose).

6.5.5 *Normal Force Slope*

Using the $(C_{m\alpha})_{eff}$ data obtained for determining the center-of-pressure location, the normal force slope coefficient is

$$(C_{N\alpha})_{eff} = \frac{d}{x_{cg1} - x_{cp}} (C_{m\alpha 1})_{eff} .$$

Due to the usual model mass characteristics, it is not practical to obtain directly the effective lift curve slope, $(C_{L\alpha})_{eff}$, because the amount model swerve is generally too small (see Table III) for sufficient accuracy.

6.5.6 *Dynamic Stability (Pitch Damping)*

General case: static aerodynamic coefficients are non-linear

$$C_m(\theta) = C_{m\alpha}\theta + 2r_m\theta^3$$

$$C_L = C_{L\alpha}\alpha + b_1\alpha^3 + b_2\alpha^5$$

$$C_D = C_{D0} + c_1\alpha^2 + c_2\alpha^4 .$$

Determine $(C_{m\alpha})_{eff}$ from oscillation frequency. If not practical to estimate rate of $C_{m\alpha}/r_m$ from $(C_{m\alpha})_{eff}$ data obtained as a function of θ_0, then use Newtonian Impact theory to estimate $C_{m\alpha}/r_m$. Use factor R (Fig. 58) on $\log_e(\alpha_x/\alpha_0)$ term to correct for non-linearity of pitching moment,

$$C_{mq} + C_{m\dot{\alpha}} = R\frac{4I}{\rho A d^2}\left(\frac{1}{X - X_0}\right)\log_e\left(\frac{\alpha_x}{\alpha_0}\right) + \frac{I}{md^2}\left(C_{L\alpha} + \tfrac{3}{4}b_1\bar{\alpha}_0^2 + \tfrac{5}{8}b_2\bar{\alpha}_0^4\right) - \frac{I}{md^2}\left(C_{D0} + \tfrac{1}{4}c_1\bar{\alpha}_0^2 + \tfrac{1}{8}c_2\bar{\alpha}_0^4\right) ,$$

where R is a function of both $C_{m\alpha}/r_m$ and $\bar{\alpha}_0$ (that is, θ_0).

In any case, the coefficient $(C_{mq} + C_{m\dot{\alpha}})$ is taken to be the effective average constant over an entire cycle of oscillation and generally does vary with the oscillation amplitude.

This damping coefficient equation reduces to the linear case simply by letting $R = 1$ and $b_1 = b_2 = c_1 = c_2 = 0$.

7. CONCLUDING REMARKS

This report presents free-flight testing procedures which are now operational. The emphasis has been on those techniques used in the Jet Propulsion Laboratory (JPL) continuous-flow supersonic and hypersonic wind tunnels[64]. The ideas and techniques described as relating to JPL are not necessarily unique nor original with JPL. It was just convenient to describe JPL's experience. Free-flight testing is currently being developed and used at several other establishments (see Table VI).

There are times when this free-flight technique is the most appropriate method for obtaining data. Under certain conditions it may be an expedient way for obtaining data, even though not the optimum approach. Also, it can serve to validate data obtained from models supported by some physical means. This testing technique is a valuable complement to all other useful techniques.

No attempt was made to enumerate all of the problems that have occurred in developing the techniques. Nor have all the alternate approaches, which have been either considered or used, been mentioned. Further detailed information on the use of this rapidly advancing testing technique along with typical results can be found in the included references.

REFERENCES

1. Zimmerman, C.H. — *Preliminary Tests in the NACA Free-Spinning Tunnel.* (Langley). Technical Report 557, 1936.

2. Campbell, John P. — *Free and Semi-Free Model Flight-Testing Techniques Used in Low-Speed Studies of Dynamic Stability and Control.* AGARDograph 79, October 1963.

3. May, Albert; Witt, W.R. Jr — *Free-Flight Determinations of the Drag Coefficients of Spheres.* (NOL). Journal of the Aeronautical Sciences, Vol.20, September 1953.

4. Murphy, C.H.; Nicolaides, J.D. — *A Generalized Ballistic Force System.* USA Ballistics Research Laboratories, BRL Report 933, May 1955.

5. Short, Barbara J.; Sommer, Simon C. — *Some Measurements of the Dynamic and Static Stability of Two Blunt-Nosed, Low-Fineness-Ratio Bodies of Revolution in Free-Flight at M = 4.* (Ames). NASA TM X-20, 1959.

6. Bull, G.V. — *Hypervelocity Research in the CARDE Free Flight Ranges.* Galbraith Building Opening Ceremonies, University of Toronto, 1961.

7. Lyons, W.C. Jr et al. — *Hypersonic Drag, Stability, and Wake Data for Cones and Spheres.* AIAA Preprint 64-44, (presented at the AIAA Aerospace Meeting, New York, January 1964). Also AIAA Journal, Vol.2, November 1964, pp.1948-1956.

8. Slattery, R.E., Clay, W.G. — *Width of the Turbulent Trail Behind a Hyper-velocity Sphere.* (MIT). Physics of Fluids, Vol.4, 1961, pp.1199-1201.

9. - — *Hypervelocity Range Research Program.* General Motors Corp., Defense Research Laboratories, Aerospace Operations Department, Report DA-04-495-ORD-3567, January 1963.

10. Pallone, A.J. et al. — *Hypersonic Laminar Wakes and Transition Studies.* AIAA Preprint 63-171, June 1963.

11. Gates, D.F., Bixler, D.N. — *The Measurement of Aerodynamic Forces and Moments in the NOL 4-in. Hypersonic Shock Tunnel No.3.* United States Naval Ordnance Laboratory, White Oak, Maryland, NOLTR-6-100, September 1961.

12. Geiger, Richard E. — *Experimental Lift and Drag of a Series of Glide Configurations at Mach Numbers 12, 6 and 17.5.* (GE). Journal of the Aerospace Sciences, Vol.29, April 1962.

13. Bloxsom, D.E., Rhodes, B.V. — *Experimental Effect of Bluntness and Gas Rarefaction on Drag Coefficients and Stagnation Heat Transfer on Axi-symmetric Shapes in Hypersonic Flow.* Journal of the Aerospace Sciences, Vol.29, December 1962.

14. Lukasiewicz, J., Jackson, R., van der Bliek, J.A. — Arnold Engineering Development Center
Hanes, W.G., Miller, R.M. — Boeing, Seattle
Development of Capacitance and Inductance Driven Hotshot Tunnels. Paper presented at the 1960 Hypervelocity Technique Symposium, University of Denver.

15. Kinslow, M., Potter, J.L. — *Drag of Spheres in Rarefied Hypervelocity Flow.* AIAA Journal, Vol.I, November 1963, pp.2467-2473.

16. Nelson, R.L. — *Measurement of Aerodynamic Characteristics of Re-Entry Configurations in Free Flight at Hypersonic and Near-Orbital Speeds.* Technical Report 6-90-61-37, Lockheed Missiles and Space Division, Sunnyvale, California, July 1961.

17. Shafrir, Uri
McDonald, Gordon
Use of Sky-Diving Technique (prior to parachute deployment) for Observing Free-Fall Spheres. Geophysics Department, University of California at Los Angeles, Private Communiqué, July 1964.

18. Holmes, F.T.
Axial Magnetic Suspensions. Review of Scientific Instruments, Vol.8, November 1937, pp.444-447 (also Physical Review, Vol.51, 1937, p.689).

19. Tournier, M.
Laurenceau, P.
Perfectionnements a la Suspension Magnetique des Maquettes (Improvement in the Magnetic Suspension of Models). ONERA NT 5/1579 AP, Paris, December 1956.

20. Parker, H.M.
et al.
An Electromagnetic Suspension System for the Measurement of Aerodynamic Characteristics. University of Virginia, Report AST-4443-106-62U, Contract AF 49(638)-1022, March 1962 (also AFOSR 2294).

21. Covert, E.E.
Tilton, E.L. III
Calibration of a Magnetic Balance System for Drag, Lift, and Pitching Moment. Massachusetts Institute of Technology, Aerophysics Laboratory, May 1963.

22. Dubois, G.
Rouge, C.
On a Method for Measuring the Base Pressure. ONERA La Recherche Aeronautique, Vol.79, November-December 1960 (translated by University of Virginia, Report AST-4443-102-61U, May 1961. Also AFOSR 1020 and ASTIA AD-260634).

23. Clemens, P.L.
Radio Telemetry of Stagnation Pressure from a Wind Tunnel Model Magnetically Supported in Supersonic Flow. Arnold Engineering Development Center, AEDC-TDR-62-141, July 1962.

24. Zapata, R
Dukes, T.
Electromagnetic Suspension for Holding Spherical Models in a Hypersonic Wind Tunnel. Princeton University, Department of Aeronautical and Mechanical Sciences, 1964.

25. Auriol
Flon
Détermination du Coefficient de Traînée de Spheres en vol Libre dans une Soufflerie (Drag Coefficient Determination of a Free-Flight Sphere in a Wind Tunnel). No.E-804-NT3 R4, Laboratoire de Recherches Balistiques et Aerodynamiques, Vernon, Octobre 1954.

26. Fox, N.L.
Blaylock, R.B.
Blunt-Nose Cylinder Flare Studies. Space Program Summary No.37-22, Vol.IV, Jet Propulsion Laboratory, Pasadena, June-July 1963, pp.74-75.

27. -
Equations, Tables, and Charts for Compressible Flow. NACA Report 1135, Ames Aeronautical Laboratory, 1953.

28. Dayman, B. — *Definitive Interference-Free Experimental Studies of Vehicle Motion.* AIAA Preprint 64-476, June 1964.

29. Seiff, Alvin — *A New Method for Computing Drag Coefficients from Ballistic Range Data.* Journal of the Aeronautical Sciences, Vol.25, February 1958, pp.133-134.

30. Jaffe, Peter; Prislin, Robert H. — *Effect of Boundary-Layer Transition on Dynamic Stability over Large Amplitudes of Oscillation.* AIAA Paper 64-427, June 1964. Also, *Effect of Boundary-Layer Transition on Dynamic Stability.* Journal of Spacecraft and Rockets, Vol.3, January 1966, pp.46-52.

31. Dayman, Bain, Jr — *Free-Flight Hypersonic Viscous Effects on Slender Cones.* AIAA Preprint 64-46. Also, *Hypersonic Viscous Effects on Free-Flight Slender Cones.* AIAA Journal, Vol.3, August 1965, pp.1391-1400.

32. Ashkenas, H. — *Calibration of the JPL Low Density Supersonic Wind Tunnel.* Private communication, Jet Propulsion Laboratory, Pasadena, California, August 1963.

33. Dayman, Bain, Jr — *Saturn Free Flight.* Space Program Summary No.37-31, Vol.IV, Jet Propulsion Laboratory, Pasadena, California, December 1964 - January 1965, pp.138-139.

34. Lun , D.E. — *Saturn Cold-Wall Studies.* Space Program Summary No.37-34, Vol.IV, Jet Propulsion Laboratory, Pasadena, California, June-July 1965, p.105.

35. Holway, H.P. — *Tandem Model Release for Free-Flight Testing.* Space Program Summary No.37-37, Vol.IV, Jet Propulsion Laboratory, Pasadena, California, December 1965 - January 1966.

36. Goranson, G.M. — *Free-Flight Wind Tunnel Studies of Drogue Devices for Supersonic Drag and Stabilization.* Technical Memorandum, Jet Propulsion Laboratory, Pasadena, California (to be published in 1966).

37. Hiller, R.C.; Harrison, R.G. Jr — *Interference-Free Base Pressure Measurements.* Space Program Summary No.37-28, Vol.IV, Jet Propulsion Laboratory, Pasadena, California, June-July 1964, pp.52-54.

38. Welton, John T. — *Free-Flight Telemetry Testing in the Jet Propulsion Laboratory Wind Tunnels.* Technical Report 32-775. Jet Propulsion Laboratory, Pasadena, California, September 1965.

39. Dayman, Bain, Jr — *Optical Free-Flight Wake Studies.* Technical Report 32-364, Jet Propulsion Laboratory, Pasadena, California, November 1962.

40. Dayman, Bain, Jr — *Support Interference Effects on the Supersonic Wake.* AIAA Journal Technical Note, Vol.1, August 1963, pp.1921-1923.

41. Laumann, E.A. — *The Wakes of Wire Supported Models.* Space Program Summary No.37-37, Vol.IV, Jet Propulsion Laboratory, Pasadena, California, December 1965 - January 1966.

42. Herrera, J.G. — *Free-Fall Model Wake Surveys.* Space Program Summary No.37-25, Vol.IV, Jet Propulsion Laboratory, Pasadena, California, December 1963 - January 1964.

43. Dayman, Bain, Jr — *Simplified Free-Flight Testing in a Conventional Wind Tunnel.* Technical Report 32-346, Jet Propulsion Laboratory, Pasadena, October 1962.

44. Stollenwerk, E. — *Wire-Release of Free-Flight Models by Use of Electrical Energy to Sever Wires at Localized Areas.* Private communication, Lockheed-California Company, March 1966.

45. Holway, H.P. et al. — *A Pneumatic Model Launcher for Free-Flight Testing in a Conventional Wind Tunnel.* Technical Memorandum 33-177, Jet Propulsion Laboratory, Pasadena, March 1964.

46. Platou, Anders S. — *Free Flight Wind Tunnel Techniques at the Ballistic Research Laboratories, Aberdeen Proving Ground.* Transactions of the Second Technical Workshop on Dynamic Stability Testing, Vol.II, Arnold Engineering Development Center, Arnold Air Force Station, Tennessee, April 1965.

47. Hodapp, A.E. Jr — *A Model Launcher for Free Flight Wind Tunnel Measurements.* Arnold Engineering Development Center. Private communication, November 1965.

48. Holway, H.P., Prislin, R.H. — *Techniques for Launching Spinning Free-Flight Models in a Conventional Wind Tunnel.* Space Program Summary No.37-38, Vol.IV, Jet Propulsion Laboratory, Pasadena, California, February-March 1966.

49. Iandolo, J. et al. — *Instrumentation, Techniques and Equations Used at the Naval Ordnance Laboratory for the Determination of Dynamic Derivatives in the Wind Tunnel.* NOLTR 66-23 Aeronautical Research Report 258, 1966.

50. Platou, Anders S. — *Launch System for Spinning Free-Flight Models.* Private communication, Ballistic Research Laboratories, Aberdeen Proving Ground, March 1966.

51. Ward, L.K. — *A Model Drop Technique for Free Flight Wind Tunnel Measurements Using Telemetry.* Private communication, Arnold Engineering Development Center, November 1965.

52. Cumming, D.P. — *Development of a System for the Launch and Recovery of Larger Instrumented Free-Flight Models in a High Speed Wind Tunnel.* Private communication, General Dynamics/Convair, March 1966.

53. Levy, Lionel L. Jr; Fletcher, Leroy S. — *Free-Flight Aerodynamics of a Blunt-Faced Re-entry Shape with and without Ablation.* AIAA Preprint 66-61, January 1966.

54. Marks, Lionel S. — *Mechanical Engineers' Handbook.* Sixth Edition, McGraw-Hill, New York, 1958.

55. Myers, Jack A. — *Handbook of Equations for Mass and Area Properties of Various Geometrical Shapes.* NAVWEPS Report 7827, US Naval Ordnance Test Station, China Lake, April 1962.

56. Peterson, Victor L. — *Measurement of Aerodynamic Characteristics of Bodies Free-Flying in a Wind Tunnel using Data Telemetered from Onboard Accelerometers.* Private communication, NASA Ames Research Center, February 1966.

57. Prislin, R.H.; Holway, H.P. — *Non-Planar Free-Flight Testing in a Conventional Wind Tunnel.* Space Program Summary No.37-37, Vol.IV, Jet Propulsion Laboratory, Pasadena, California, December 1965 - January 1966.

58. Harrison, R.G. Jr — *A Pressure Telemeter for Wind Tunnel Free Flight Pressure Measurement.* Technical Report 32-763, Jet Propulsion Laboratory, Pasadena, California, December 1965.

59. McDevitt, John B. et al. — *Measurement of Pressures and Heat Transfer by FM Telemetry from Free-Flying Models in Hypersonic Tunnel Streams.* Proceedings of the First International Congress on Instrumentation in Aerospace Simulation Facilities, Paris, France, September 1964.

60. Prislin, R.H. — *The Free-Flight and Free-Oscillation Techniques for Wind Tunnel Dynamic Stability Testing.* Technical Report 32-878, Jet Propulsion Laboratory, Pasadena, California, January 1966.

61. Jaffe, Peter — *Obtaining Free-Flight Dynamic Damping of an Axially Symmetric Body (at all Angles-of-Attack) in a Conventional Wind Tunnel.* Technical Report 32-544, Jet Propulsion Laboratory, Pasadena, California, January 1964.

62. Jaffe, Peter — *A Generalized Approach to Dynamic-Stability Flight Analysis.* Technical Report 32-757, Jet Propulsion Laboratory, Pasadena, July 1965.

63. Prislin, R.H. — *Corrections to Free-Flight Data Reduction for Various Forms of Non-Linear Pitching Moment.* Private communication, Jet Propulsion Laboratory, February 1966.

64. – *Wind Tunnel Facilities at the Jet Propulsion Laboratory.* Technical Release No. 34-257, January 1962.

TABLE I

Analytical Comparison of Base Drag to Total Cone Drag

($\alpha = 0^o$)

Cone half-angle (deg)	M	C_{DP} (Form drag[27])	C_{DB} (Base Drag)	C_{DOT} (Total Drag)	C_{DB}/C_{DOT}
10	1.25	0.144	0.457	0.601	0.76
	2	0.104	0.179	0.283	0.63
	5	0.074	0.029	0.103	0.28
	10	0.066	0.007	0.073	0.10
	20	0.064	0.002	0.066	0.03
20	1.25	0.489	0.457	0.946	0.48
	2	0.325	0.179	0.504	0.36
	5	0.259	0.029	0.288	0.10
	10	0.250	0.007	0.257	0.03
	20	0.248	0.002	0.250	0.01

TABLE II

Example Free-Flight Model Mass Characteristics and Trajectory Parameters

Parameter	*Model Types*						
	(A)				(B)		
d (in.)	0.5	0.5	1	2	0.5	1	2
W (gm)	2	2	16	128	0.34	2.8	22
m ($in.^{-1}$ lb sec^2)	1.1×10^{-5}	1.1×10^{-5}	9.1×10^{-5}	7.3×10^{-4}	2.0×10^{-6}	1.6×10^{-5}	1.3×10^{-4}
I (in. lb sec^2)	1.9×10^{-7}	1.9×10^{-7}	6.1×10^{-6}	1.95×10^{-4}	4.9×10^{-7}	1.6×10^{-5}	5.0×10^{-4}
m/I ($in.^{-2}$)	60	60	15	3.75	4	1	0.25
q (lb/$in.^2$)	0.3	3	3	3	3	3	3
a/g	1.5	15	7.4	3.7	86	43	21
V_m (ft/sec)	14	44	31	22	105	74	52
t (sec)	0.029	0.092	0.13	0.18	0.038	0.054	0.076
N (cycles)	17	17	12	8.5	4.4	3.1	2.2
f (c/s)	58	182	91	45	115	57	29
Δy (in.)	0.012	0.012	0.026	0.052	0.20	0.40	0.80
$(\alpha_t/\alpha_0)_{env}$ due to:							
Dynamics Term	0.62	0.22	0.34	0.47	0.77	0.85	0.88
Static Term	0.97	0.92	0.94	0.96	0.83	0.87	0.91
Total	0.60	0.20	0.32	0.45	0.64	0.74	0.80

TABLE III

Typical Conditions for Wire-Release System

Material	*Diameter* (in.)	*Notch Depth* (in.)	*Notch Temperature* (°F)	T_0 (°F)	*Preload* (lb)	*Impulse Load* (lb)
17-9PH Stainless Steel Wire	0.008	0.003	0 to Adiabatic	1000	3	10
↓	0.012	0.005	0 to Adiabatic	1000	7	21
	0.020	0.004	-320	600	50	30
	0.020	0.004	Adiabatic	600	27	25
	0.024	0.007	100	600	75	30
	0.024	0.007	Adiabatic	600	30	30
	0.026	0.010	-32	600	60	30
	0.026	0.006	100	600	50	30
	0.026	0.006	Adiabatic	1000	32	25
321 Stainless Steel Tube	0.036*	0.003†	0	600	30	30
(0.006 wall)	0.036*	0.003†	Adiabatic	600	20	30

* Internally cooled with 50 lb/in.^{2} gauge room temperature nitrogen gas at tube inlet

† Circumferential notch

TABLE IV

Properties of Some Common Materials
(from Reference 54)

Material	*Density* (lb/in.^{3})	*Specific Heat* (Btu/lb °F) *at Room Temperature*	*Thermal Conductivity* (Btu/ft^2 h in. °F)	*Linear Coefficient of Thermal Expansion per* °F × 10^{-6}	*Melting Temperature* (°F)
Polyurethane foam (2 lb/ft^3 mix)	0.003*				
Water	0.036				
Styrene	0.040				
Silastic rubber	0.041				
Magnesium	0.063	0.249	1100	14	1202
Beryllium	0.066	0.425	1100	7	2340
Aluminum	0.098	0.226	1740	13	1220
Antimony	0.239	0.049	131	5-6	1167
Zinc	0.258	0.093	784	9-22	787
Chromium	0.260	0.120	464	3½	3350
Tin	0.264	0.055	464	13	450
Iron	0.284	0.108	120-320	6½	2802
Cadmium	0.313	0.055	639	16½	610
Nickel	0.322	0.112	639	7½	2651
Copper	0.324	0.092	2730	9	1981
Silver	0.379	0.056	2900	11	1760
Lead	0.410	0.030	241	16	621
Mercury	0.490	0.033	58	34	-38
Uranium	0.687	0.028	186	11½	2065
Tungsten	0.697	0.034	900	2½	6150
Gold	0.698	0.031	206	8	1945
Platinum	0.775	0.032	494	5	3224

* The average density of molded models from the 2 lb/ft^3 mix is about 6 lb/ft^3

232

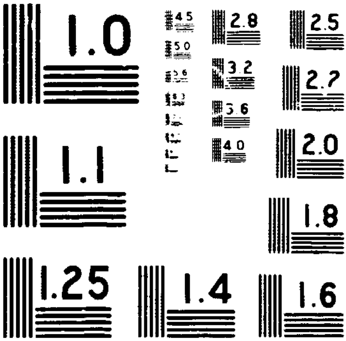

MICROCOPY RESOLUTION TEST CHART

NATIONAL BUREAU OF STANDARDS-1963

TABLE V

Sample Tabulation of Free-Flight Trajectory Data

TEST NO. 20-590 RUN NO. 13

Frame No.	Smooth t (sec)	X (ft)	Raw α (deg)	Smooth α (deg)	Raw x (in.)	Smooth x (in.)	Raw y (in.)	Smooth y (in.)	V_m (in./sec)	$\ln\left(1 + \frac{V_m}{V_e}\right)$
0.	0.	-0.00	0.1	-0.1	0.	0.02	0.	0.00	-620.0	0.022460
2.	0.000455	1.06	4.4	4.2	-0.27	-0.26	-0.03	-0.02	-623.5	0.022409
4.	0.000910	2.12	7.2	8.2	-0.53	-0.54	-0.02	-0.04	-618.9	0.022330
6.	0.001364	3.18	11.7	11.8	-0.83	-0.92	-0.06	-0.06	-614.4	0.022177
8.	0.001818	4.24	16.0	15.4	-1.08	-1.10	-0.08	-0.08	-609.9	0.022016
10.	0.002273	5.30	18.2	18.2	-1.36	-1.38	-0.10	-0.09	-605.4	0.021894
12.	0.002727	6.36	20.2	20.0	-1.65	-1.65	-0.09	-0.09	-600.9	0.021693
14.	0.003182	7.43	20.4	21.1	-1.94	-1.92	-0.09	-0.10	-596.4	0.021532
16.	0.003638	8.49	22.0	21.6	-2.19	-2.20	-0.12	-0.12	-591.8	0.021370
18.	0.004096	9.56	21.9	21.6	-2.46	-2.47	-0.14	-0.13	-587.5	0.021213
20.	0.004553	10.62	20.7	21.4	-2.74	-2.73	-0.14	-0.14	-583.3	0.021066
22.	0.005011	11.69	20.4	20.1	-3.00	-3.00	-0.14	-0.14	-578.9	0.020900
24.	0.005465	12.75	18.9	18.6	-3.25	-3.26	-0.12	-0.13	-574.6	0.020733
26.	0.005915	13.80	15.8	16.3	-3.50	-3.52	-0.14	-0.13	-569.8	0.020584
28.	[illegible]	14.85	13.6	12.8	-3.78	-3.78	-0.13	-0.13	-565.1	0.020415
30.	0.006813	15.89	9.0	9.3	-4.05	-4.03	-0.12	-0.12	-560.4	0.020247
32.	0.007262	16.94	5.4	6.1	-4.28	-4.28	-0.11	-0.11	-555.8	0.020083
34.	0.007714	17.99	3.3	3.0	-4.53	-4.53	-0.07	-0.09	-551.2	0.019916
36.	0.008168	19.05	0.4	0.0	-4.79	-4.78	-0.11	-0.08	-546.8	0.019759
38.	0.008622	20.11	-3.4	-3.3	-5.02	-5.02	-0.05	-0.06	-543.3	0.019633
40.	0.009077	21.16	-7.2	-7.3	-5.27	-5.27	-0.06	-0.05	-539.7	0.019507
42.	0.009529	22.22	-11.0	-11.0	-5.50	-5.51	-0.03	-0.05	-536.2	0.019381
44.	0.009978	23.26	-14.5	-14.1	-5.74	-5.75	-0.05	-0.06	-532.0	0.019230
46.	0.010429	24.30	-16.2	-16.3	-6.00	-5.99	-0.09	-0.06	-527.7	0.019077
48.	0.010873	25.35	-18.0	-17.9	-6.20	-6.23	-0.05	-0.06	-523.5	0.018926
50.	0.011321	26.39	-18.9	-19.1	-6.46	-6.46	-0.03	-0.04	-518.7	0.018785
52.	0.011770	27.43	-20.4	-20.5	-6.67	-6.69	-0.03	-0.02	-513.4	0.018565
54.	0.012221	28.48	-21.2	-21.4	-6.93	-6.92	-0.03	-0.04	-507.8	0.018364
56.	0.012671	29.53	-22.2	-21.7	-7.15	-7.15	-0.06	-0.06	-502.4	0.018171
58.	0.013121	30.57	-20.5	-20.4	-7.40	-7.37	-0.10	-0.08	-496.9	0.017974
60.	0.013570	31.62	-18.1	-17.9	-7.59	-7.60	-0.08	-0.09	-491.1	0.017765
62.	0.014019	32.66	-14.3	-14.0	-7.82	-7.82	-0.09	-0.09	-484.7	0.017533
64.	0.014467	33.70	-11.6	-11.8	-8.05	-8.03	-0.10	-0.10	-478.3	0.017307
66.	0.014914	34.74	-9.8	-8.9	-8.27	-8.26	-0.12	-0.12	-472.5	0.017089
68.	0.015362	35.78	-6.3	-6.1	-8.46	-8.46	-0.16	-0.14	-468.6	0.016891
70.	0.015810	36.82	-2.9	-2.8	-8.64	-8.66	-0.16	-0.16	-460.8	0.016692
72.	0.016258	37.86	0.7	0.4	-8.86	-8.87	-0.19	-0.18	-456.1	0.016510
74.	0.016706	38.90	3.8	3.6	-9.07	-9.07	-0.19	-0.21	-451.6	0.016300
76.	0.017153	39.94	6.7	6.9	-9.27	-9.27	-0.22	-0.22	-447.6	0.016080
78.	0.017600	40.98	10.1	9.9	-9.45	-9.47	-0.27	-0.25	-444.0	0.016076
80.	0.018048	42.02	13.5	13.1	-9.66	-9.67	-0.27	-0.27	-436.8	0.015930
82.	0.018496	43.05	15.3	16.1	-9.87	-9.86	-0.26	-0.28	-436.9	0.015520
84.	0.018944	44.09	18.3	18.2	-10.06	-10.06	-0.31	-0.29	-433.7	0.015705
86.	0.019392	45.13	20.1	19.7	-10.25	-10.25	-0.30	-0.30	-430.8	0.015500
88.	0.019840	46.17	20.2	20.7	-10.43	-10.44	-0.30	-0.31	-427.5	0.015403
90.	0.020286	47.21	20.6	20.6	-10.62	-10.62	-0.31	-0.33	-424.0	0.015207
92.	0.020734	48.24	20.	20.3	-10.82	-10.82	-0.33	-0.33	-420.6	0.015127
94.	0.021180	49.28	19.0	19.4	-11.03	-11.01	-0.33	-0.33	-417.1	0.015100
96.	0.021626	50.31	19.2	17.7	-11.22	-11.20	-0.32	-0.32	-413.8	0.014977
98.	0.022072	51.35	17.2	15.4	-11.37	-11.38	-0.33	-0.33	-409.0	0.014813
100.	0.022519	52.38	12.6	12.8	-11.57	-11.56	-0.32	-0.32	-404.8	0.014403
102.	0.022964	53.41	9.9	9.7	-11.73	-11.74	-0.36	-0.33	-400.2	0.014501
104.	0.023409	54.44	6.6	6.5	-11.92	-11.92	-0.32	-0.33	-396.5	0.014359
106.	0.023854	55.47	3.0	3.6	-12.08	-12.09	-0.32	-0.31	-392.5	0.014216
108.	0.024299	56.50	0.	0.1	-12.26	-12.26	-0.30	-0.28	-390.1	0.014067
110.	0.024745	57.54	-2.7	-3.4	-12.42	-12.44	-0.28	-0.28	-384.4	0.013911
112.	0.025191	58.57	-6.9	-6.3	-12.62	-12.61	-0.26	-0.27	-381.1	0.013813
114.	0.025637	59.60	-10.0	-9.3	-12.74	-12.78	-0.26	-0.26	-378.2	0.013693
116.	0.026082	60.63	-11.7	-12.2	-12.96	-12.96	-0.26	-0.26	-374.0	0.013548
118.	0.026526	61.66	-14.1	-14.0	-13.11	-13.11	-0.27	-0.27	-371.1	0.013404
120.	0.026970	62.69	-17.0	-15.8	-13.27	-13.27	-0.27	-0.27	-367.1	0.013281
122.	0.027413	63.71	-17.0	-17.3	-13.47	-13.45	-0.27	-0.27	-363.3	0.013100
124.	0.027856	64.74	-19.1	-18.9	-13.59	-13.60	-0.27	-0.26	-356.0	0.012980
126.	0.028300	65.76	-19.3	-19.5	-13.76	-13.76	-0.28	-0.26	-352.5	0.012784
128.	0.028744	66.79	-19.1	-19.6	-13.93	-13.94	-0.26	-0.26	-346.6	0.012645
130.	0.029187	67.82	-19.1	-19.3	-14.09	-14.06	-0.28	-0.28	-344.0	0.012531
132.	0.029679	68.84	-17.7	-18.1	-14.23	-14.21	-0.30	-0.30	-335.0	0.012211
134.	0.030070	69.86	-16.1	-16.0	-14.36	-14.36	-0.35	-0.32	-329.1	0.011930
136.	0.030511	70.88	-13.5	-13.8	-14.51	-14.50	-0.33	-0.31	-323.1	0.011730
138.	0.030952	71.89	-10.8	-11.0	-14.66	-14.65	-0.32	-0.31	-317.3	0.011516
140.	0.031392	72.91	-8.2	-8.1	-14.81	-14.78	-0.32	-0.32	-311.8	0.011317
142.	0.031832	73.93	-5.1	-5.1	-14.91	-14.92	-0.34	-0.35	-306.9	0.011139
144.	0.032271	74.94	-2.2	-1.9	-15.04	-15.05	-0.38	-0.39	-302.5	0.010977
146.	0.032710	75.95	2.0	1.6	-15.16	-15.18	-0.44	-0.43	-298.0	0.010817
148.	0.033149	76.97	5.3	4.6	-15.31	-15.31	-0.47	-0.46	-294.6	0.010651
150.	0.033588	77.98	7.8	7.9	-15.44	-15.44	-0.47	-0.46	-291.1	0.010491
152.	0.034028	78.99	10.5	10.3	-15.57	-15.57	-0.47	-0.48	-289.7	0.010400
154.	0.034467	80.01	13.0	12.6	-15.69	-15.69	-0.52	-0.50	-287.1	0.010423
156.	0.034907	81.02	14.8	14.8	-15.82	-15.82	-0.50	-0.53	-284.6	0.010333
158.	0.035348	82.04	16.8	16.6	-15.94	-15.94	-0.55	-0.53	-282.4	0.010261
160.	0.035789	83.06	17.8	17.9	-16.06	-16.07	-0.59	-0.56	-279.2	0.010140
162.	0.036231	84.08	18.9	19.1	-16.14	-16.19	-0.56	-0.57	-276.2	0.010030
164.	0.036673	85.10	20.2	19.8	-16.29	-16.31	-0.55	-0.55	-272.5	0.009895
166.	0.037114	86.11	19.3	19.6	-16.43	-16.43	-0.55	-0.55	-268.5	0.009759
168.	0.037556	87.13	19.8	19.0	-16.55	-16.55	-0.56	-0.56	-264.8	0.009619
170.	0.037995	88.14	17.3	17.3	-16.70	-16.67	-0.55	-0.55	-261.1	0.009466
172.	0.038435	89.16	15.6	15.2	-16.80	-16.78	-0.55	-0.57	-257.7	0.009340
174.	0.038875	90.17	12.8	12.5	-16.89	-16.89	-0.55	-0.57	-254.4	0.009242
176.	0.039314	91.18	9.7	9.6	-17.00	-17.00	-0.57	-0.57	-251.1	0.009124
178.	0.039752	92.19	7.8	6.7	-17.13	-17.11	-0.57	-0.56	-247.5	0.008992
180.	0.040190	93.20	4.2	3.7	-17.22	-17.22	-0.61	-0.58	-243.6	0.008850
182.	0.040627	94.21	0.	0.5	-17.32	-17.33	-0.58	-0.57	-239.1	0.008688
184.	0.041063	95.21	-2.8	-2.6	-17.42	-17.43	-0.57	-0.56	-234.6	0.008525
186.	0.041500	96.22	-5.0	-5.4	-17.50	-17.53	-0.55	-0.55	-230.0	0.008356
188.	0.041936	97.22	-7.8	-7.6	-17.61	-17.63	-0.54	-0.56	-225.9	0.008209
190.	0.042372	98.23	-10.2	-10.1	-17.74	-17.73	-0.55	-0.56	-222.0	0.008070
192.	0.042807	99.23	-12.0	-12.5	-17.86	-17.87	-0.55	-0.56	-218.3	0.007943
194.	0.043243	100.23	-15.0	-14.5	-17.93	-17.93	-0.58	-0.56	-215.1	0.007820
196.	0.043680	101.74	-16.7	-16.7	-18.01	-18.01	-0.58	-0.56	-211.8	0.007701
198.	0.044117	102.74	-18.1	-18.3	-18.11	-18.10	-0.54	-0.56	-208.2	0.007570
200.	0.044555	103.25	-19.5	-19.3	-18.22	-18.19	-0.57	-0.57	-203.0	0.007409
202.	0.044994	104.26	-19.9	-19.6	-18.28	-18.28	-0.57	-0.57	-198.7	0.007225
204.	0.045432	105.27	-19.6	-19.3	-18.37	-18.37	-0.60	-0.59	-192.7	0.007010
206.	0.045870	106.27	-18.8	-18.2	-18.45	-18.45	-0.60	-0.60	-186.7	0.006791
208.	0.046309	107.28	-17.8	-17.1	-18.55	-18.54	-0.62	-0.62	-180.6	0.006560
210.	0.046747	108.29	-15.6	-15.7	-18.60	-18.61	-0.62	-0.63	-174.7	0.006394
212.	0.047185	109.30	-14.5	-14.1	-18.70	-18.69	-0.61	-0.63	-168.9	0.006104
214.	0.047619	110.29	-11.9	-11.7	-18.77	-18.76	-0.64	-0.65	-163.6	0.005993
216.	0.048055	111.29	-8.5	-8.7	-18.89	-18.83	-0.69	-0.66	-159.0	0.005700
218.	0.048486	112.28	-5.2	-5.3	-18.90	-18.90	-0.70	-0.71	-155.2	0.005600
220.	0.048915	113.27	-1.9	-2.1	-18.96	-18.96	-0.74	-0.74	-151.8	0.005526
222.	0.049346	114.26	0.4	0.7	-19.06	-19.02	-0.76	-0.75	-148.4	0.005401
224.	0.049779	115.25	3.5	3.5	-19.09	-19.09	-0.77	-0.77	-145.0	0.005277
226.	0.050212	116.25	6.1	6.3	-19.14	-19.15	-0.76	-0.77	-141.7	0.005151
228.	0.050645	117.24	9.2	9.3	-19.20	-19.21	-0.79	-0.79	-138.7	0.005049
230.	0.051079	118.24	12.1	11.9	-19.29	-19.27	-0.79	-0.81	-134.0	0.004951
232.	0.051513	119.23	14.4	14.3	-19.32	-19.33	-0.86	-0.83	-133.3	0.004884
234.	0.051948	120.23	15.6	15.9	-19.38	-19.39	-0.89	-0.85	-130.6	0.004761
236.	0.052383	121.23	17.5	17.2	-19.49	-19.44	-0.86	-0.87	-128.5	0.004600
238.	[illegible]	122.23	17.0	18.2	-19.48	-19.50	-0.88	-0.88	-126.2	0.004599
240.	[illegible]	123.22	18.7	18.5	-19.56	-19.55	-0.90	-0.89	-124.0	0.004515
242.	0.053688	124.22	18.4	17.8	-19.59	-19.61	-0.90	-0.89	-121.0	0.004434
244.	0.054123	125.22	16.2	16.7	-19.68	-19.66	-0.89	-0.90	-119.2	0.004340
246.	0.054558	126.22	15.0	15.0	-19.72	-19.71	-0.90	-0.91	-116.3	0.004234
248.	0.054993	127.21	13.5	13.4	-19.75	-19.76	-0.94	-0.92	-113.2	0.004124
250.	0.055427	128.21	11.7	11.9	-19.81	-19.81	-0.93	-0.93	-109.9	0.004002
252.	0.055860	129.20	10.1	9.7	-19.86	-19.86	-0.93	-0.93	-106.3	0.003871
254.	0.056291	130.19	7.4	7.3	-19.91	-19.90	-0.91	-0.90	-102.3	0.003729
256.	0.056723	131.18	4.2	4.9	-19.94	-19.94	-0.88	-0.89	-97.7	0.003560
258.	0.057156	132.17	2.7	2.5	-19.99	-19.99	-0.88	-0.88	-93.2	0.003396
260.	0.057586	133.16	0.5	0.1	-20.02	-20.03	-0.90	-0.89	-89.0	0.003242
262.	0.058017	134.14	-2.7	-2.6	-20.06	-20.06	-0.89	-0.90	-86.9	0.003092
264.	0.058447	135.13	-5.7	-5.6	-20.09	-20.10	-0.91	-0.92	-81.0	0.002953
266.	0.058878	136.12	-8.7	-8.5	-20.15	-20.13	-0.93	-0.92	-77.2	0.002813
268.	0.059307	137.10	-10.8	-11.0	-20.17	-20.16	-0.95	-0.96	-73.3	0.002670
270.	0.059737	138.08	-13.1	-13.2	-20.21	-20.20	-0.91	-0.95	-69.6	0.002536
272.	0.060167	139.07	-15.2	-14.8	-20.23	-20.22	-0.90	-0.95	-66.0	0.002405
274.	0.060595	140.05	-16.0	-15.9	-20.26	-20.25	-0.94	-0.95	-62.1	0.002264
276.	0.061026	141.03	-16.4	-16.6	-20.29	-20.28	-0.94	-0.94	-58.0	0.002116
278.	0.061455	142.01	-16.8	-17.1	-20.29	-20.30	-0.92	-0.93	-53.3	0.001964
280.	0.061887	143.00	-17.6	-17.4	-20.31	-20.32	-0.95	-0.94	-48.1	0.001799
282.	0.062320	143.99	-18.1	-17.8	-20.34	-20.33	-0.95	-0.96	-42.9	0.001564
284.	0.062752	144.98	-17.2	-17.5	-20.34	-20.36	-1.00	-0.99	[illegible]	0.001377
286.	0.063185	145.97	-16.7	-16.5	-20.40	-20.38	-1.02	-1.03	-32.6	0.001181
288.	0.063615	146.95	-14.9	-14.9	-20.41	-20.39	-1.06	-1.05	-27.4	0.000998
290.	0.064046	147.94	-13.0	-12.9	-20.42	-20.40	-1.07	-1.06	-23.0	0.000830
292.	0.064478	148.92	-10.3	-10.2	-20.40	-20.41	-1.06	-1.08	-19.1	0.000697
294.	0.064906	149.90	-7.5	-7.4	-20.42	-20.42	-1.09	-1.08	-15.0	0.000577
296.	0.065333	150.88	-4.3	-4.8	-20.43	-20.42	-1.09	-1.09	-12.6	0.000452
298.	0.065762	151.86	-2.5	-2.4	-20.43	-20.43	-1.09	-1.11	-8.4	0.000305
300.	0.066191	152.84	-0.4	-0.1	-20.45	-20.43	-1.16	-1.14	-4.4	0.000159
302.	0.066620	153.82	2.1	2.6	-20.42	-20.43	-1.19	-1.19	-0.5	0.000018
304.	0.067047	154.79	5.2	4.9	-20.40	-20.43	-1.20	-1.24	3.6	-0.000126
306.	0.067476	155.77	8.1	7.8	-20.39	-20.43	-1.26	-1.27	7.3	-0.000267
308.	0.067904	156.75	9.5	10.4	-20.40	-20.42	-1.33	-1.30	10.8	-0.000395
310.	0.068332	157.73	13.1	12.3	-20.42	-20.42	-1.32	-1.33	14.0	-0.000513
312.	0.068760	158.70	14.0	13.8	-20.45	-20.41	-1.36	-1.37	17.1	-0.000621
314.	0.069188	159.68	14.7	15.6	-20.39	-20.40	-1.40	-1.38	19.9	-0.000720
316.	0.069617	160.66	16.2	16.4	-20.39	-20.39	-1.39	-1.40	22.0	-0.000794
318.	0.070046	161.64	17.9	17.2	-20.40	-20.38	-1.39	-1.40	25.7	-0.000937
320.	0.070475	162.62	17.6	17.3	-20.39	-20.37	-1.42	-1.39	28.7	-0.001077
322.	0.070903	163.59	16.1	16.7	-20.36	-20.36	-1.38	-1.38	31.9	-0.001169
324.	0.071330	164.57	15.7	15.7	-20.32	-20.34	-1.36	-1.39	35.5	-0.001299
326.	0.071756	165.54	14.6	14.5	-20.31	-20.33	-1.40	-1.40	39.1	-0.001479
328.	0.072180	166.50	13.3	13.0	-20.32	-20.31	-1.45	-1.42	42.0	-0.001564
330.	0.072605	167.47	10.7	11.0	-20.30	-20.29	-1.41	-1.44	46.4	-0.001695
332.	0.073029	168.44	8.7	8.7	-20.26	-20.27	-1.44	-1.44	49.8	-0.001819
334.	0.073453	169.41	6.6	6.2	-20.23	-20.25	-1.45	-1.43	53.0	-0.001935
336.	0.073878	170.37	3.6	3.7	-20.21	-20.23	-1.41	-1.42	55.7	-0.002036
338.	0.074301	171.34	1.2	1.4	-20.21	-20.20	-1.40	-1.41	58.0	-0.002120
340.	0.074725	172.30	-1.8	-1.8	-20.18	-20.18	-1.41	-1.40	60.1	-0.002197
342.	0.075148	173.27	-3.1	-3.4	-20.16	-20.15	-1.40	-1.41	62.6	-0.002287
344.	0.075573	174.24	-6.1	-5.9	-20.14	-20.12	-1.43	-1.43	65.7	-0.002399
346.	0.075999	175.21	-8.8	-8.9	-20.08	-20.10	-1.46	-1.46	69.2	-0.002527
348.	0.076427	176.18	-10.9	-11.0	-20.04	-20.07	-1.48	-1.48	72.9	-0.002665
350.	0.076854	177.15	-13.1	-13.0	-20.03	-20.03	-1.50	-1.49	77.2	-0.002820
352.	[illegible]	178.12	-14.8	-14.5	-20.00	-20.00	-1.46	-1.48	81.0	-0.002980
354.	0.077706	179.09	-15.3	-15.6	-19.96	-19.96	-1.49	-1.47	86.1	-0.003162
356.	0.078130	180.06	-16.2	-16.1	-19.96	-19.93	-1.55	-1.47	90.9	-0.003324
358.	0.078554	181.02	-16.4	-16.7	-19.90	-19.89	-1.47	-1.49	95.1	-0.003477
360.	0.078978	181.99	-16.4	-16.5	-19.86	-19.85	-1.50	-1.51	99.1	-0.003629
362.	0.079401	182.95	-16.2	-16.2	-19.82	-19.80	-1.55	-1.52	103.2	-0.003775
364.	0.079826	183.92	-16.0	-16.0	-19.77	-19.76	-1.52	-1.53	107.5	-0.003910
366.	0.080251	184.88	-15.1	-15.1	-19.73	-19.71	-1.51	-1.54	111.7	-0.004005
368.	0.080676	185.85	-14.6	-13.9	-19.69	-19.66	-1.58	-1.55	116.0	-0.004242
370.	0.081101	186.82	-11.9	-12.2	-19.61	-19.61	-1.59	-1.59	120.2	-0.004395
372.	0.081525	187.78	-10.2	-9.8	-19.53	-19.56	-1.61	-1.63	124.1	-0.004540
374.	0.081948	188.74	-7.2	-6.9	-19.49	-19.51	[illegible]	-1.64	127.7	-0.004671
376.	0.082371	189.70	-3.8	-4.4	-19.43	[illegible]	[illegible]	-1.66	130.9	-0.004789
378.	0.082794	190.66	-1.6	-1.8	-19.38	[illegible]	-1.65	-1.67	133.8	-0.004895
380.	0.083217	191.62	0.	0.6	-19.35	[illegible]	-1.69	-1.68	136.3	-0.004985
382.	0.083640	192.58	2.7	2.7	-19.30	[illegible]	-1.70	-1.71	138.6	-0.005072
384.	0.084063	193.55	5.4	5.0	-19.22	[illegible]	-1.74	-1.74	141.0	-0.005161
386.	0.084486	194.51	7.8	7.2	-19.15	[illegible]	-1.78	-1.77	143.3	-0.005246
388.	0.084909	195.47	9.2	9.1	-19.09	[illegible]	-1.86	-1.81	145.9	-0.005339
390.	0.085332	196.43	10.8	10.9	-19.03	-19.04	-1.84	-1.84	148.8	-0.005445
392.	0.085754	197.39	12.8	12.9	-18.94	-18.98	-1.87	-1.88	152.0	-0.005566
394.	0.086176	198.34	14.3	14.3	-18.89	-18.91	-1.92	-1.91	155.5	-0.005691
396.	0.086598	199.30	15.8	15.3	-18.87	-18.85	-1.96	-1.93	159.3	-0.005830
398.	0.087019	200.26	15.6	15.7	-18.78	-18.78	-1.95	-1.95	163.2	-0.005976

TABLE V (continued)

Sample Tabulation of Free-Flight Trajectory Data

TEST NO. 20-598 RUN NO. 13

Frame No.	Smooth t (sec)	X (ft)	Raw α (deg)	Smooth α (deg)	Raw x (in.)	Smooth x (in.)	Raw y (in.)	Smooth y (in.)	V_m (in./sec)	$\ln\left(1+\frac{V_m}{V_w}\right)$
400.	0.087441	201.22	15.3	15.7	-18.70	-18.71	-1.94	-1.96	167.3	-0.006126
402.	0.087864	202.18	15.5	15.2	-18.67	-18.64	-1.97	-1.96	171.5	-0.006277
404.	0.088287	203.14	14.5	14.6	-18.59	-18.56	-1.96	-1.96	175.4	-0.006423
406.	0.088710	204.10	13.3	13.4	-18.49	-18.49	-1.95	-1.96	179.3	-0.006564
408.	0.089133	205.05	12.1	11.8	-18.41	-18.41	-1.95	-1.95	183.0	-0.006703
410.	0.089554	206.01	9.9	10.0	-18.34	-18.33	-1.95	-1.95	186.7	-0.006837
412.	0.089973	206.96	7.9	8.3	-18.27	-18.25	-1.96	-1.97	190.5	-0.006977
414.	0.090392	207.91	6.6	6.5	-18.18	-18.17	-1.99	-1.98	194.5	-0.007116
416.	0.090810	208.86	5.1	4.5	-18.09	-18.09	-1.99	-1.99	197.8	-0.007246
418.	0.091228	209.80	2.1	2.2	-17.99	-18.01	-1.97	-1.99	201.5	-0.007379
420.	0.091648	210.76	-0.7	-0.1	-17.91	-17.92	-2.00	-1.98	205.1	-0.007513
422.	0.092068	211.71	-2.3	-2.4	-17.83	-17.84	-1.99	-1.99	208.7	-0.007646
424.	0.092489	212.66	-4.0	-4.7	-17.74	-17.75	-1.97	-2.00	212.1	-0.007772
426.	0.092910	213.62	-7.4	-7.0	-17.65	-17.66	-2.02	-2.00	215.4	-0.007894
428.	0.093331	214.57	-9.5	-9.4	-17.57	-17.57	-2.02	-2.01	218.7	-0.008012
430.	0.093751	215.52	-11.3	-11.4	-17.45	-17.47	-2.00	-2.01	222.0	-0.008134
432.	0.094170	216.47	-13.1	-12.7	-17.38	-17.38	-2.02	-2.01	225.4	-0.008259
434.	0.094589	217.42	-13.6	-14.0	-17.27	-17.29	-2.01	-2.02	228.7	-0.008382
436.	0.095007	218.37	-15.0	-15.3	-17.19	-17.19	-2.04	-2.04	232.0	-0.008505
438.	0.095427	219.32	-16.4	-16.3	-17.09	-17.09	-2.06	-2.05	235.4	-0.008627
440.	0.095848	220.27	-17.3	-16.9	-17.00	-16.99	-2.07	-2.07	238.4	-0.008741
442.	0.096271	221.23	-16.6	-16.7	-16.88	-16.89	-2.09	-2.08	241.8	-0.008865
444.	0.096692	222.18	-15.5	-15.7	-16.80	-16.79	-2.10	-2.10	244.9	-0.008977
446.	0.097113	223.13	-14.5	-14.4	-16.68	-16.68	-2.11	-2.12	248.0	-0.009092
448.	0.097532	224.08	-13.0	-13.1	-16.60	-16.58	-2.15	-2.13	251.2	-0.009209
450.	0.097949	225.02	-11.5	-11.8	-16.48	-16.47	-2.13	-2.15	254.3	-0.009325
452.	0.098363	225.96	-10.2	-9.9	-16.39	-16.37	-2.16	-2.17	257.6	-0.009437
454.	0.098778	226.90	-8.4	-7.9	-16.24	-16.26	-2.21	-2.20	260.5	-0.009552
456.	0.099192	227.83	-5.0	-5.7	-16.15	-16.15	-2.23	-2.23	263.6	-0.009666
458.	0.099608	228.77	-3.7	-3.6	-16.04	-16.04	-2.26	-2.26	266.7	-0.009782
460.	0.100024	229.72	-1.5	-1.5	-15.91	-15.93	-2.27	-2.28	269.9	-0.009898
462.	0.100441	230.66	0.1	0.4	-15.79	-15.82	-2.31	-2.31	273.1	-0.010017
464.	0.100858	231.60	2.9	2.7	-15.69	-15.70	-2.35	-2.33	276.3	-0.010134
466.	0.101275	232.54	5.1	5.2	-15.57	-15.58	-2.36	-2.36	279.5	-0.010252
468.	0.101692	233.49	7.5	7.5	-15.45	-15.47	-2.37	-2.38	282.7	-0.010371
470.	0.102110	234.43	9.6	9.4	-15.33	-15.35	-2.42	-2.41	285.9	-0.010491
472.	0.102527	235.37	11.0	11.0	-15.24	-15.23	-2.42	-2.44	289.1	-0.010606
474.	0.102945	236.32	12.1	12.2	-15.10	-15.11	-2.50	-2.48	292.1	-0.010720
476.	0.103363	237.26	13.2	13.4	-14.98	-14.98	-2.51	-2.51	295.2	-0.010833
478.	0.103783	238.21	14.4	14.3	-14.85	-14.86	-2.52	-2.54	298.3	-0.010947
480.	0.104203	239.16	15.0	14.8	-14.74	-14.73	-2.55	-2.55	301.4	-0.011061
482.	0.104621	240.10	14.9	15.0	-14.62	-14.61	-2.57	-2.56	304.4	-0.011171
484.	0.105040	241.05	14.6	14.8	-14.49	-14.48	-2.56	-2.57	307.4	-0.011283
486.	0.105458	241.99	14.3	14.1	-14.35	-14.35	-2.56	-2.58	310.5	-0.011398
488.	0.105875	242.93	13.3	13.2	-14.22	-14.22	-2.60	-2.59	313.6	-0.011512
490.	0.106292	243.87	11.8	12.0	-14.07	-14.09	-2.61	-2.61	317.0	-0.011637
492.	0.106708	244.81	10.5	10.4	-13.96	-13.95	-2.61	-2.62	320.2	-0.011756
494.	0.107124	245.75	8.8	8.8	-13.83	-13.82	-2.62	-2.61	323.4	-0.011875
496.	0.107540	246.69	7.1	7.2	-13.69	-13.68	-2.62	-2.62	326.7	-0.011999
498.	0.107954	247.62	5.6	5.5	-13.53	-13.55	-2.62	-2.64	329.9	-0.012117
500.	0.108368	248.56	3.8	3.7	-13.41	-13.41	-2.66	-2.65	333.2	-0.012234
502.	0.108782	249.49	1.7	1.7	-13.25	-13.27	-2.67	-2.66	336.3	-0.012349
504.	0.109196	250.43	-0.6	-0.4	-13.12	-13.13	-2.66	-2.66	339.3	-0.012461
506.	0.109610	251.36	-2.7	-2.7	-12.99	-12.99	-2.66	-2.67	342.1	-0.012566
508.	0.110026	252.30	-4.6	-5.0	-12.84	-12.85	-2.66	-2.67	345.2	-0.012677
510.	0.110442	253.23	-7.5	-7.1	-12.69	-12.70	-2.71	-2.69	348.3	-0.012793
512.	0.110858	254.17	-9.0	-8.9	-12.55	-12.56	-2.69	-2.70	351.4	-0.012909
514.	0.111274	255.11	-10.3	-10.3	-12.40	-12.41	-2.70	-2.71	354.6	-0.013026
516.	0.111690	256.05	-11.3	-11.5	-12.27	-12.26	-2.71	-2.71	357.8	-0.013144
518.	0.112104	256.98	-12.7	-12.8	-12.10	-12.11	-2.74	-2.73	361.2	-0.013272
520.	0.112518	257.91	-14.0	-13.9	-11.96	-11.96	-2.75	-2.75	364.7	-0.013401
522.	0.112931	258.84	-14.9	-14.5	-11.80	-11.81	-2.77	-2.77	368.4	-0.013535
524.	0.113344	259.77	-14.4	-14.8	-11.67	-11.66	-2.79	-2.78	371.8	-0.013662
526.	0.113757	260.70	-14.6	-14.7	-11.51	-11.50	-2.78	-2.80	375.2	-0.013788
528.	0.114170	261.63	-14.5	-14.0	-11.35	-11.35	-2.82	-2.81	378.5	-0.013912
530.	0.114583	262.56	-13.1	-13.2	-11.19	-11.19	-2.84	-2.84	381.9	-0.014036

Frame No.	Smooth t (sec)	X (ft)	Raw α (deg)	Smooth α (deg)	Raw x (in.)	Smooth x (in.)	Raw y (in.)	Smooth y (in.)	V_m (in./sec)	$\ln\left(1+\frac{V_m}{V_w}\right)$
532.	0.114997	263.50	-11.8	-12.0	-11.03	-11.03	-2.86	-2.87	385.1	-0.014154
534.	0.115409	264.42	-10.9	-10.9	-10.89	-10.87	-2.90	-2.89	388.2	-0.014270
536.	0.115820	265.35	-9.7	-9.7	-10.74	-10.71	-2.92	-2.92	391.4	-0.014386
538.	0.116230	266.27	-8.6	-8.2	-10.58	-10.55	-2.95	-2.96	394.4	-0.014500
540.	0.116639	267.19	-6.1	-6.2	-10.39	-10.39	-2.99	-2.98	397.5	-0.014613
542.	0.117049	268.11	-3.8	-3.9	-10.21	-10.22	-3.02	-3.01	400.5	-0.014726
544.	0.117460	269.04	-1.5	-1.7	-10.05	-10.06	-3.00	-3.02	403.6	-0.014841
546.	0.117873	269.97	0.3	0.5	-9.89	-9.89	-3.06	-3.04	406.9	-0.014960
548.	0.1182[illegible]	270.90	2.5	2.5	-9.72	-9.72	-3.05	-3.06	410.0	-0.015075
550.	0.11[illegible]	271.83	4.8	4.7	-9.52	-9.55	-3.09	-3.09	413.0	-0.015188
552.	0.119114	272.76	6.4	6.6	-9.36	-9.38	-3.11	-3.11	416.2	-0.015308
554.	0.119527	273.59	8.5	8.3	-9.17	-9.21	-3.15	-3.16	419.5	-0.015430
556.	0.119940	274.62	9.6	9.8	-9.02	-9.03	-3.20	-3.19	422.9	-0.015554
558.	0.120352	275.54	11.1	11.3	-8.86	-8.86	-3.24	-3.23	426.2	-0.015676
560.	0.120764	276.47	12.8	12.5	-8.67	-8.68	-3.23	-3.25	429.4	-0.015796
562.	0.121176	277.39	13.5	13.4	-8.50	-8.50	-3.27	-3.26	432.4	-0.015908
564.	0.121589	278.32	13.5	13.8	-8.34	-8.32	-3.28	-3.28	435.5	-0.016022
566.	0.122001	279.25	13.9	13.8	-8.14	-8.14	-3.32	-3.32	438.4	-0.016130
568.	0.122413	280.17	13.7	13.6	-7.98	-7.96	-3.35	-3.36	441.0	-0.016226
570.	0.122825	281.10	12.9	13.2	-7.76	-7.78	-3.40	-3.39	443.6	-0.016321
572.	0.123236	282.02	12.3	12.4	-7.60	-7.60	-3.41	-3.40	446.2	-0.016419
574.	0.123646	282.94	11.4	11.3	-7.43	-7.41	-3.39	-3.40	448.8	-0.016515
576.	0.124055	283.86	10.1	10.1	-7.23	-7.23	-3.41	-3.40	451.5	-0.016616
578.	0.124464	284.78	8.5	8.6	-7.05	-7.04	-3.40	-3.41	454.5	-0.016727
580.	0.124872	285.70	7.0	7.1	-6.87	-6.86	-3.45	-3.44	457.5	-0.016837
582.	0.125281	286.61	5.6	5.4	-6.65	-6.67	-3.45	-3.45	460.6	-0.016954
584.	0.125691	287.53	3.6	3.6	-6.49	-6.48	-3.49	-3.48	463.6	-0.017066
586.	0.126103	288.46	1.5	1.8	-6.24	-6.28	-3.46	-3.48	466.9	-0.017187
588.	0.126515	289.38	0.	-0.4	-6.08	-6.09	-3.50	-3.49	470.1	-0.017306
590.	0.126927	290.31	-2.4	-2.3	-5.88	-5.90	-3.48	-3.49	472.8	-0.017406
592.	0.127338	291.23	-4.6	-4.3	-5.68	-5.70	-3.50	-3.49	475.4	-0.017523
594.	0.127748	292.15	-5.8	-6.1	-5.49	-5.51	-3.47	-3.47	479.0	-0.017636
596.	0.128159	293.07	-7.8	-7.6	-5.28	-5.31	-3.46	-3.47	482.4	-0.017763
598.	0.128569	293.99	-9.1	-9.0	-5.10	-5.11	-3.47	-3.49	485.5	-0.017877
600.	0.128978	294.91	-10.2	-10.5	-4.90	-4.91	-3.53	-3.52	488.7	-0.017996
602.	0.129389	295.83	-11.8	-11.6	-4.72	-4.71	-3.56	-3.54	491.8	-0.018111
604.	0.129800	296.75	-12.7	-12.7	-4.49	-4.50	-3.56	-3.57	494.9	-0.018227
606.	0.130211	297.67	-13.3	-13.4	-4.29	-4.30	-3.56	-3.57	497.8	-0.018337
608.	0.130622	298.59	-13.9	-13.7	-4.10	-4.09	-3.60	-3.59	500.5	-0.018436
610.	0.131033	299.52	-13.6	-13.9	-3.88	-3.89	-3.60	-3.62	503.2	-0.018536
612.	0.131443	300.43	-13.9	-13.7	-3.71	-3.68	-3.65	-3.64	506.1	-0.018643
614.	0.131852	301.35	-13.3	-13.1	-3.50	-3.47	-3.68	-3.68	509.5	-0.018771
616.	0.132260	302.27	-12.0	-12.2	-3.27	-3.26	-3.69	-3.70	512.9	-0.018896
618.	0.132667	303.18	-10.9	-10.8	-3.05	-3.05	-3.75	-3.72	516.1	-0.019014
620.	0.133075	304.09	-9.2	-9.2	-2.85	-2.84	-3.73	-3.75	519.7	-0.019151
622.	0.133484	305.01	-7.9	-7.9	-2.65	-2.63	-3.79	-3.79	523.3	-0.019282
624.	0.133892	305.92	-6.0	-6.3	-2.42	-2.41	-3.[illegible]	-3.82	526.4	-0.019400
626.	0.134300	306.83	-5.5	-4.8	-2.19	-2.20	-3.85	-3.85	529.9	-0.019528
628.	0.134709	307.75	-2.4	-2.9	-1.95	-1.98	-3.86	-3.87	533.2	-0.019652
630.	0.135118	308.67	-1.1	-1.0	-1.77	-1.76	-3.89	-3.89	536.6	-0.019779
632.	0.135527	309.58	1.1	[illegible]	-1.54	-1.54	-3.92	-3.92	539.9	-0.019899
634.	0.135936	310.50	3.0	3.0	-1.32	-1.32	-3.95	-3.95	543.5	-0.020035
636.	0.136345	311.41	4.7	4.8	-1.12	-1.10	-3.98	-3.98	546.8	-0.020157
638.	0.136755	312.33	6.7	6.4	-0.89	-0.87	-4.01	-4.03	549.9	-0.020274
640.	0.137164	313.24	7.7	8.0	-0.61	-0.64	-4.08	-4.06	553.0	-0.020390
642.	0.137573	314.16	9.4	9.6	-0.42	-0.42	-4.11	-4.08	556.2	-0.020507
644.	0.137981	315.07	11.4	11.2	-0.17	-0.19	-4.07	-4.09	559.3	-0.020623

TABLE VI

Laboratories using Free-Flight Model Testing in Conventional High-Speed Wind Tunnels

Laboratory	*Location*	*Cognizant Person*
AEDC von Kármán Gas Dynamics Facility	Arnold Air Force Station, Tennessee	J.Lukasiewicz
Ballistic Research Laboratories, Supersonic Wind Tunnels Branch	Aberdeen Proving Ground, Maryland	C.C.Bush
General Dynamics/Convair, High Speed Wind Tunnel	San Diego, California	D.P.Cumming
Jet Propulsion Laboratory, Aerodynamic Facilities	Pasadena, California	E.A.Laumann
NASA Ames Research Center, Thermo- and Gas-Dynamics Division	Moffett Field, California	V.I.Stevens
National Aeronautical Establishment, Unsteady Aerodynamics Laboratory	Ottawa, Canada	K.Orlik-Rückemann
ONERA High Speed Wind Tunnels	Châtillon-sous-Bagneux (Seine), France	P.Carriere
US Naval Ordnance Laboratories, Applied Aerodynamics Division	Silver Springs, Maryland	S.Hastings

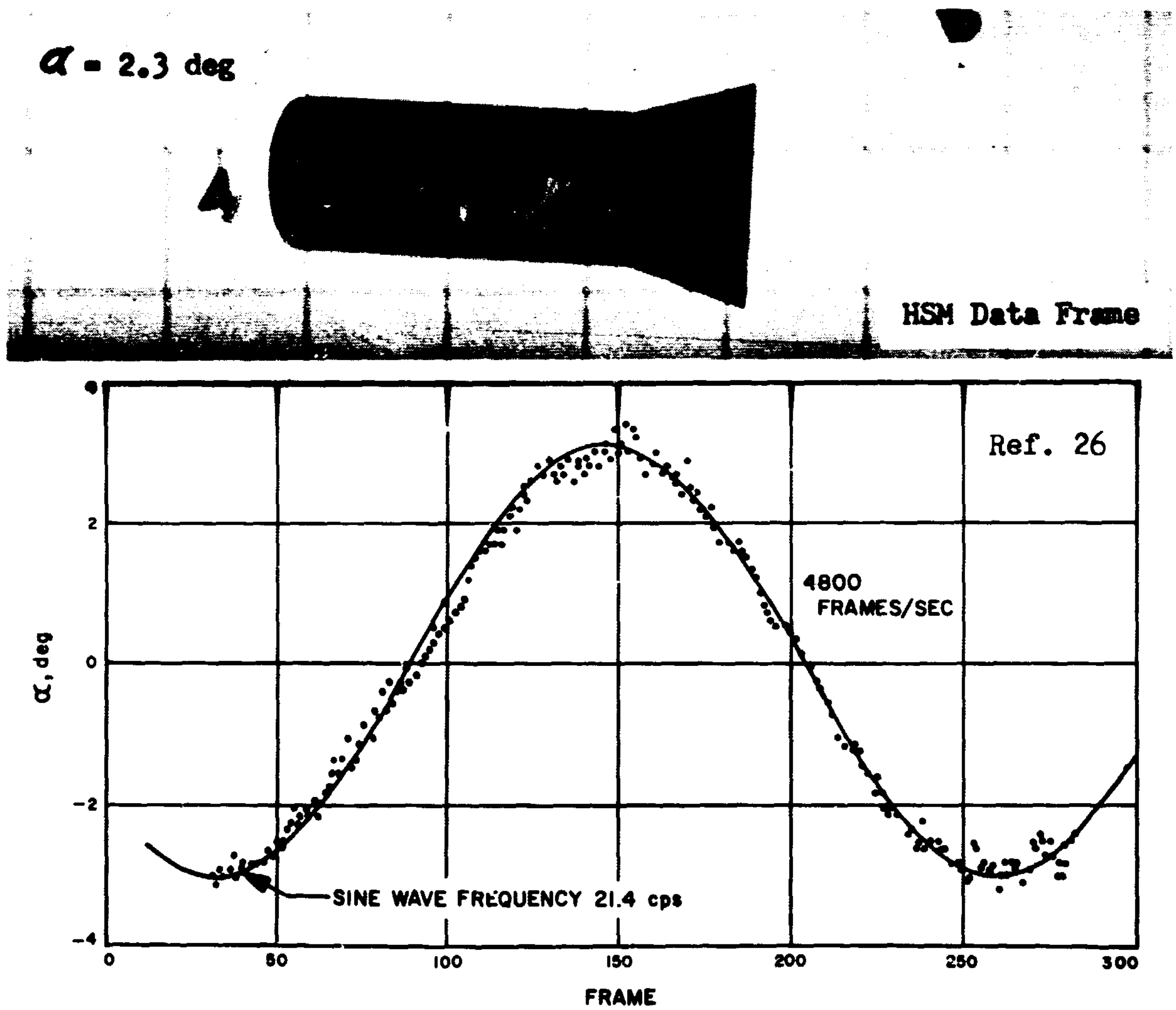

Fig. 1 Detailed angle-of-attack history

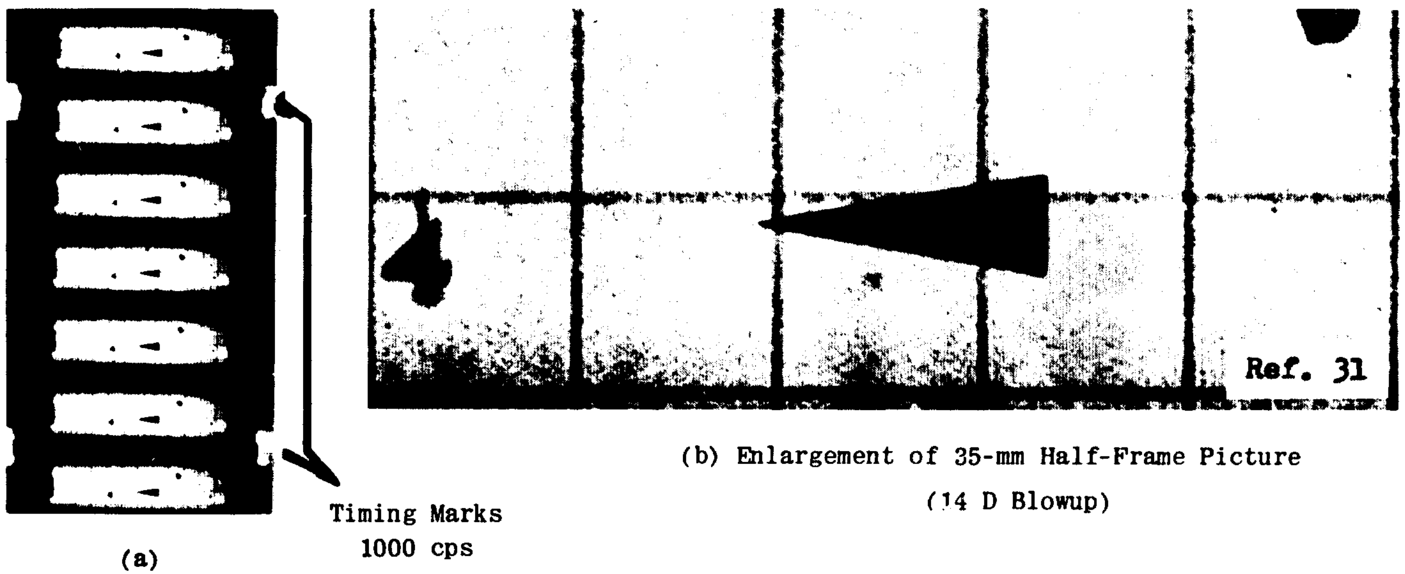

(a)

Half-Frame Pictures
on 35-mm film

(b) Enlargement of 35-mm Half-Frame Picture
(14 D Blowup)

1-in. Grid Spacing
Super Hypan Film (ASA 500) at 4800 Frames/sec
10-in. Focal Length Lens at f5.6
Model Image Size on Film is 0.038-in. Base Diameter

Fig. 2 Example of high-speed movie frame

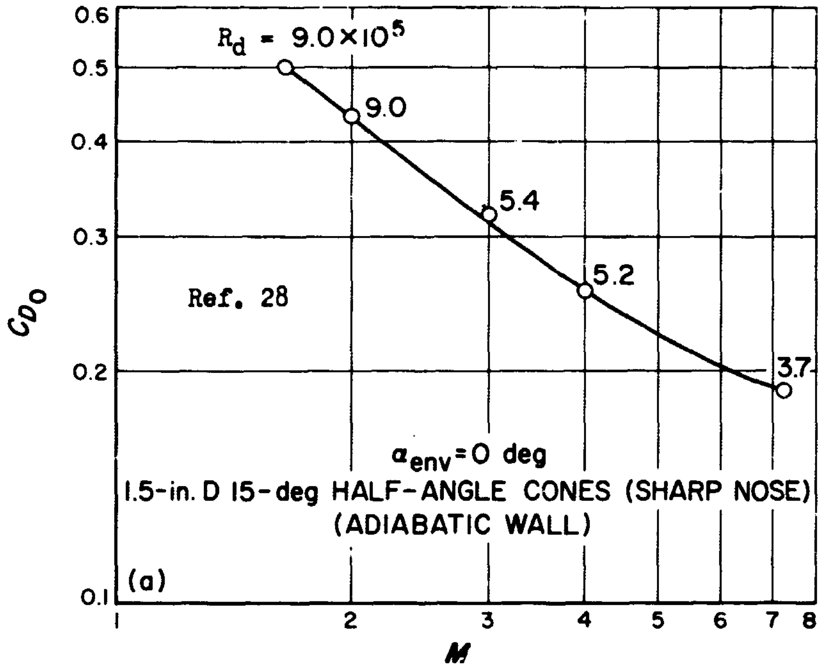

(a) Effect of Mach number

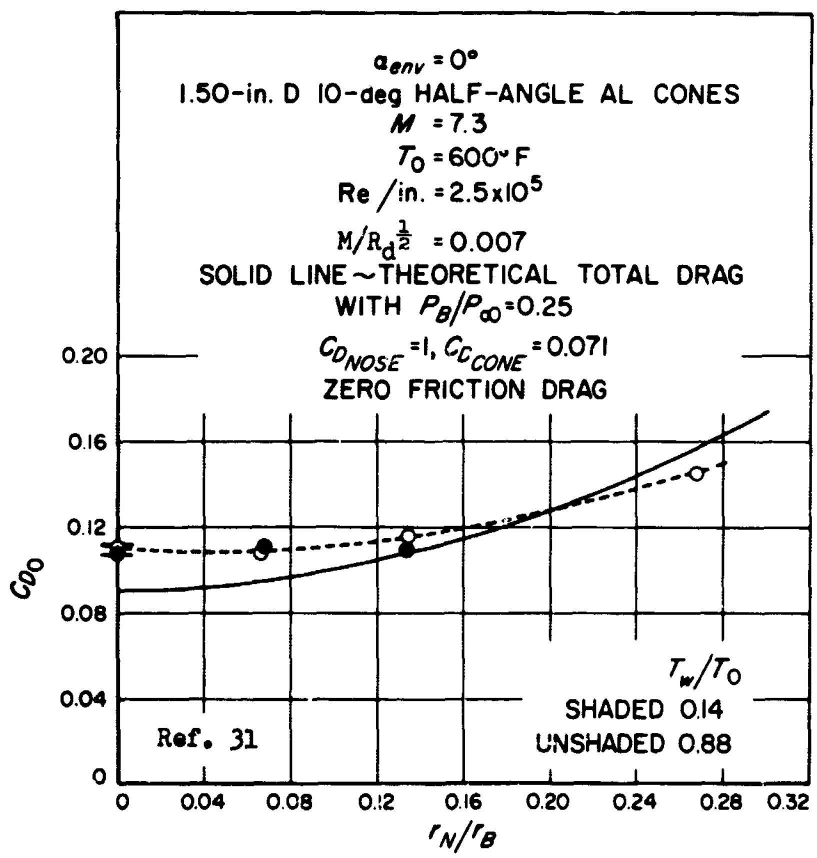

(b) Effect of nose bluntness

Fig. 3 Typical free-flight cone drag studies

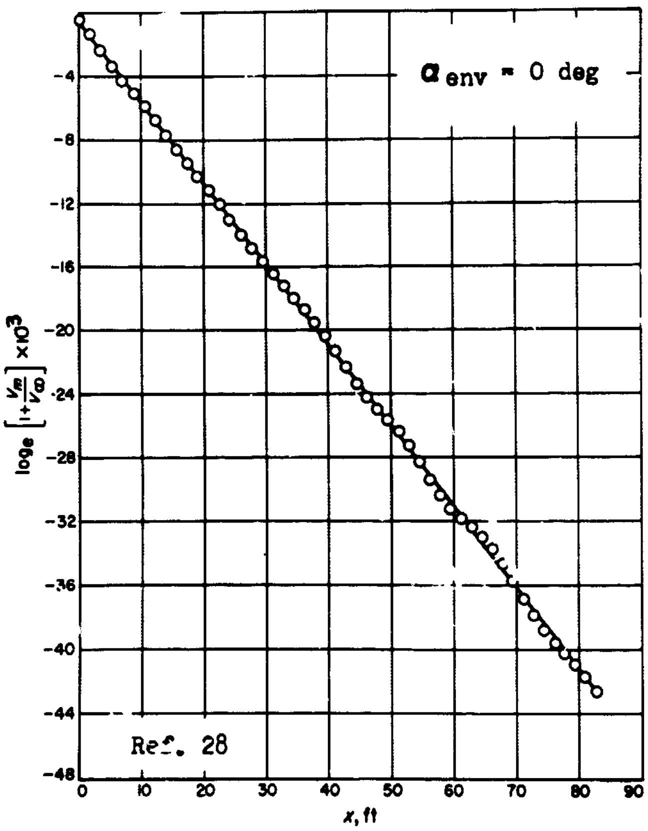

Fig 4   Typical model velocity history (high acceleration)

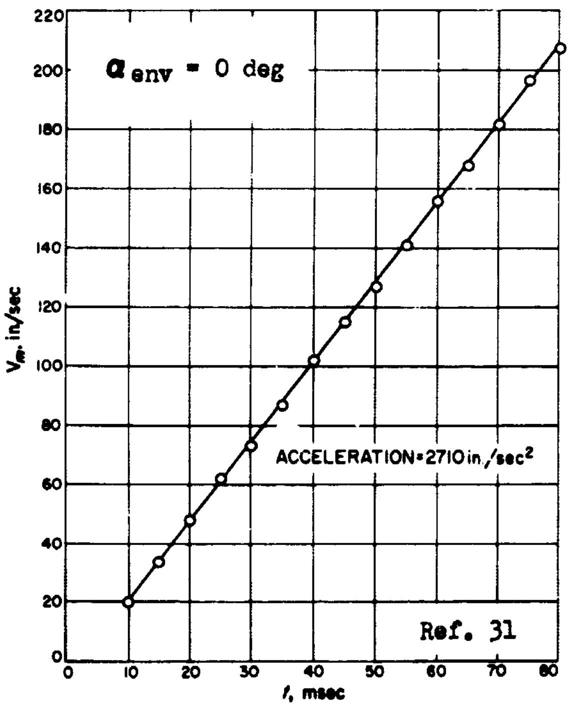

Fig. 5   Typical model velocity history (low acceleration)

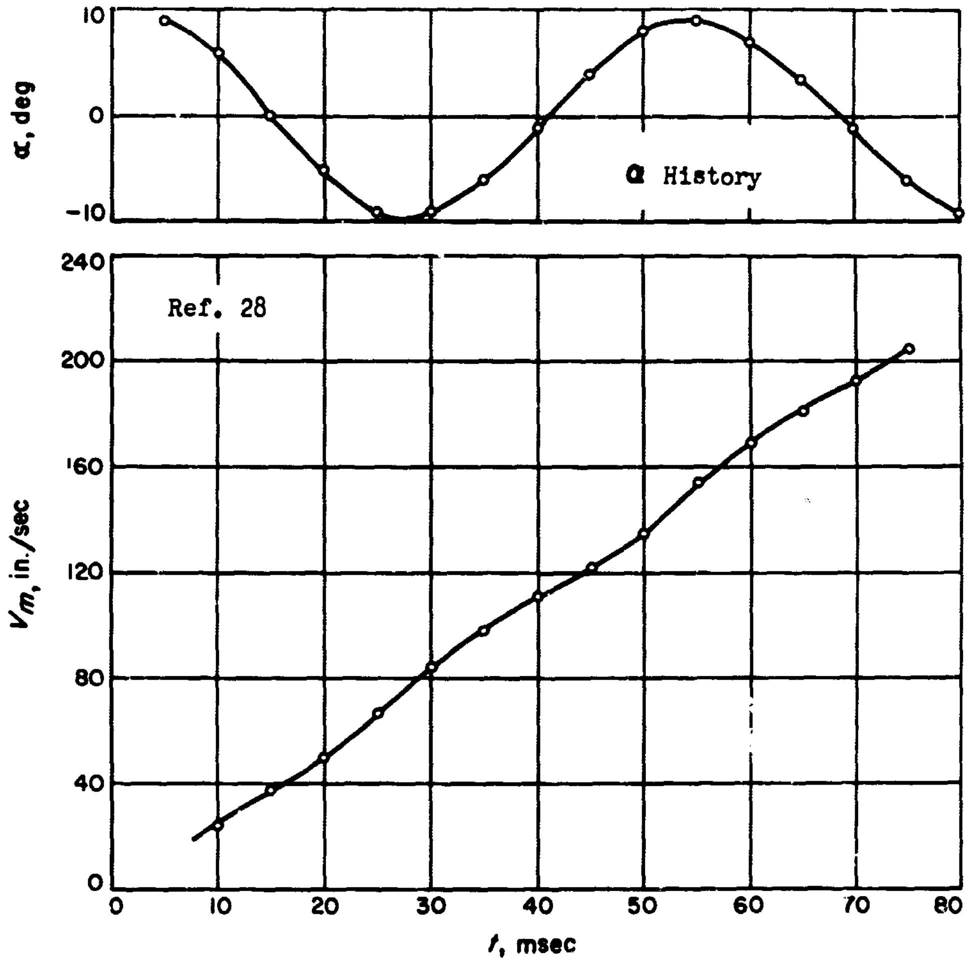

Fig. 6 Typical model velocity history (oscillating slender cone)

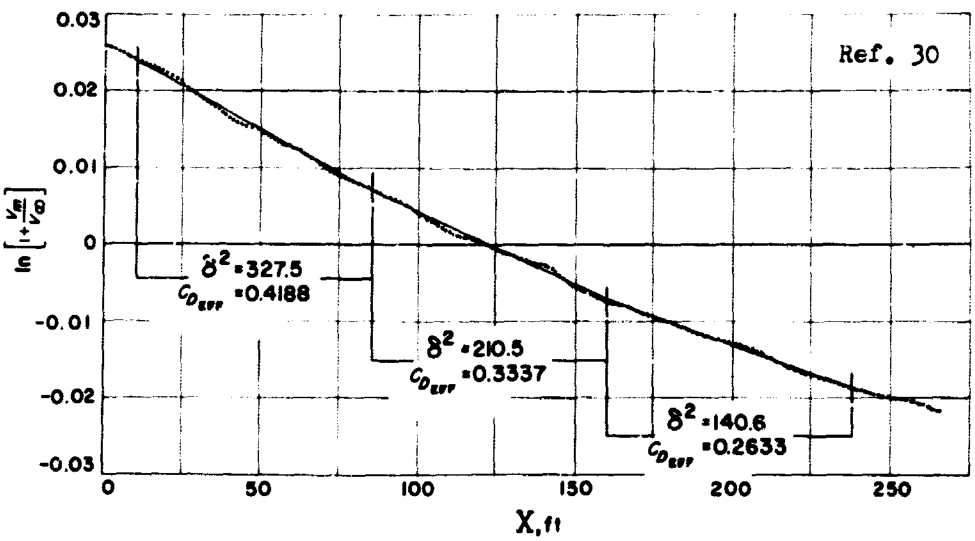

Fig. 7 Typical model velocity history (decaying oscillation amplitude)

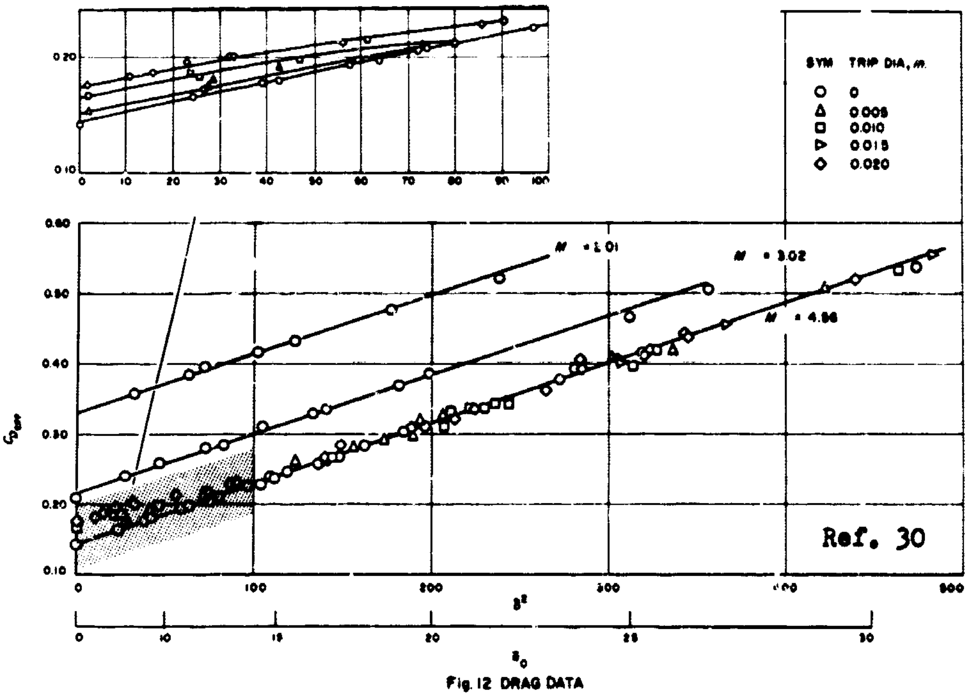

Fig. 8 Effect of oscillation amplitude on cone drag

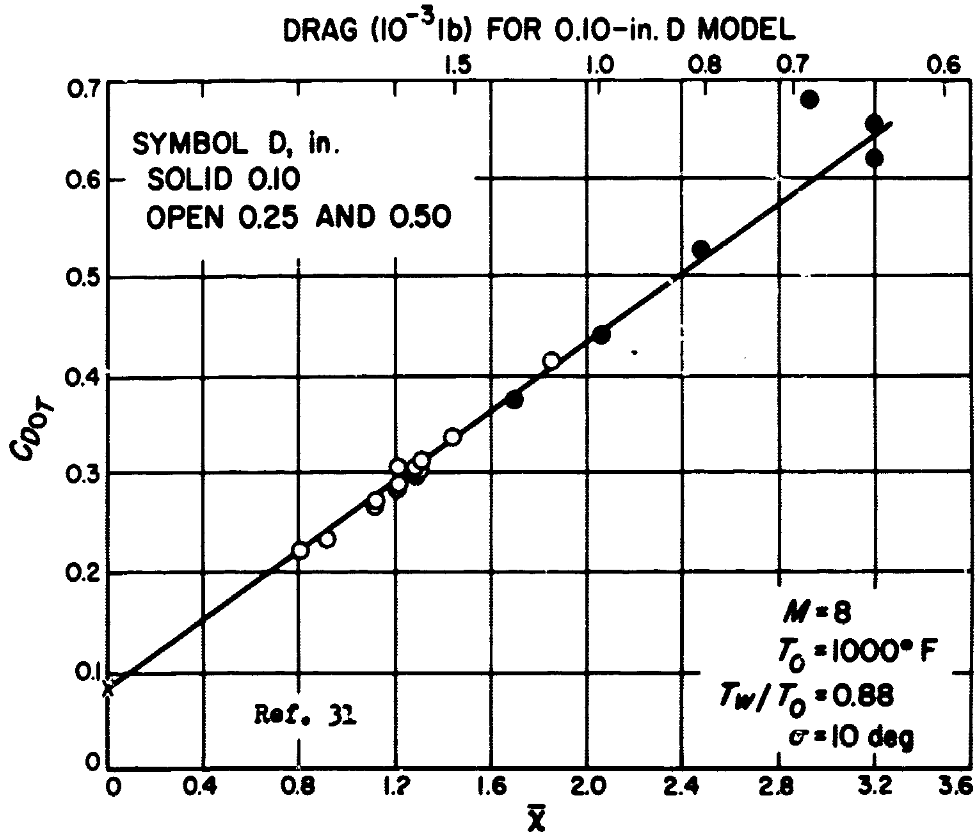

Fig. 9 Effect of hypersonic viscosity parameter on free-flight slender cone zero-lift drag coefficient

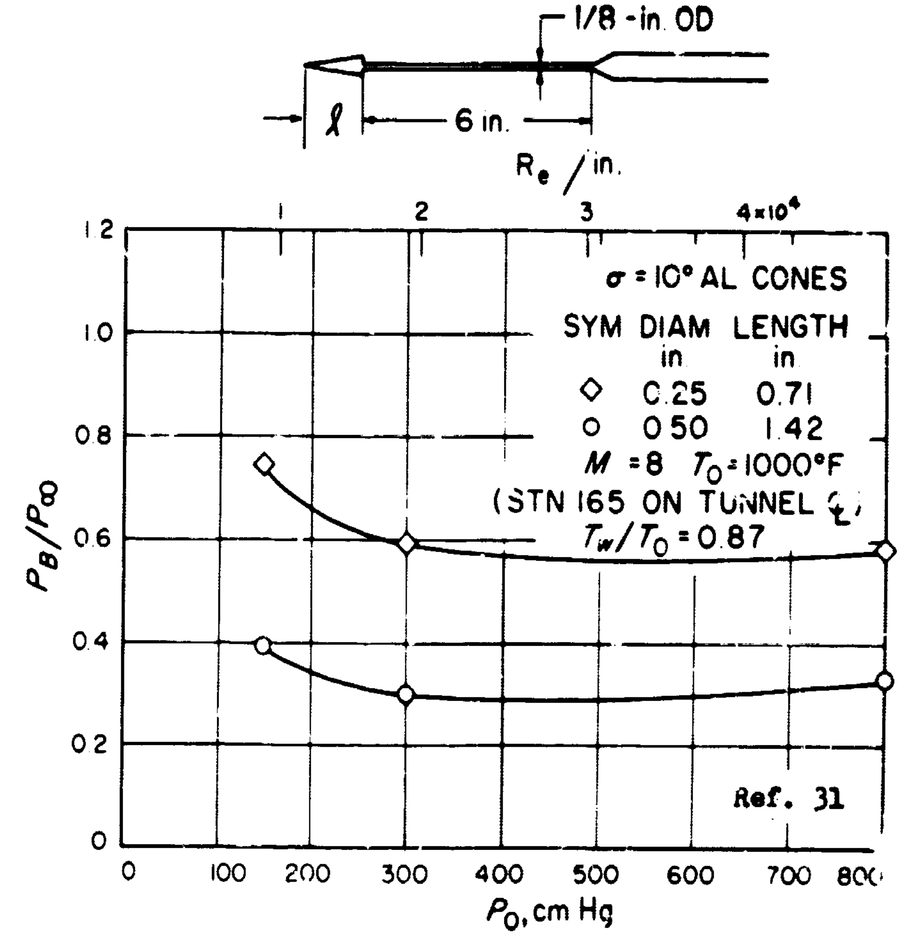

Fig. 10 Effect of sting diameter on model base pressure

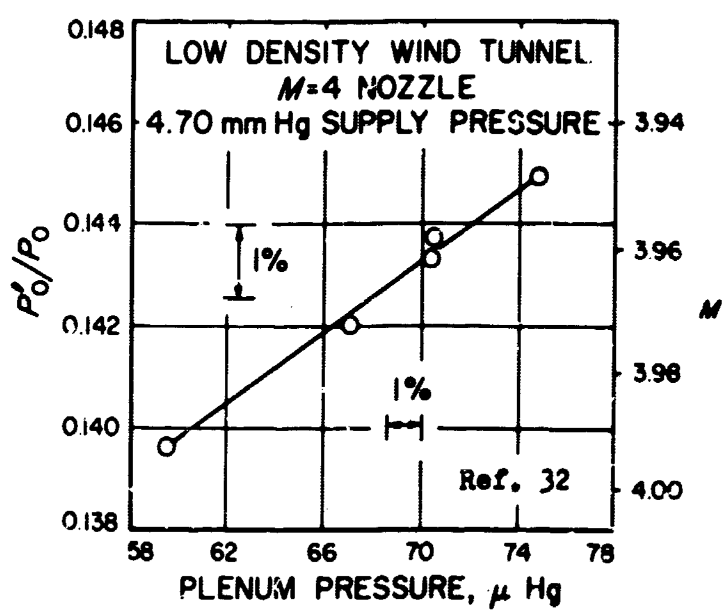

Fig. 11 Effect of plenum pressure on Mach number

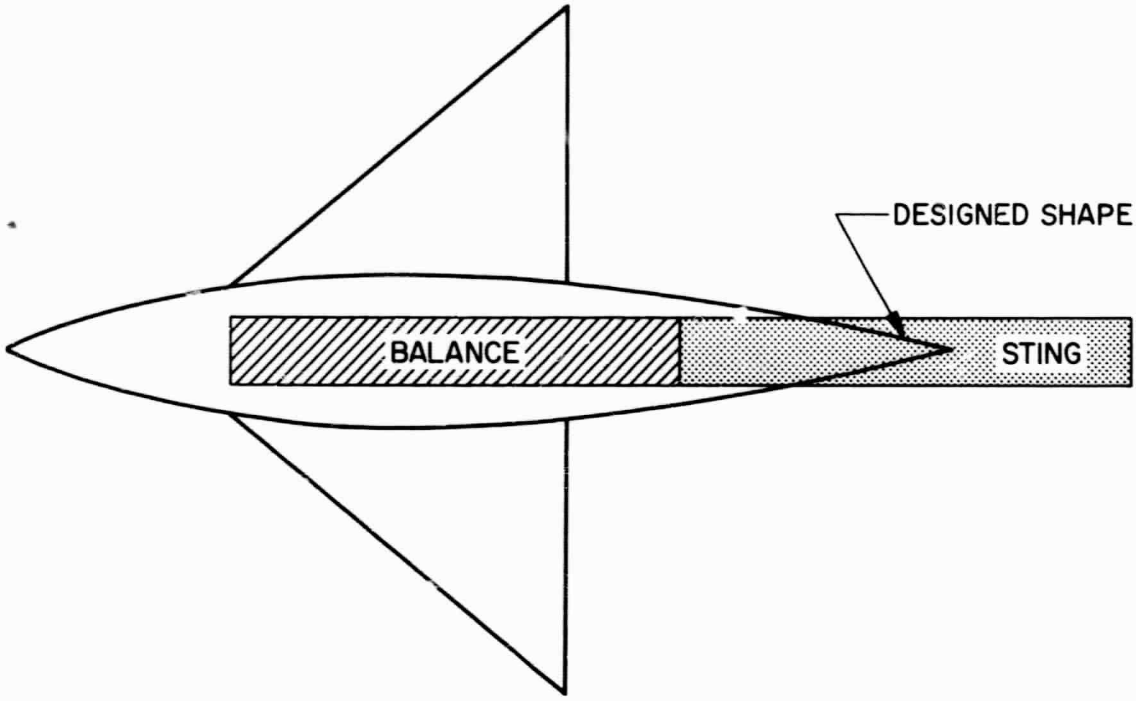

Fig. 12 Example of model aft-portion distortion required to accommodate internal balance and sting

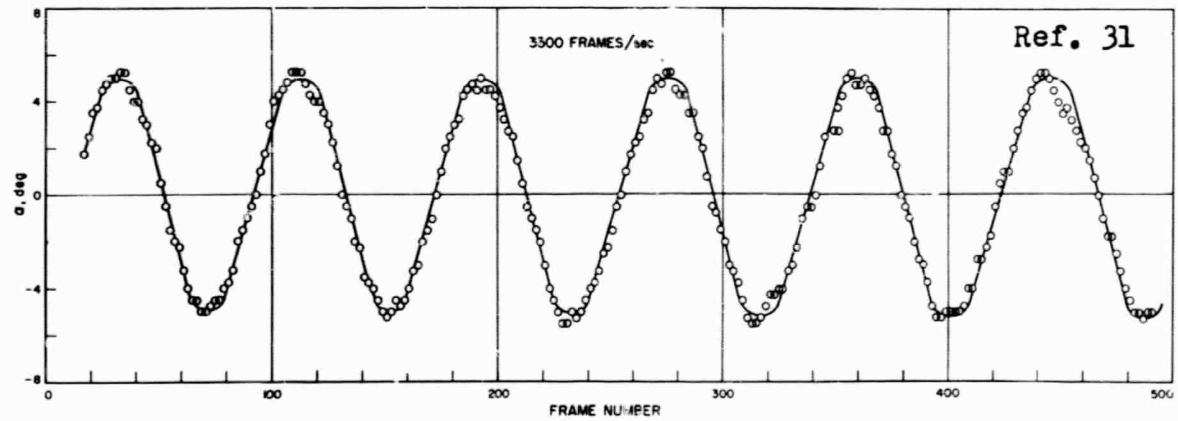

Fig. 13 Typical angle-of-attack history of a gun-launched model (constant oscillation amplitude)

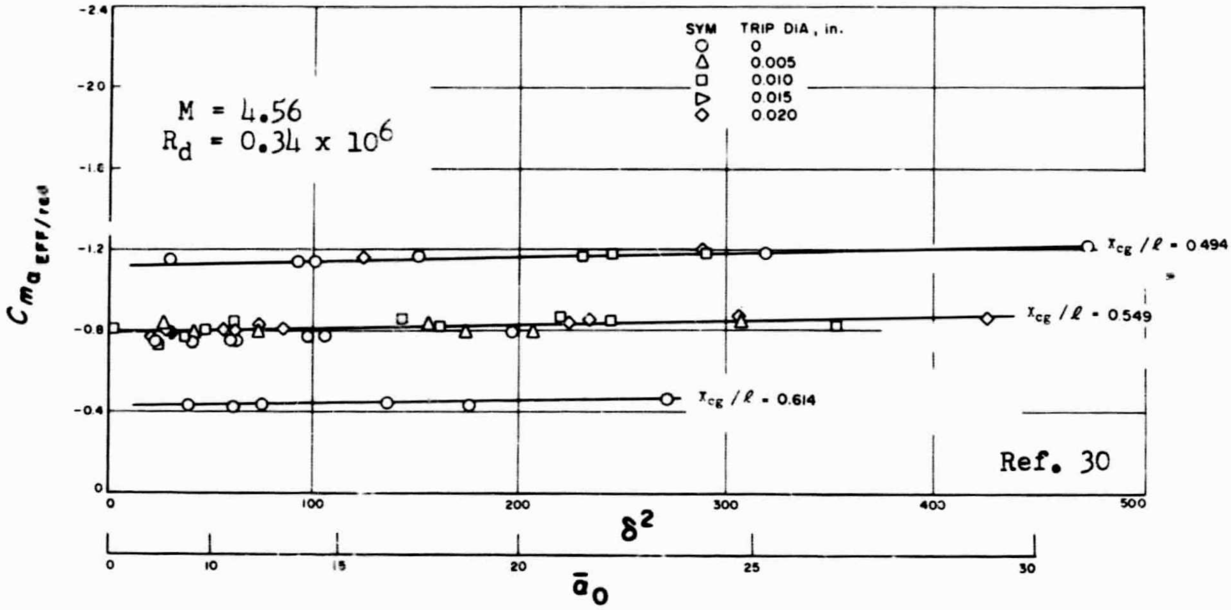

Fig. 14 Effect of oscillation amplitude on pitching moment slope

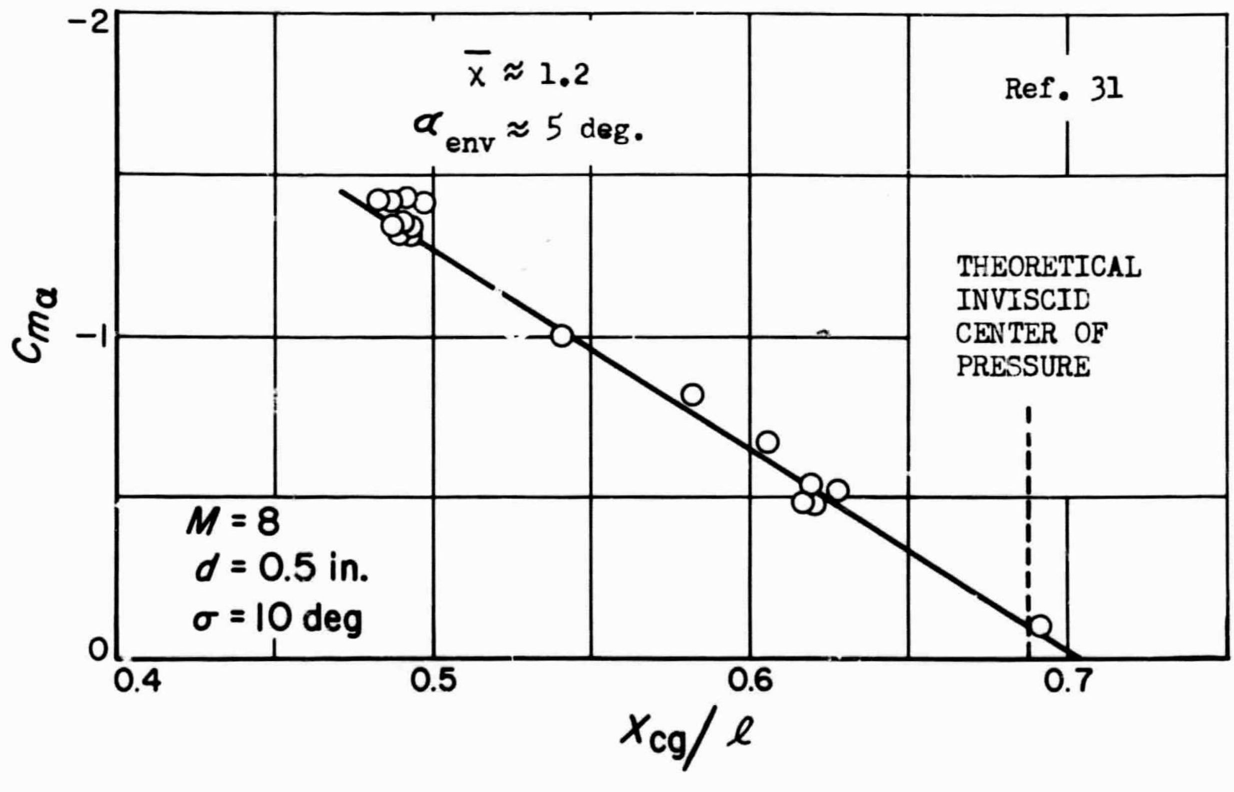

Fig. 15 Effect of cone center-of-gravity location on pitching moment slope

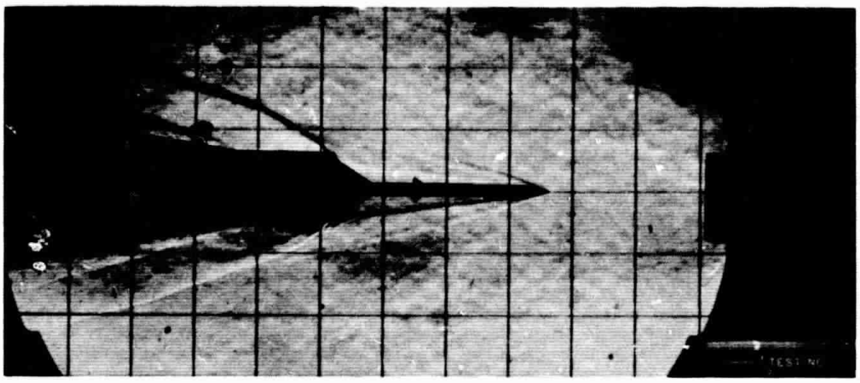

$T_w/T_\infty = 5.4$

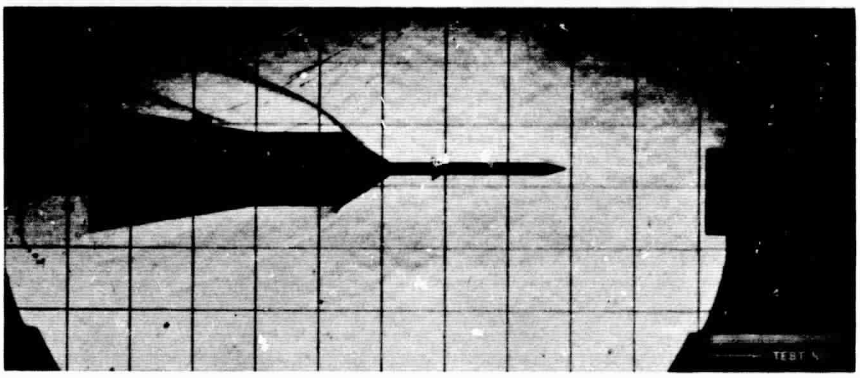

$T_w/T_\infty = 1.1$

$M = 5.1$ $\qquad R_d = 4.7 \times 10^5$

$\alpha = \psi = 0^\circ$ $\qquad$ Altitude Simulation $\approx$ 175,000 ft

SCHLIEREN OF FLOW FIELDS

Fig. 16 Effect of model wall temperature on boundary layer separation

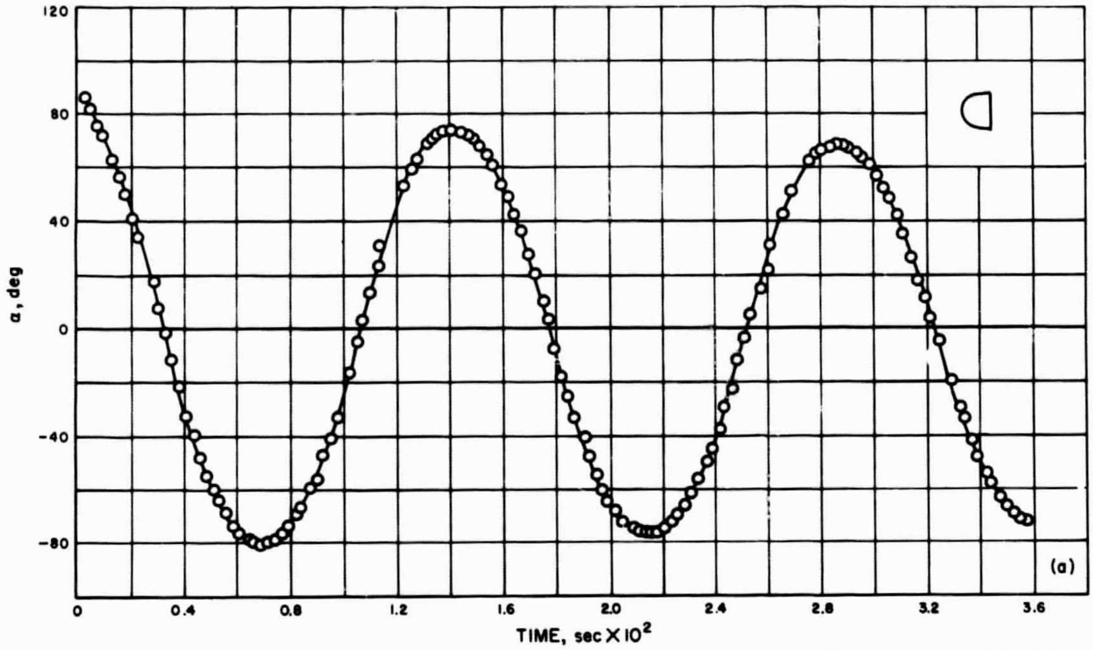

Ref. JPL TR 32-380

(a) High drag shape

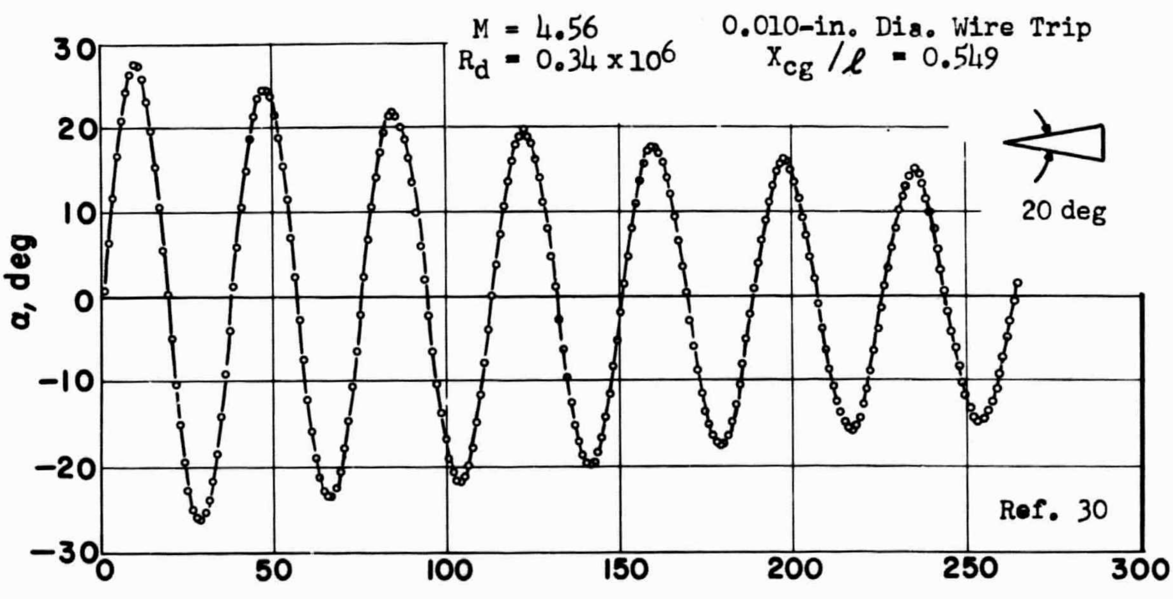

(b) Low drag shape

Fig. 17 Examples of decaying motion for high oscillation amplitudes

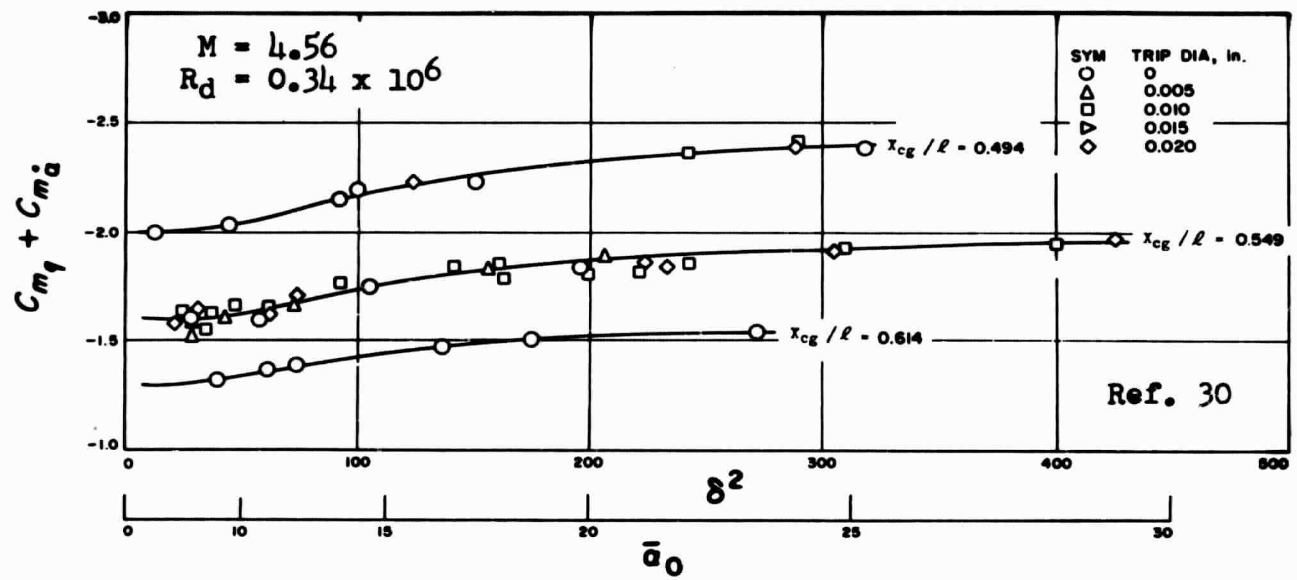

Fig. 18 Effect of oscillation amplitude on cone dynamic stability

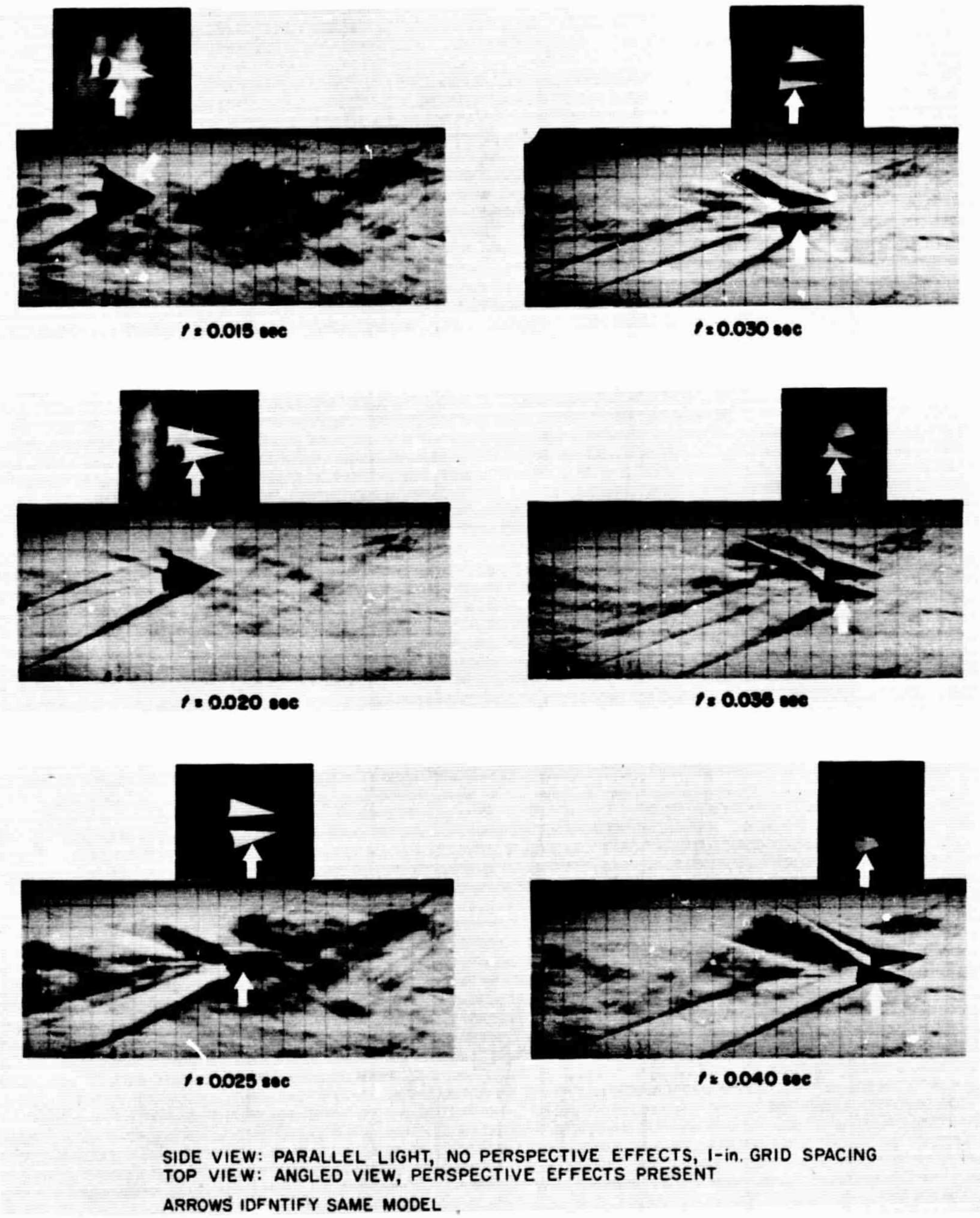

Ref. 28

Fig. 19 Example of a dual-cone salvo gun-launched into a free-flight trajectory

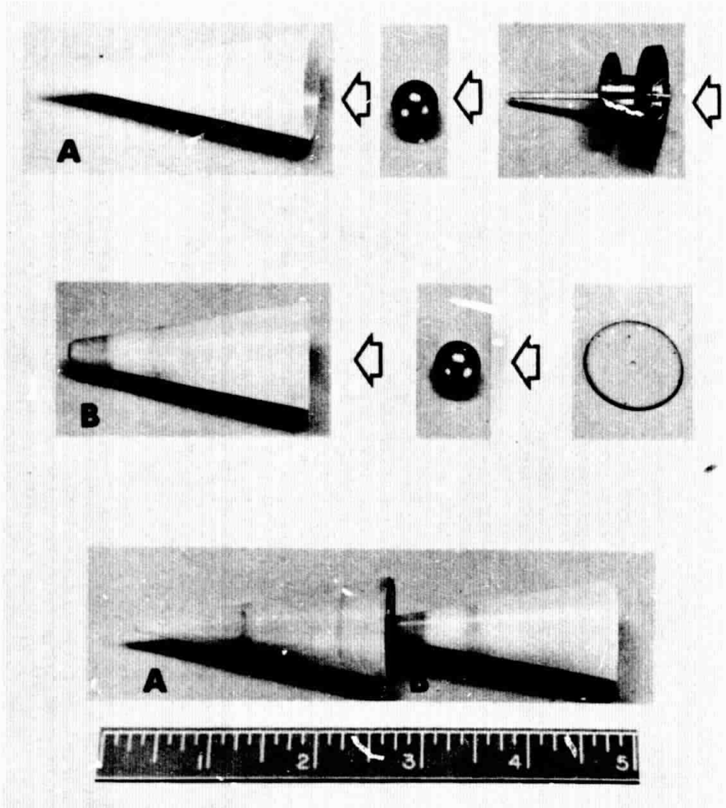

Ref. 35

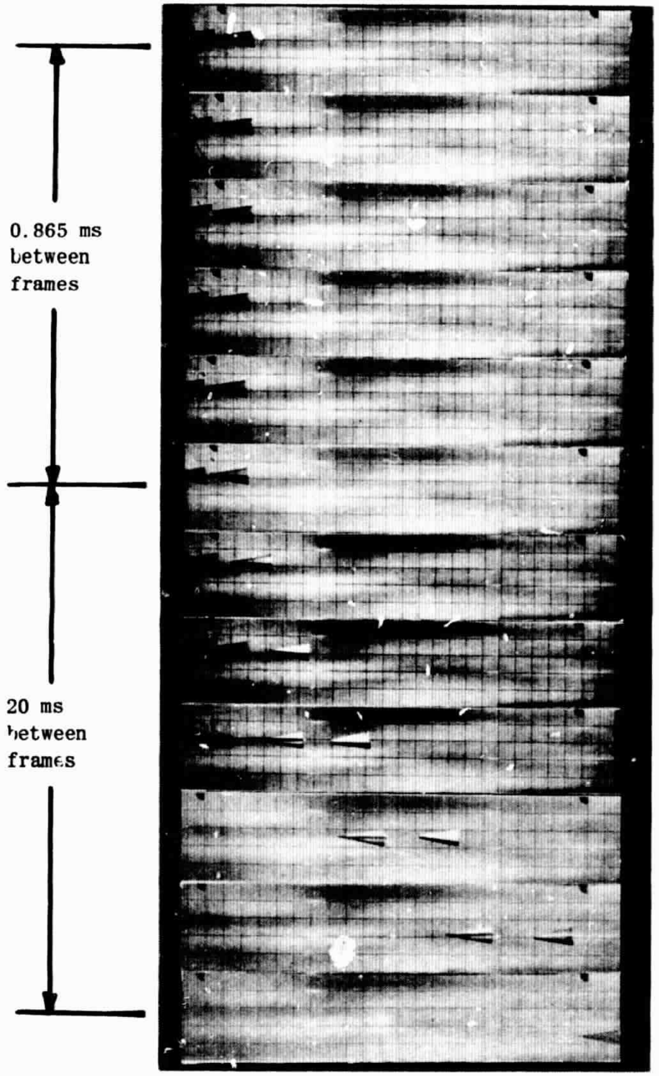

Fig. 20 Example of tandem-body equipment and flight

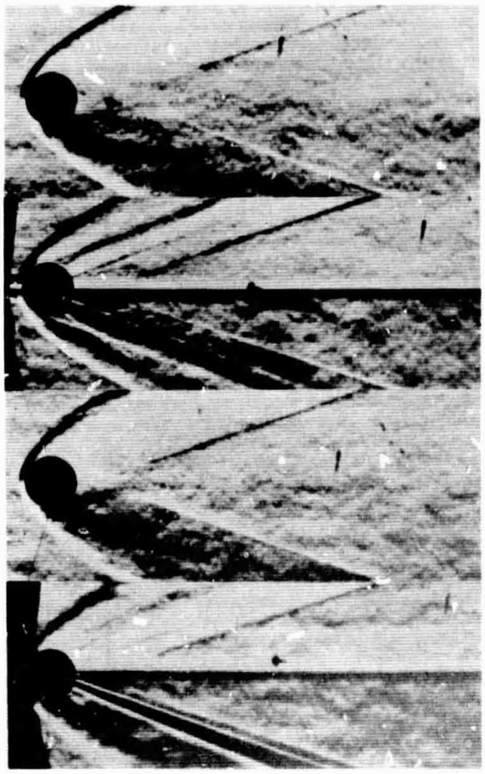

WIRE ORIENTATION	L/d
NO WIRE	1.22
HORIZONTAL	1.00
VERTICAL	0.98
HORIZONTAL AND VERTICAL	——

Ref. 39

M = 3
SUPPLY PRESSURE = 150 cm Hg
R_d = 5.3 x 10^5
MODEL DIAMETER = $1\frac{1}{2}$ in.
WIRE DIAMETER = 0.020 in.

Fig. 21 Effect of support wire orientation on flow pattern about sphere

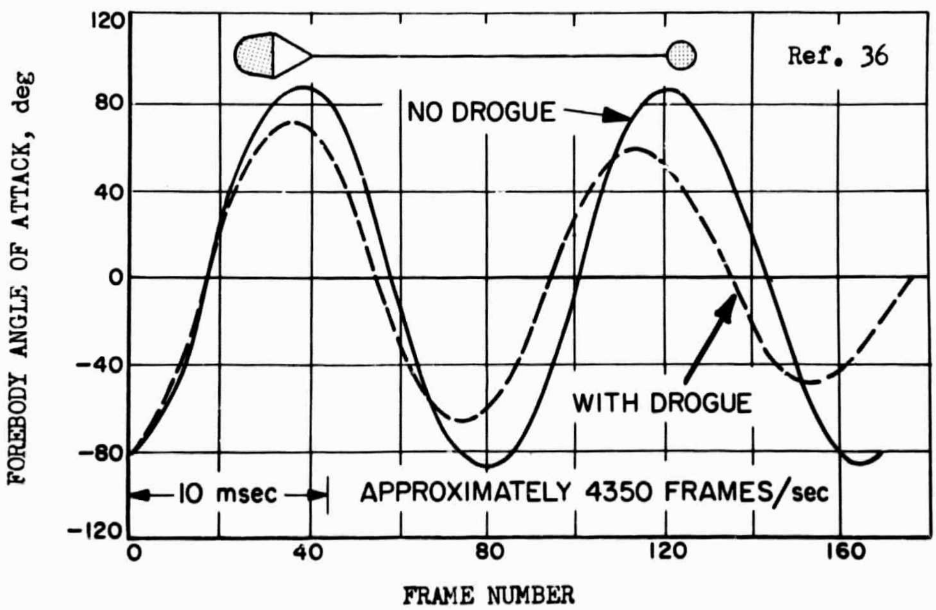

Fig. 22 Effect of a trailing drogue on forebody angle-of-attack history

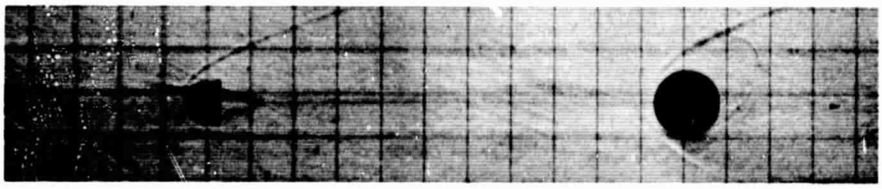

1-in. Grid   HSM Data Frame

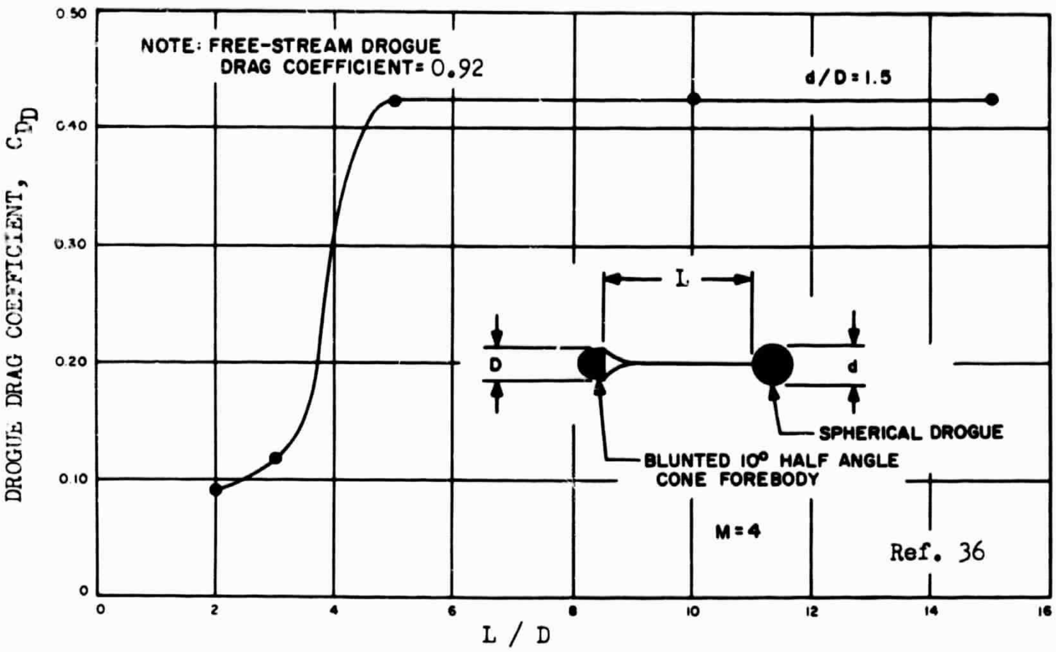

Fig. 23   Effect of tow-line length on drogue drag

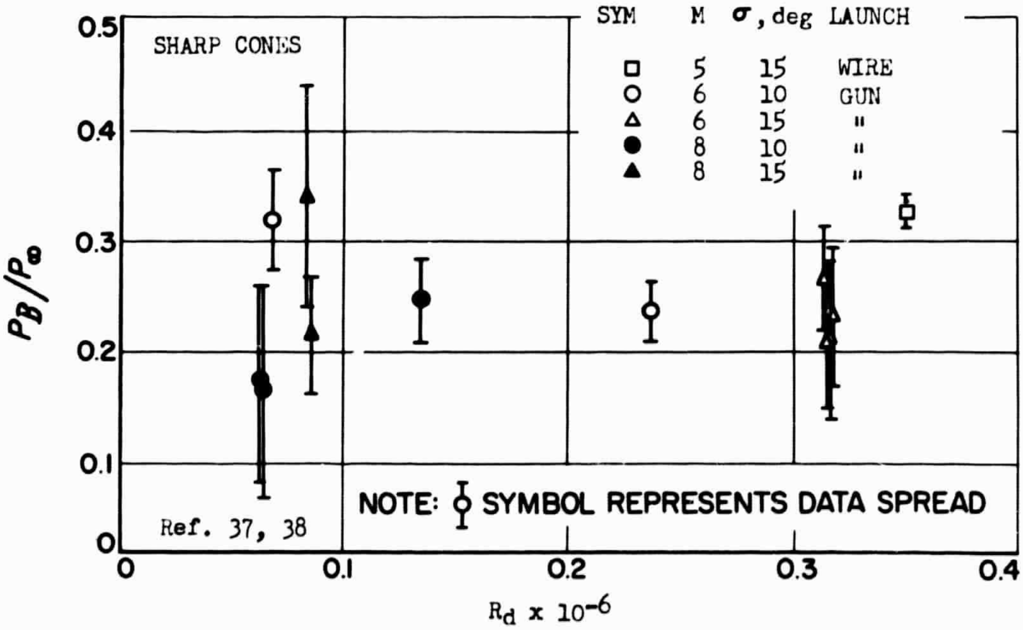

Fig. 24   Free-flight base pressure

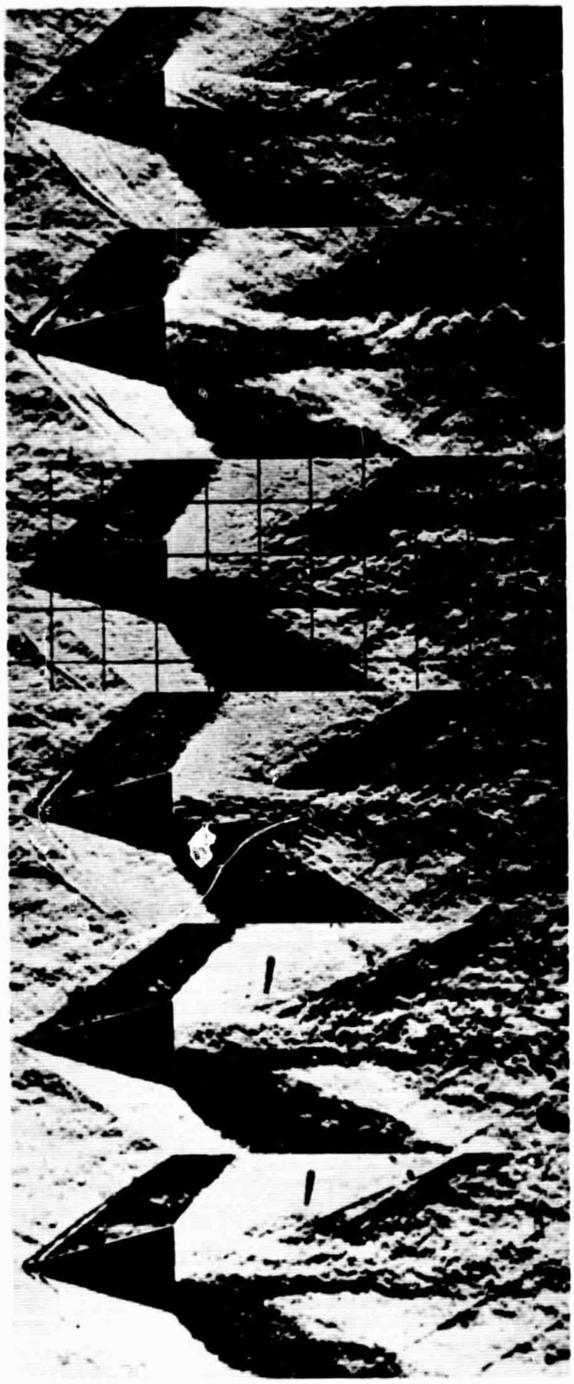

Model Boundary Layer	Mach No.	Supply Pressure (cm Hg)	R_d
Laminar	1.61	60	$4x10^5$
Turbulent	1.61	60	$4x10^5$
Laminar	1.58	120	$8x10^5$
Turbulent	1.58	120	$8x10^5$
Laminar	1.92	140	$8x10^5$
Turbulent	1.93	140	$8x10^5$

30-deg Apex Angle
$1\frac{1}{2}$-in. D Base

Ref. 39

Fig. 25 Effect of Mach number on free-flight cone wakes

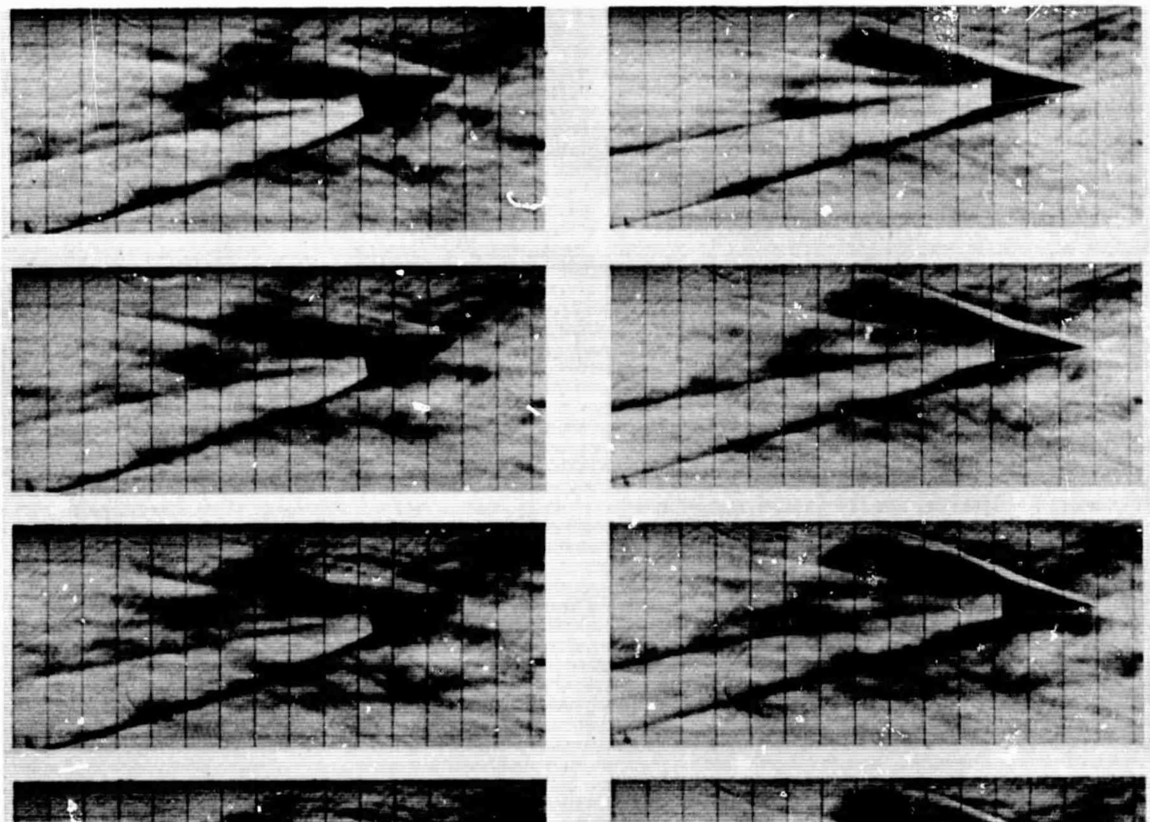

Ref. 30

0.75 msec Between Pictures

1-in. Grid Spacing

Fig. 26 Schlieren wake study of an oscillating cone

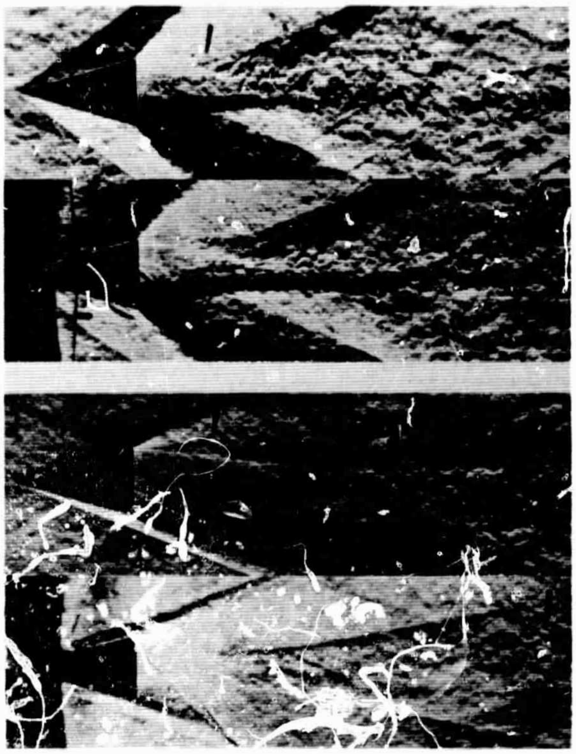

	Mach No.	Supply Pressure (cm Hg)	R_d
Free-Flight	1.92	140	8×10^5
Wire-Supported	2.02	140	8×10^5
Free-Flight	4.64	330	$4\frac{1}{2} \times 10^5$
Wire-Supported	4.77	330	$4\frac{1}{2} \times 10^5$

30-deg Apex Angle
$1\frac{1}{2}$-in. D Base

Ref. 39

Fig. 27 Effect of wire support on cone wake

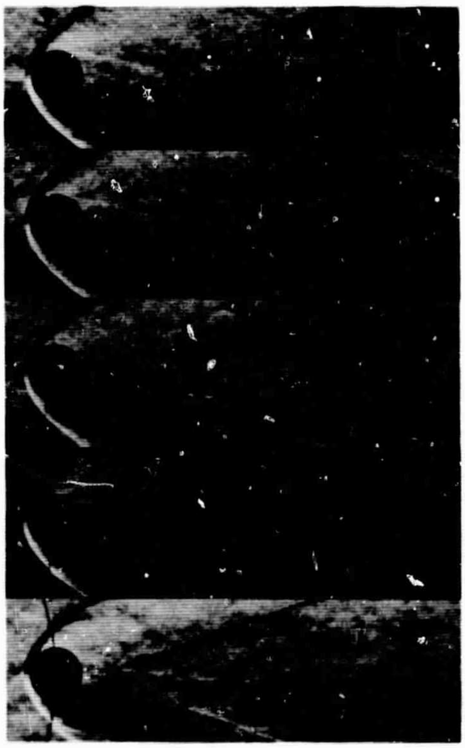

Wire Diam., in.
0
0.005
0.010
0.020
0.040

M = 3

$R_d = 2.3 \times 10^5$

Diameter = $1\frac{1}{2}$ in.

Ref. 39

Fig. 28 Effect of diameter of vertical wire support on optical sphere wakes

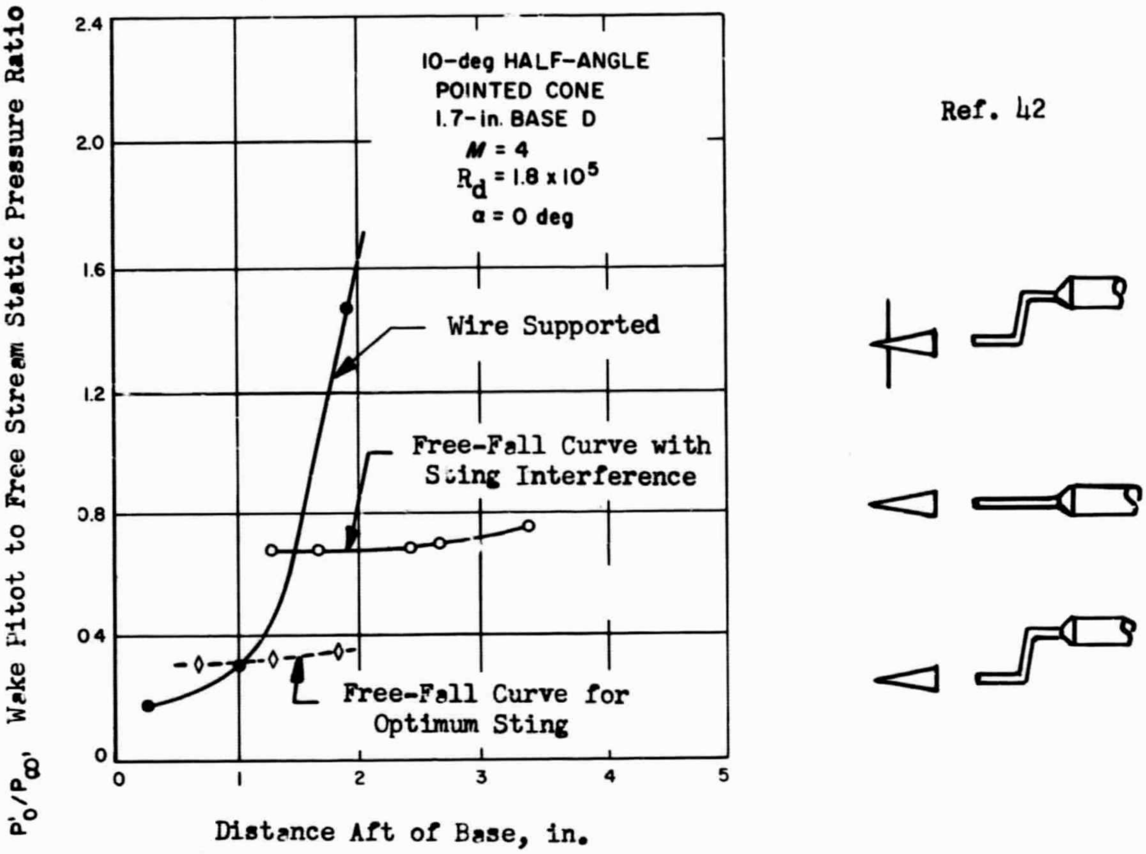

Fig. 29 Centerline pitot-pressure survey through wake of free-fall cone

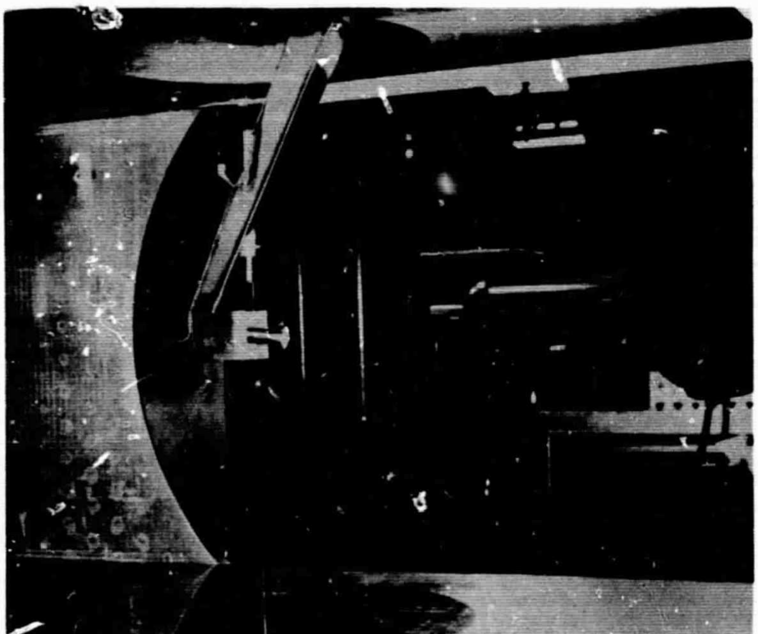

Ref. 35

Fig. 30 Wire-launch installation of model for free-flight test in hypersonic wind tunnel with cooling shield down

Every other
frame shown

Every 20th frame shown
1-in. Grid Spacing
3600 Frames / in.

Ref. 31

Fig. 31 High speed movie sequence of wire release and complete model trajectory

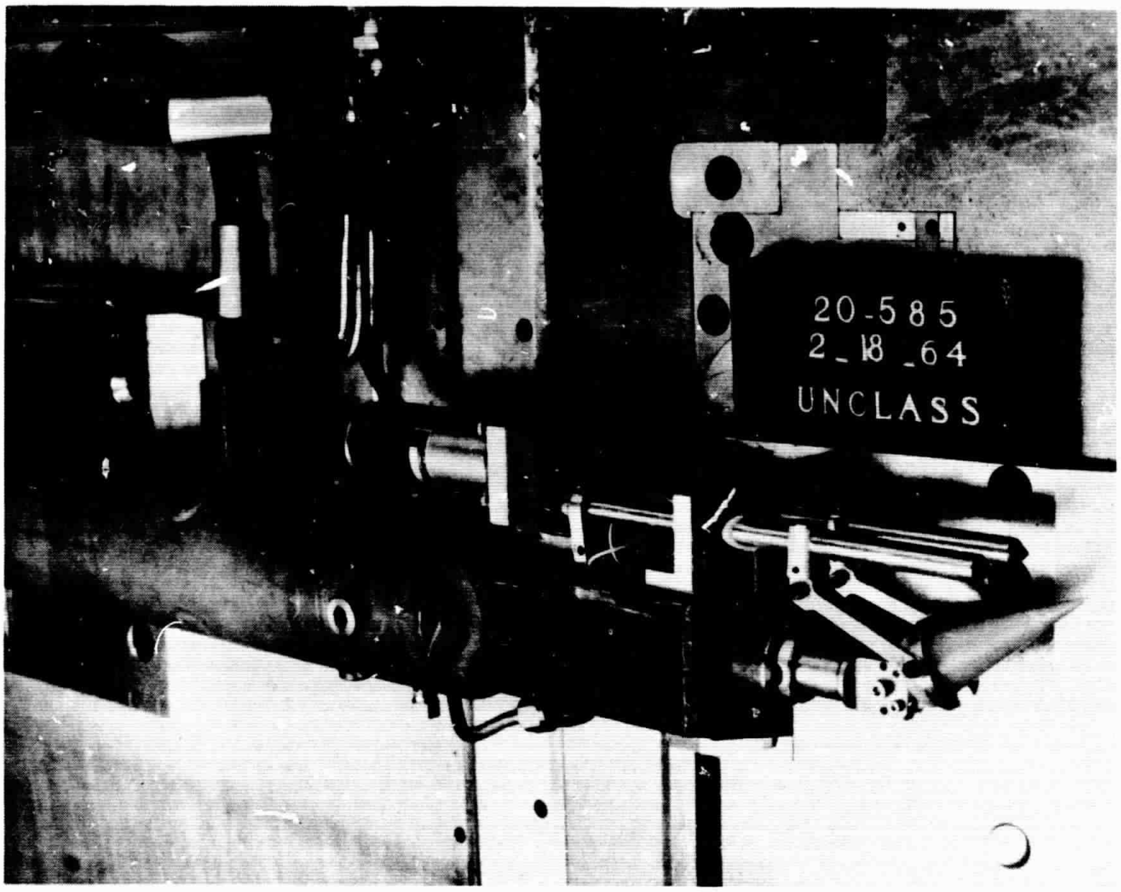

Ref. 45

Fig. 32 Pneumatic launch gun for externally mounted models

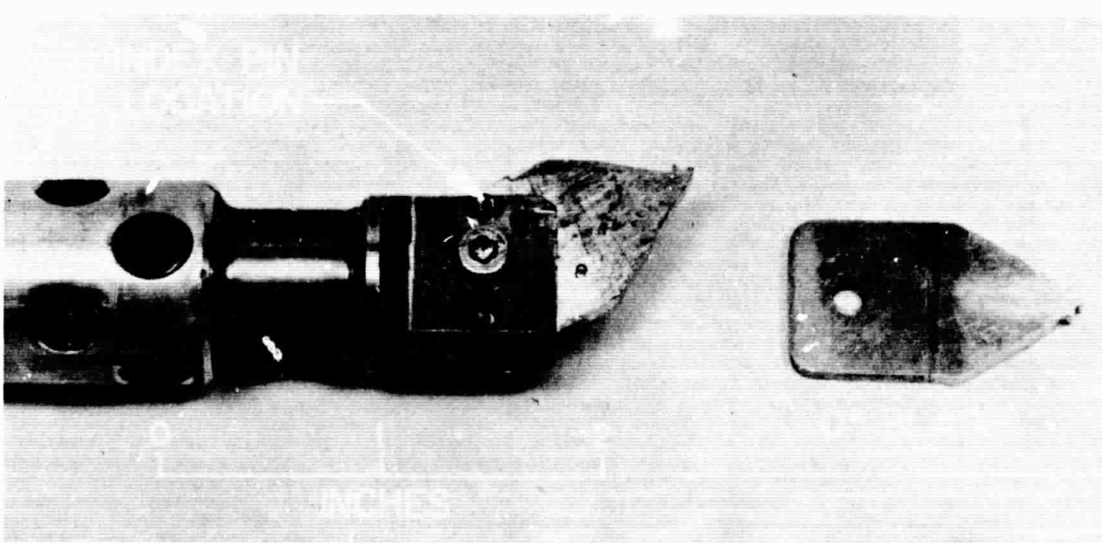

Ref. 45

Fig. 33 Triangular-shaped blade support for cone models

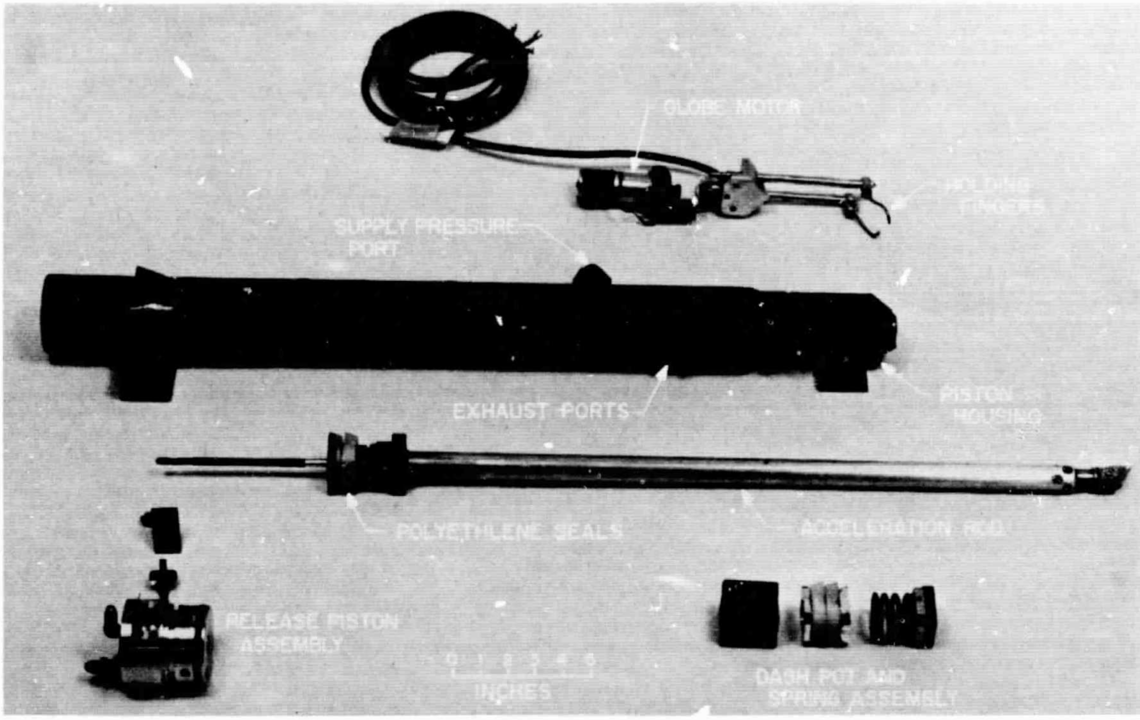

Ref. 45

Fig. 34 Components of pneumatic launcher

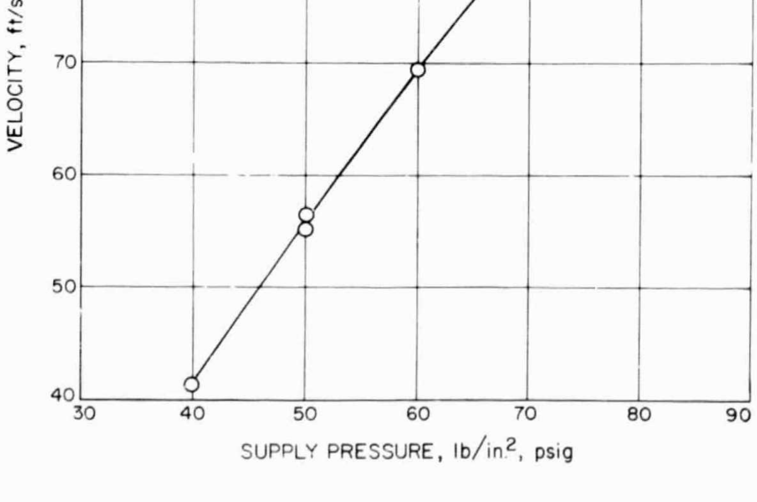

Ref. 45

Fig. 35 Typical example velocity versus chamber pressure for pneumatic model launcher

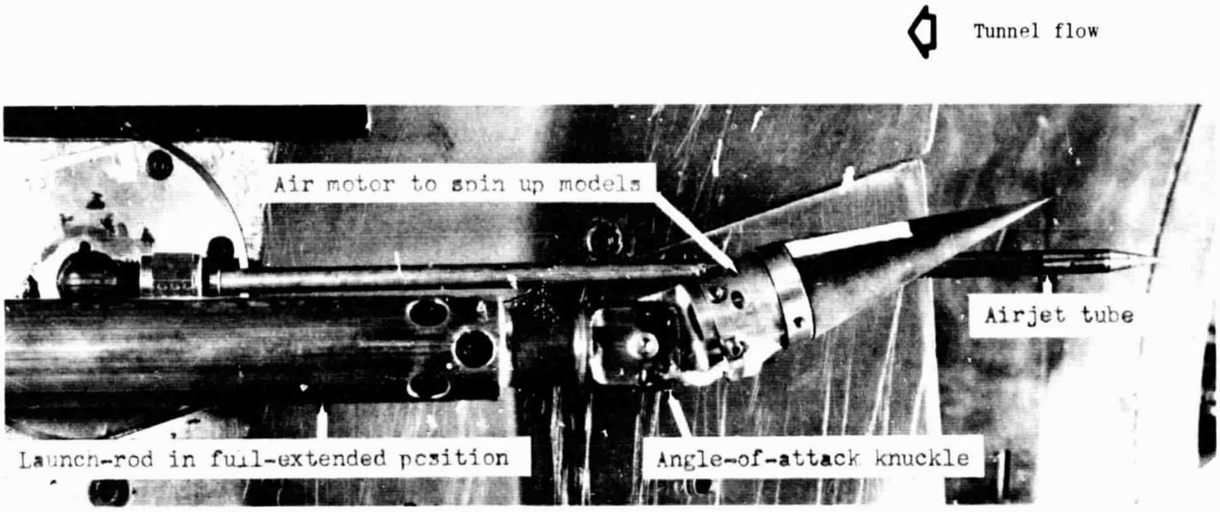

(a) Test section installation

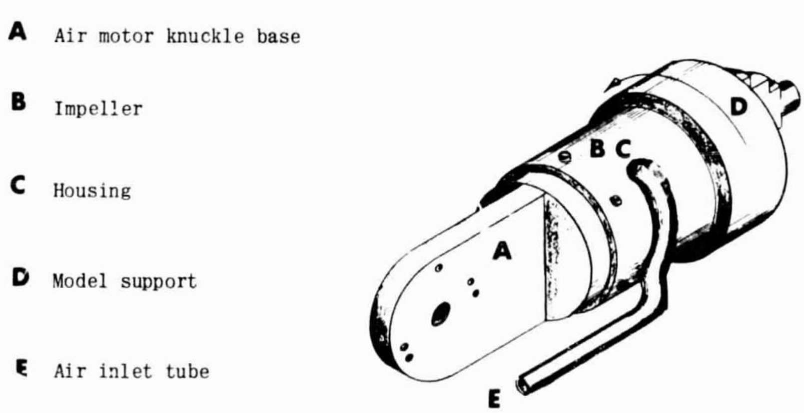

(b) Schematic of air motor

Ref. 48

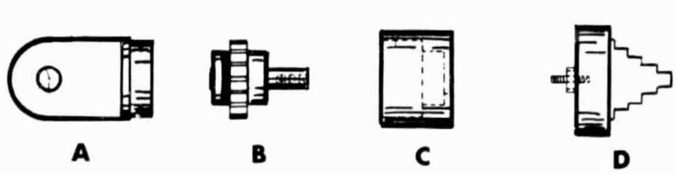

Fig. 36 Launcher for spinning models

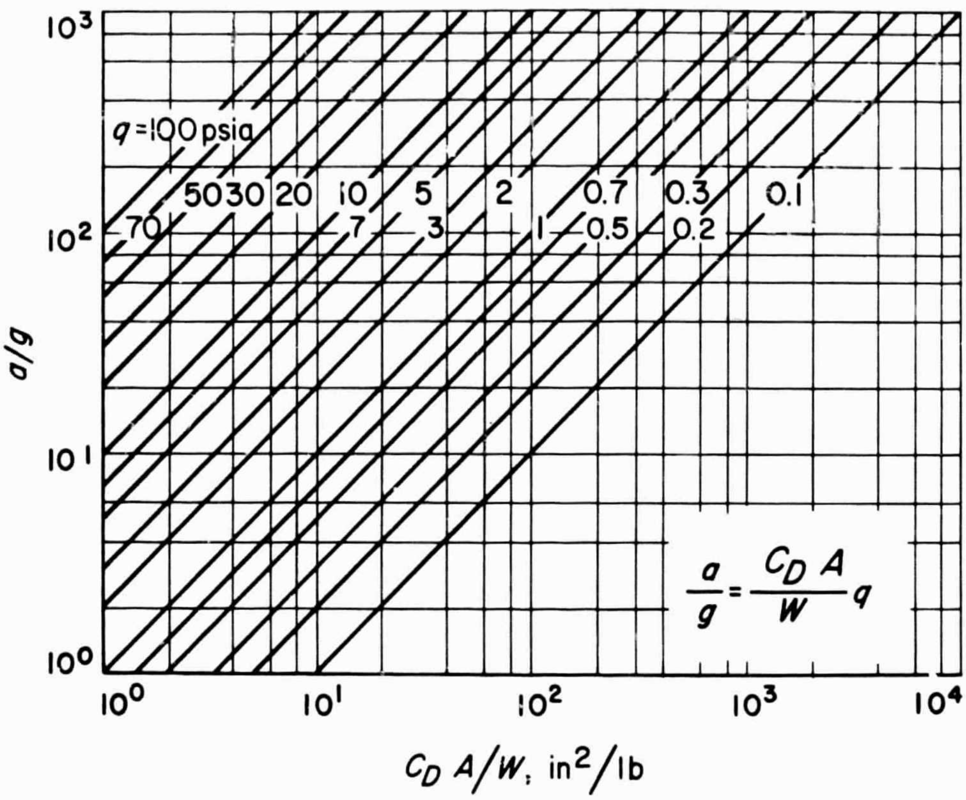

Fig. 37   Model acceleration versus ballistic coefficient

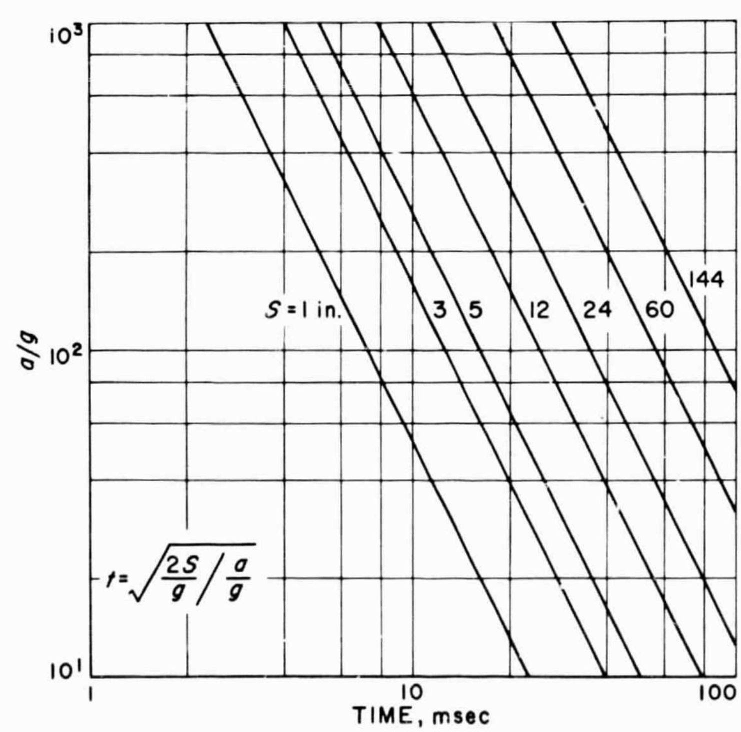

Fig. 38   Time for model to travel various distances

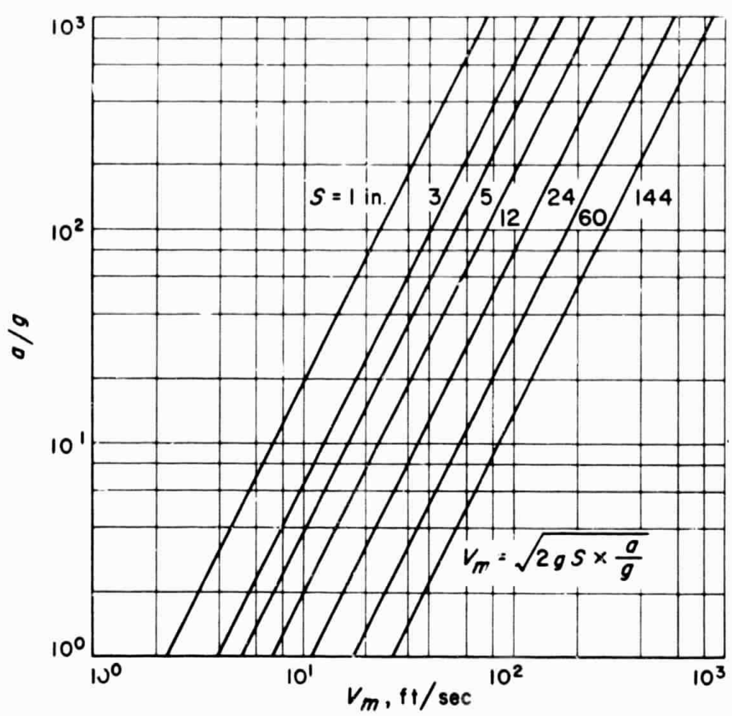

Fig. 39 Model velocity after traveling various distances

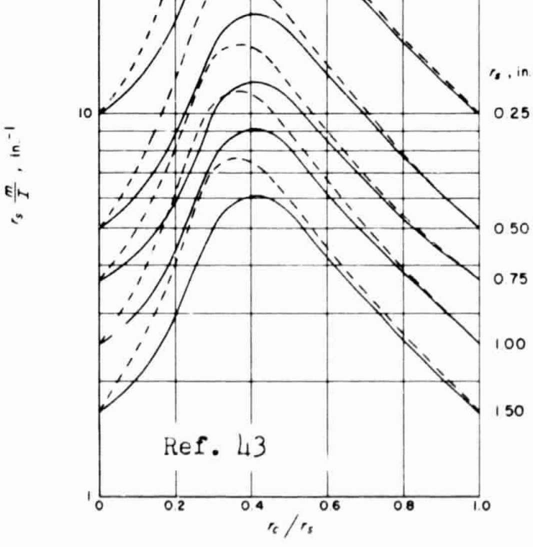

Fig. 40 The ratio $r_s m/I$ versus r_c/r_s for a spherical model

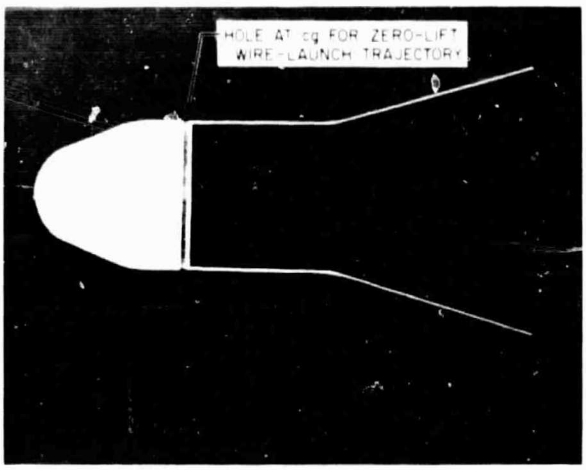

(a) Hollowed-out Aluminum model
(d_{cyl} = 1 in.)

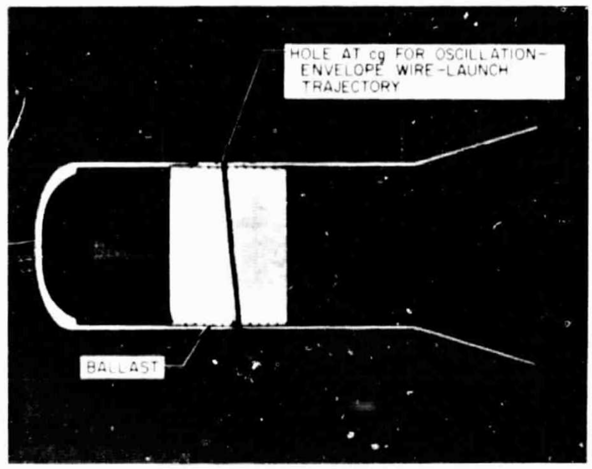

(b) Hollowed-out Magnesium model
ballasted with Copper slug
(d_{cyl} = 1.1 in.)

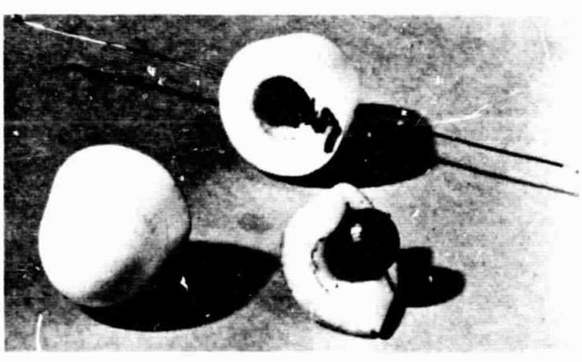

(c) Cast foam model ballasted with
0.45 in. D Lead sphere
(d_B = 1 in.)

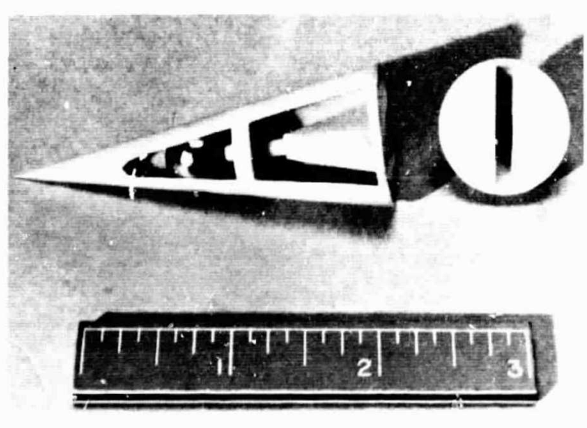

(d) Molded Plastic model ballasted with
0.45 in. D Lead sphere
(d_B = 1 in.)

Ref. 28

Fig. 41 Examples of model construction techniques

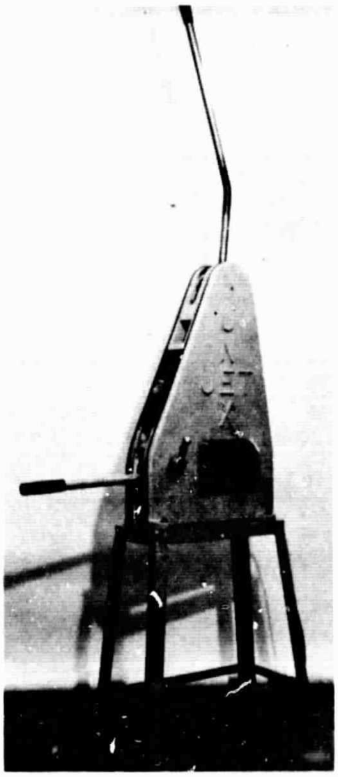

Ref. 45

Small (3/4 oz Capacity)

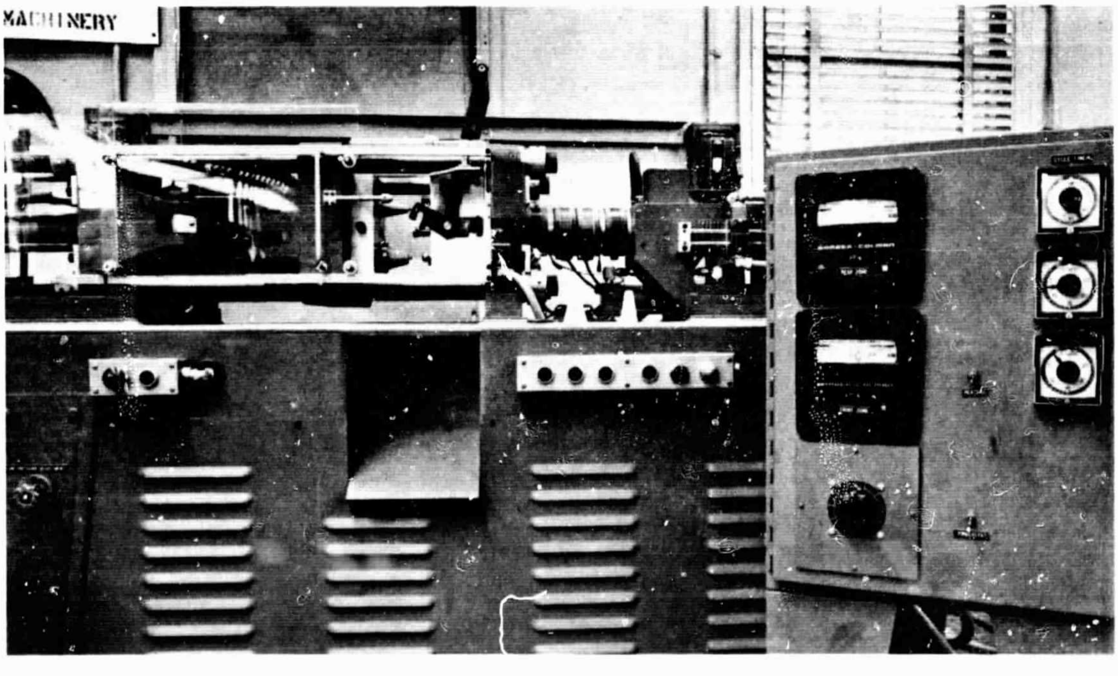

Large (3 oz Capacity)

Fig. 42 Injection molding presses

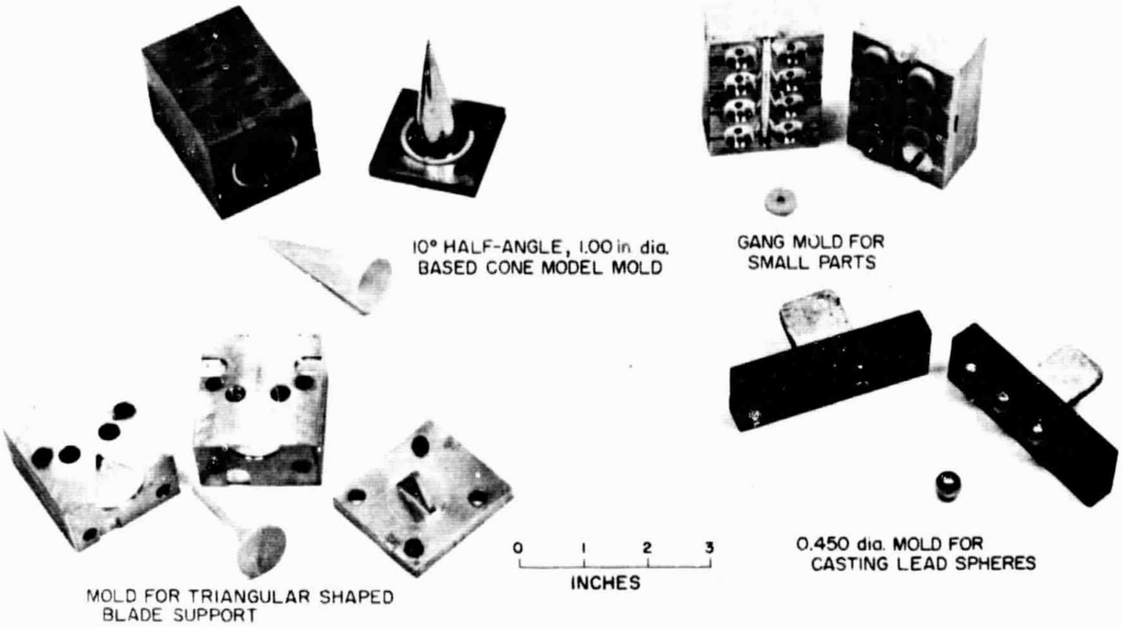

Ref. 45

Fig. 43 Typical polystyrene model molding dies

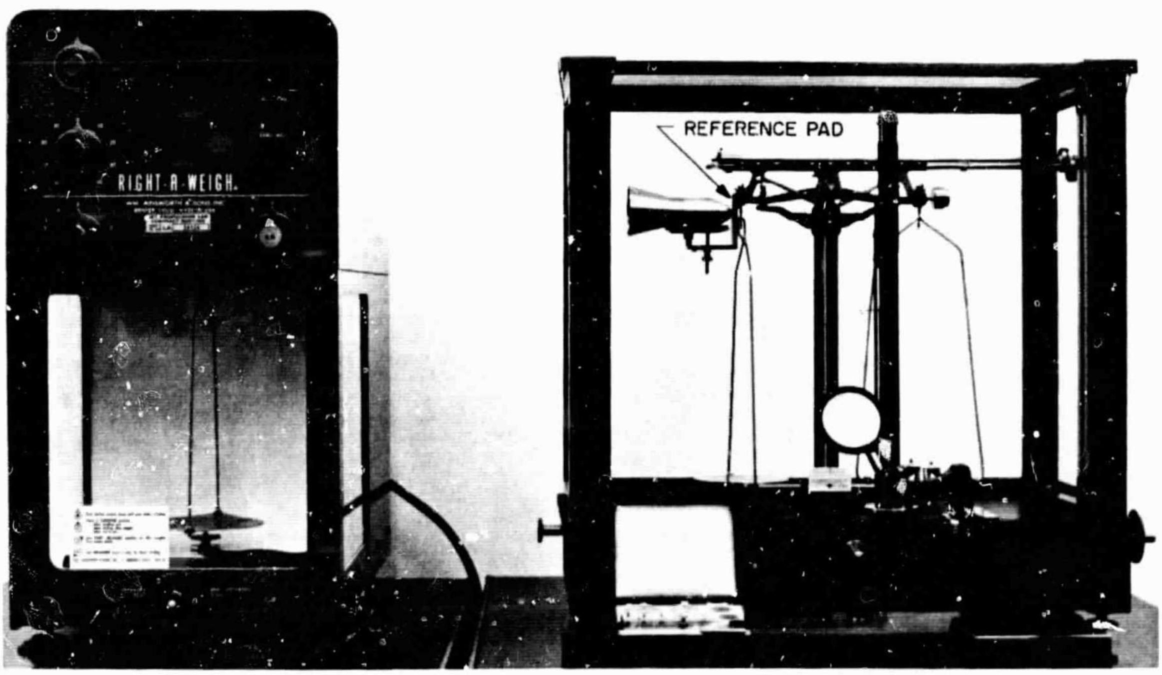

Ref. 45

Fig. 44 Analytical balances for locating the center of gravity

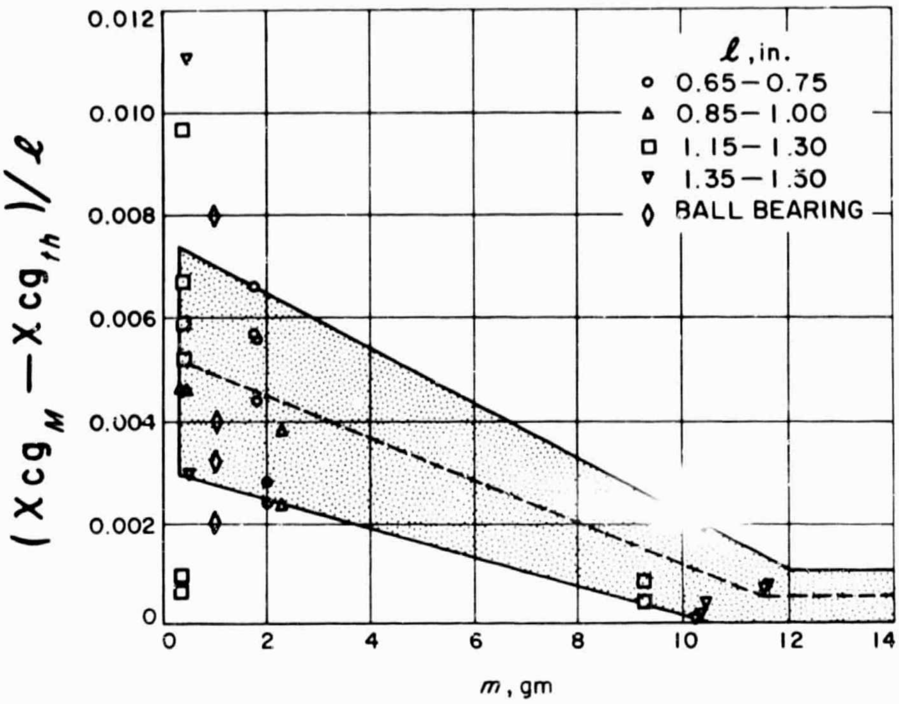

Fig. 45 Center-of-gravity measurement errors for constant cross-section calibration models

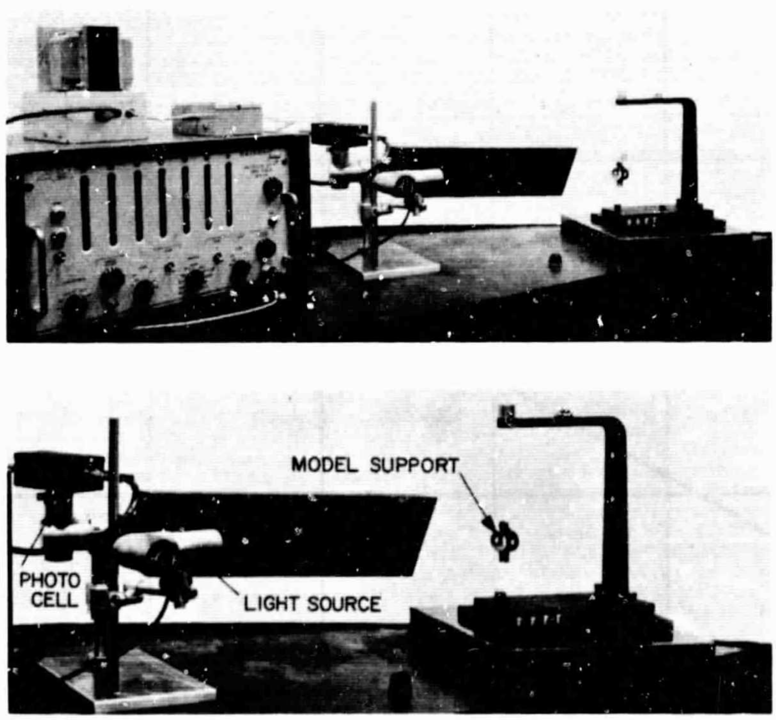

Ref. 45

Fig. 46 Instrument for measuring model moment of inertia

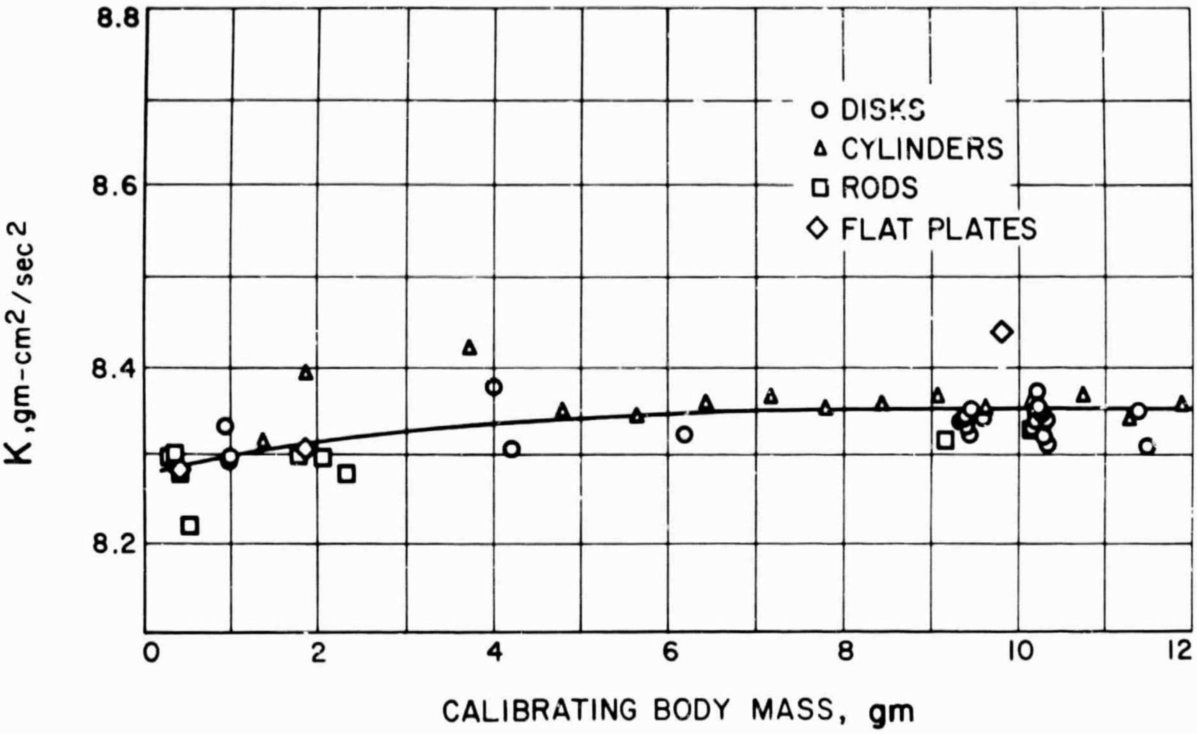

Fig. 47 Wire torsional constant calibration for moment of inertia measurements

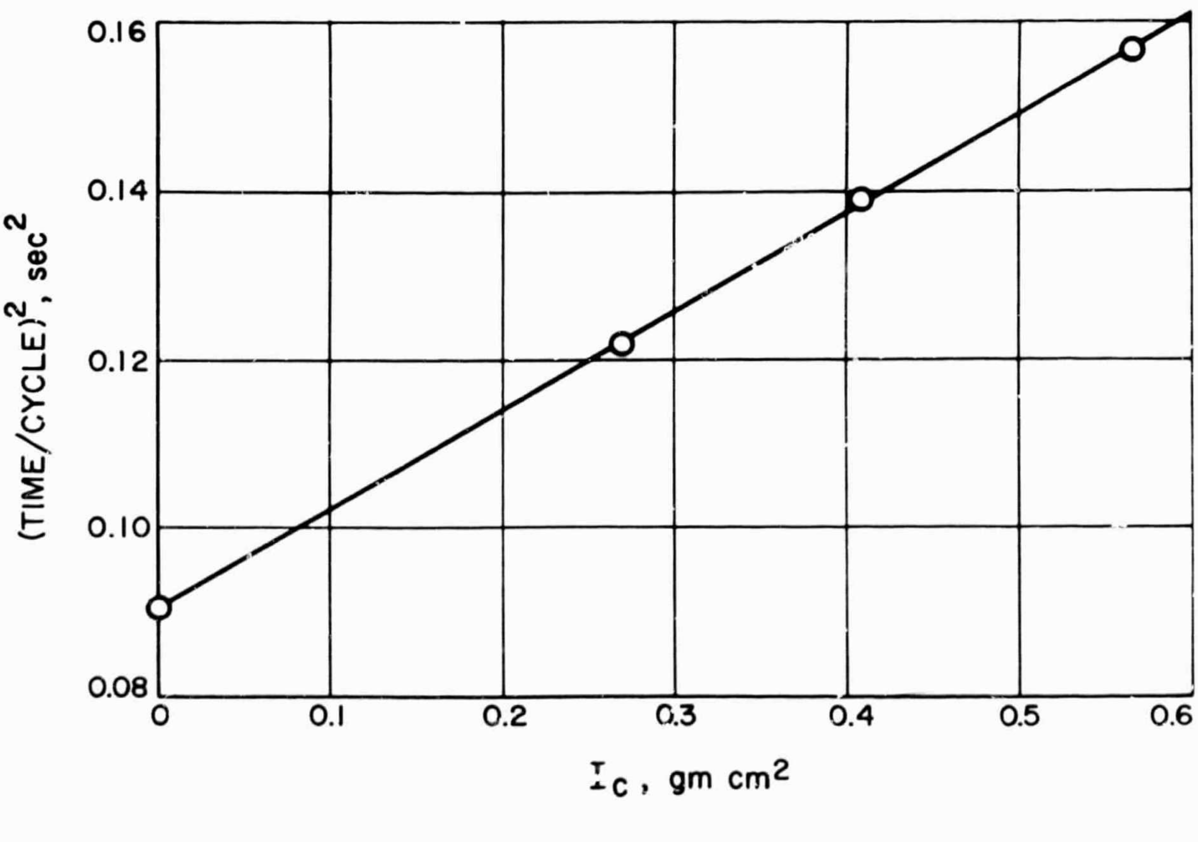

Fig. 48 Typical moment of inertia calibration for heavy models

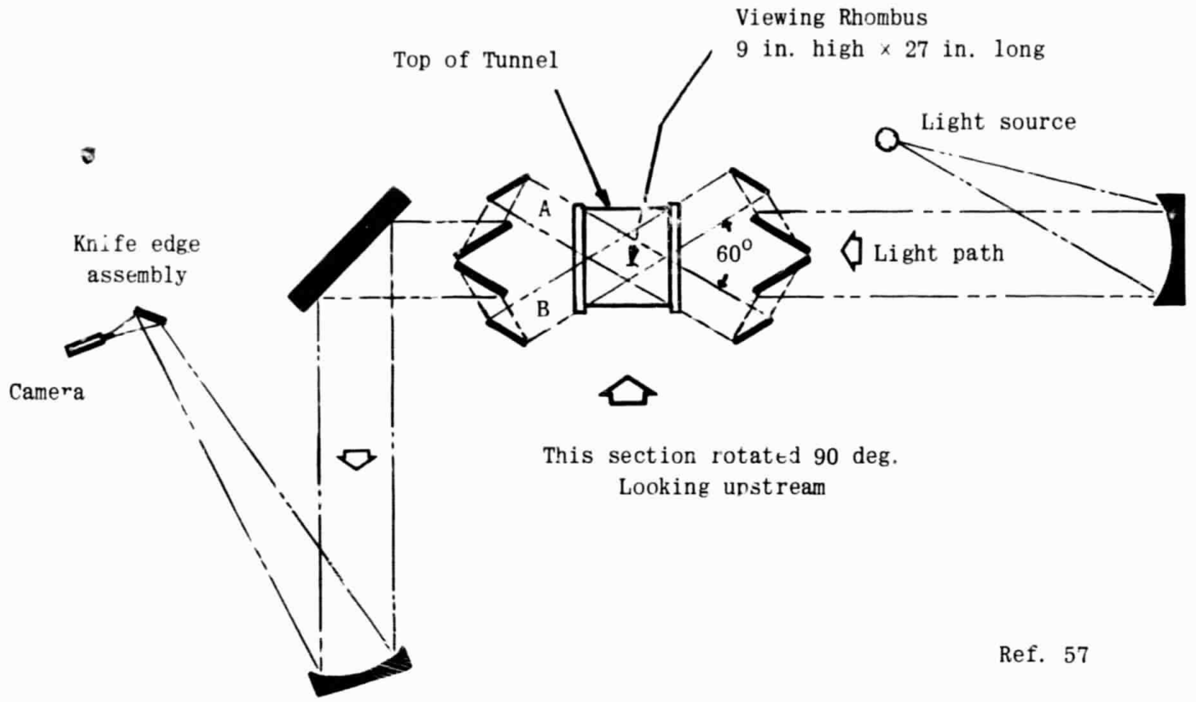

Fig. 49 Optical system for viewing non-planar free-flight motion

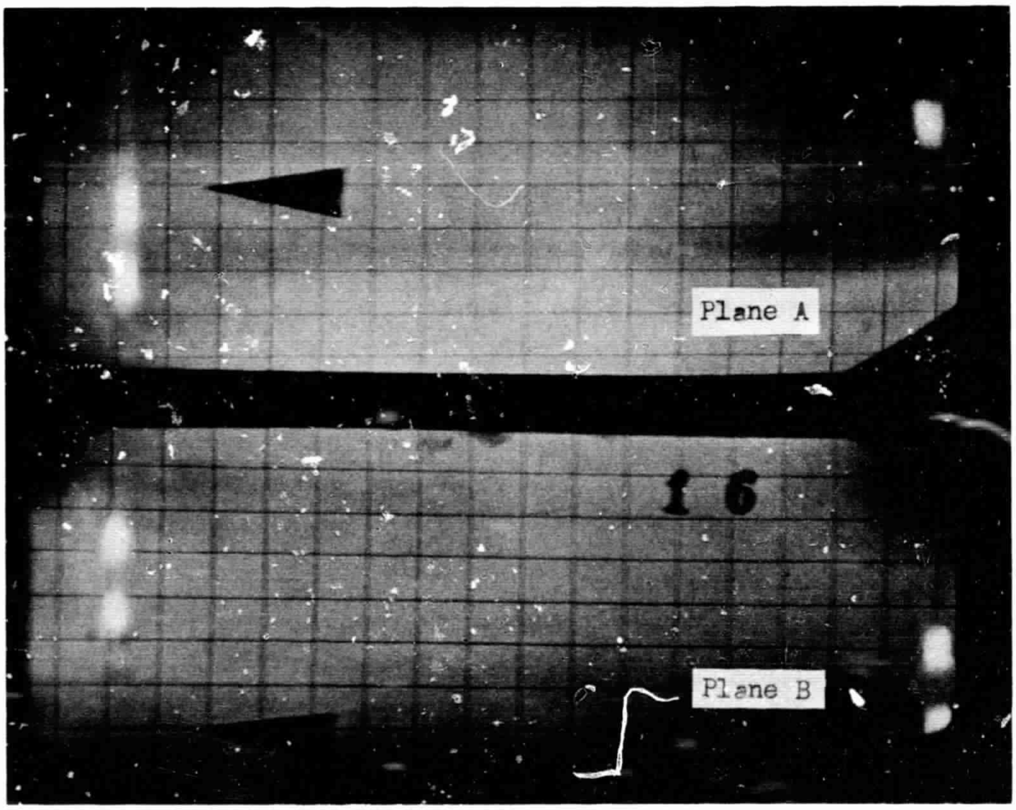

Fig. 50 Example of model photo using non-orthogonal two-plane optical system

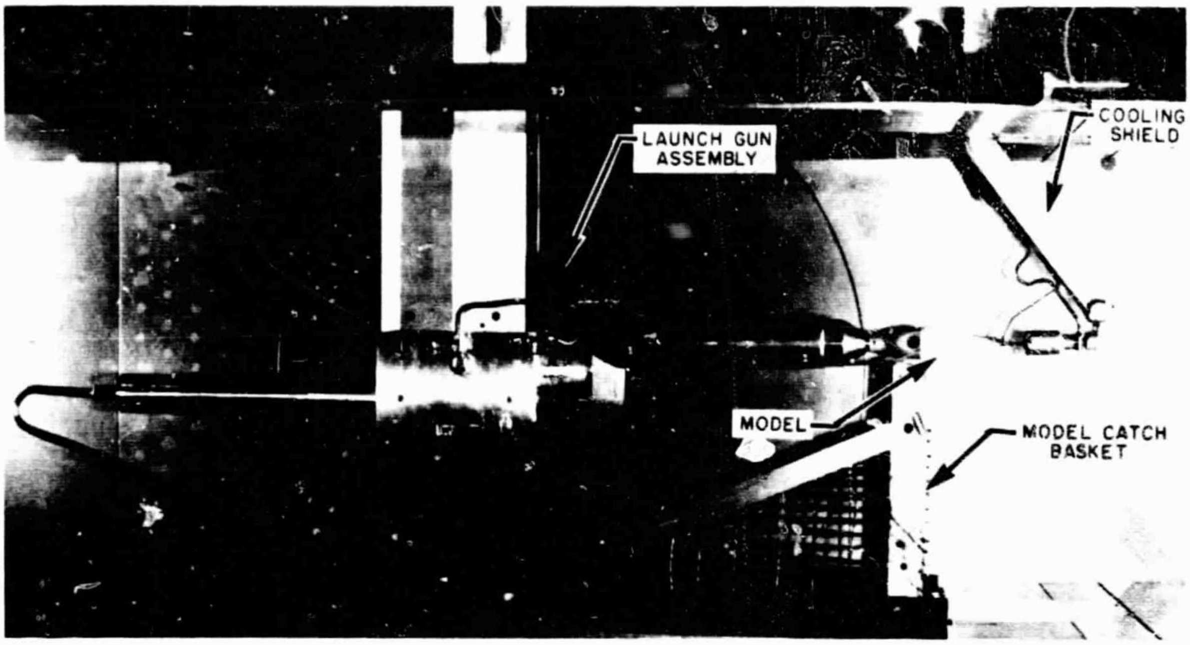

Complete Installation

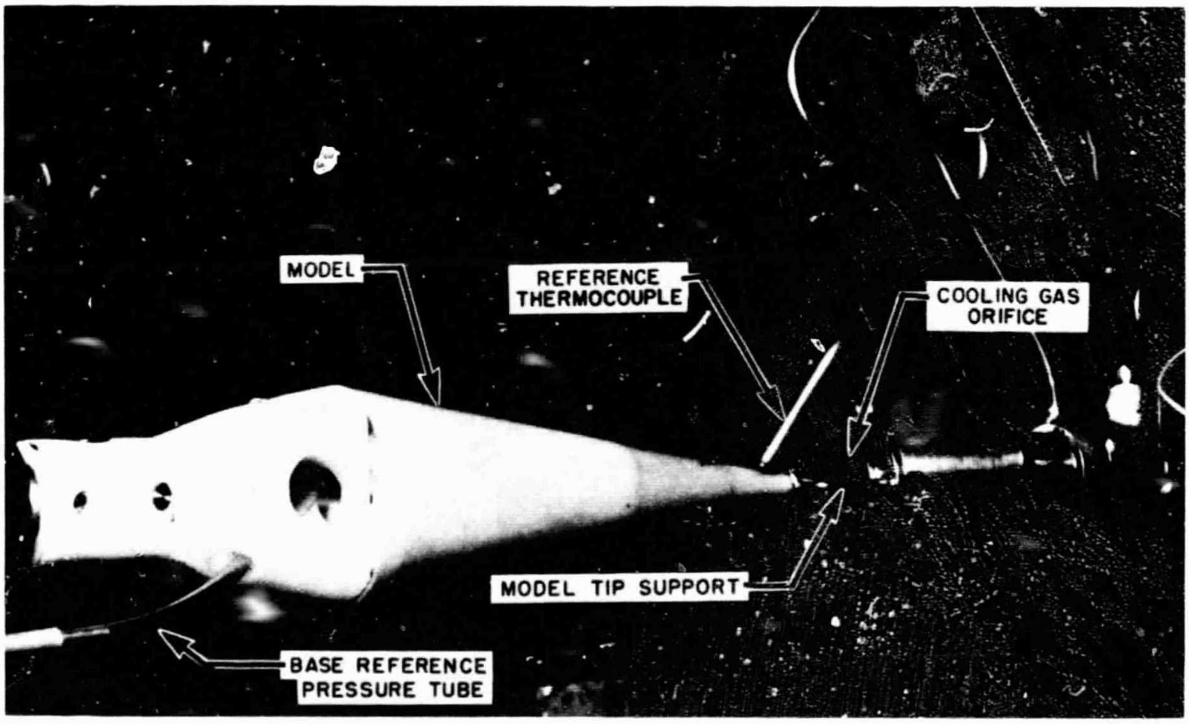

Close-up of Model Region

Ref. 38

Fig. 51 Gun-launch installation for base pressure telemetry model

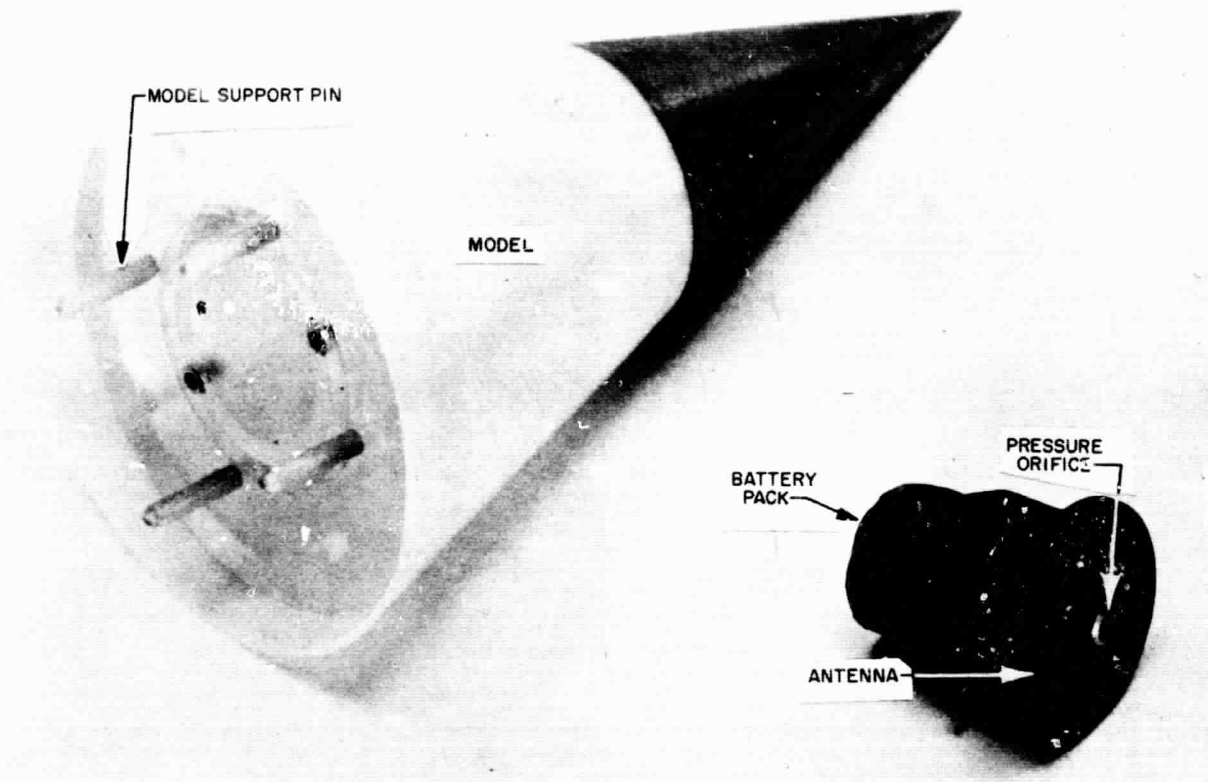

TELEMETRY PACKAGE

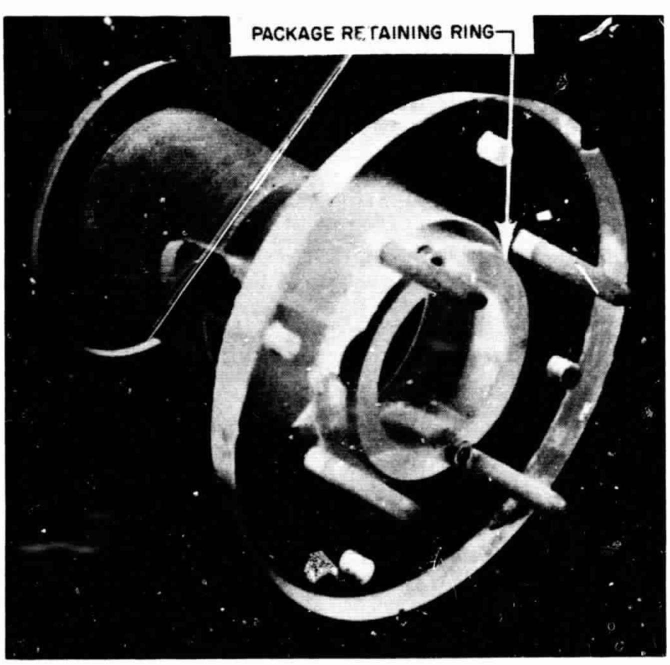

TELEMETRY PACKAGE HOLDER

Fig. 52 Free-flight base pressure telemetry package

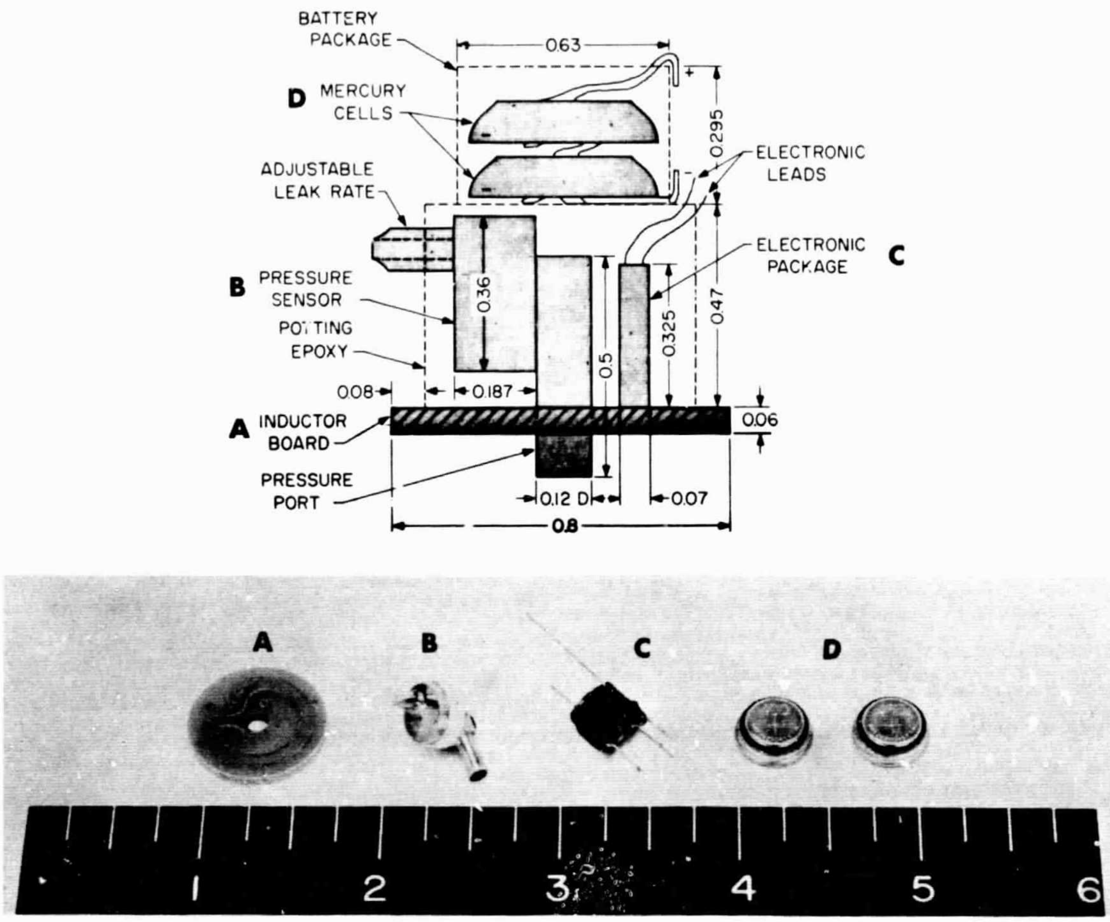

(a) Pressure telemetry components layout

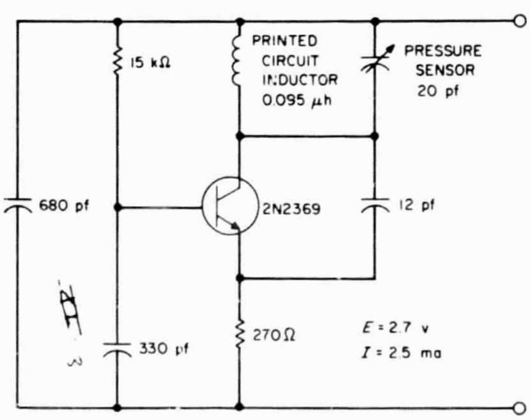

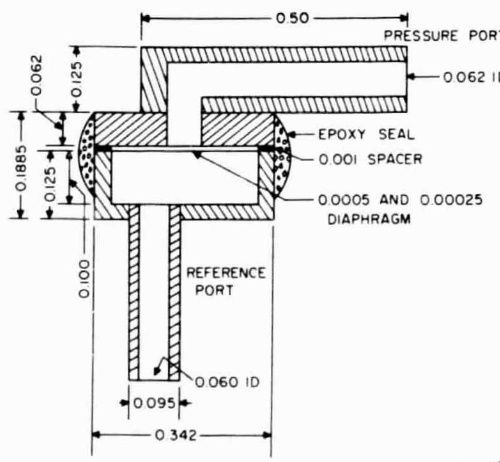

Ref. 58

(b) Schematic diagram of telemetry oscillator

(c) Pressure sensor

Fig. 53 Details of pressure telemetry system

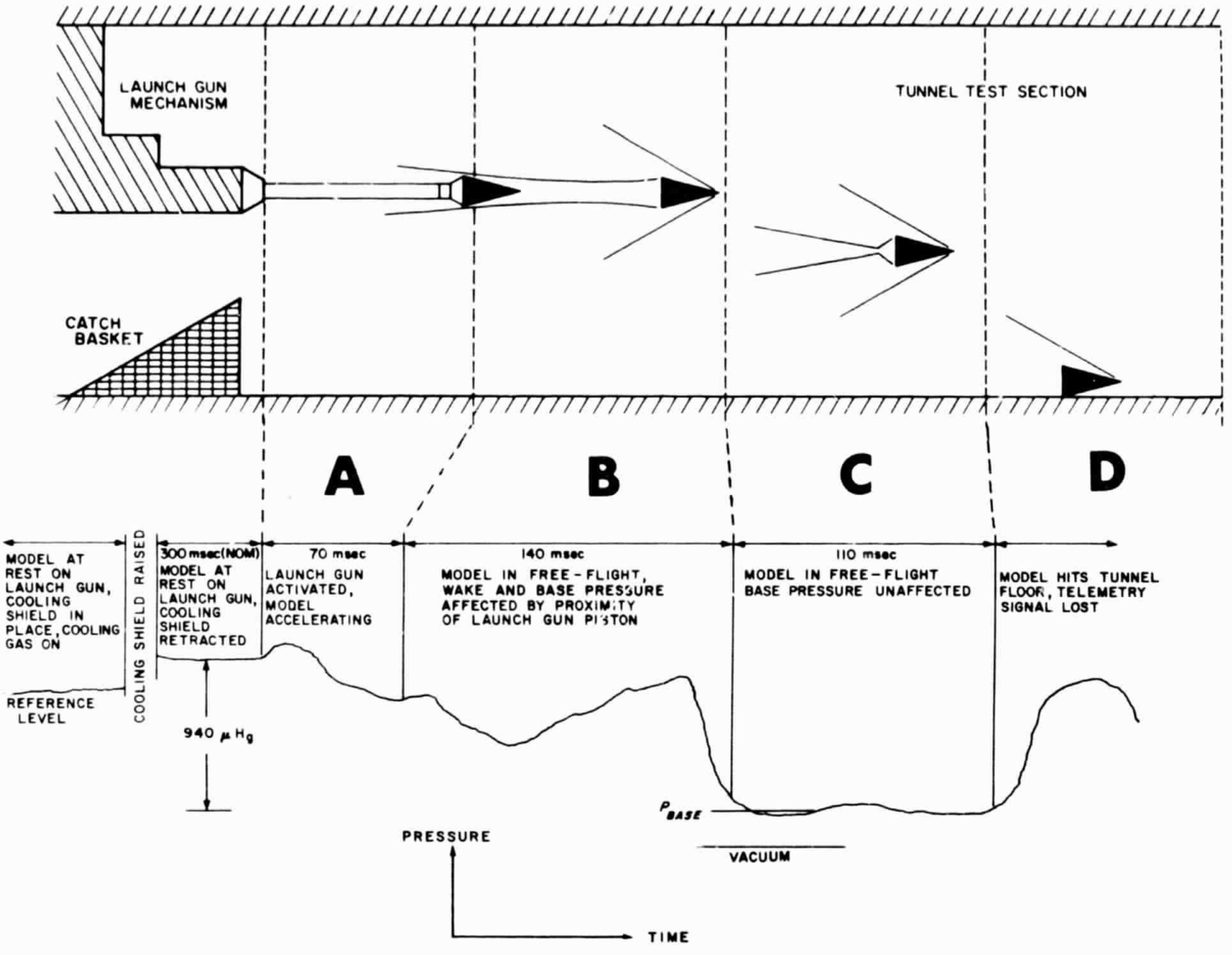

A. PISTON ACCELERATING MODEL

B. MODEL IN FREE FLIGHT, WAKE SEPARATED BY PISTON

C. MODEL IN FREE FLIGHT, WAKE UNINFLUENCED BY PISTON

D. MODEL ENTERS BOUNDARY LAYER AND STRIKES FLOOR

Ref. 38

Fig. 54 Telemetry pressure data curve with corresponding model flight position

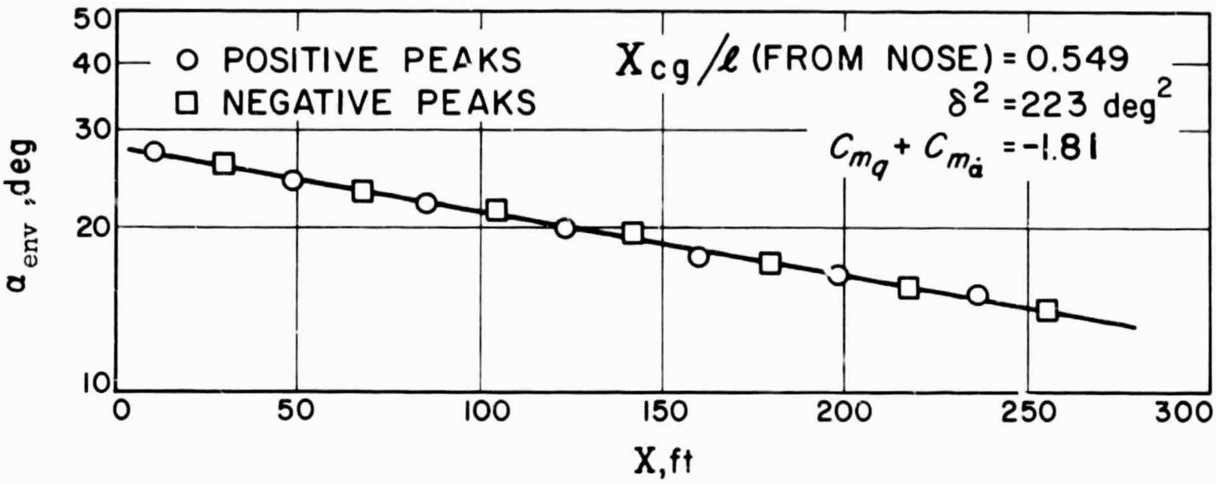

Fig. 55 Cone amplitudes for decaying oscillatory motion

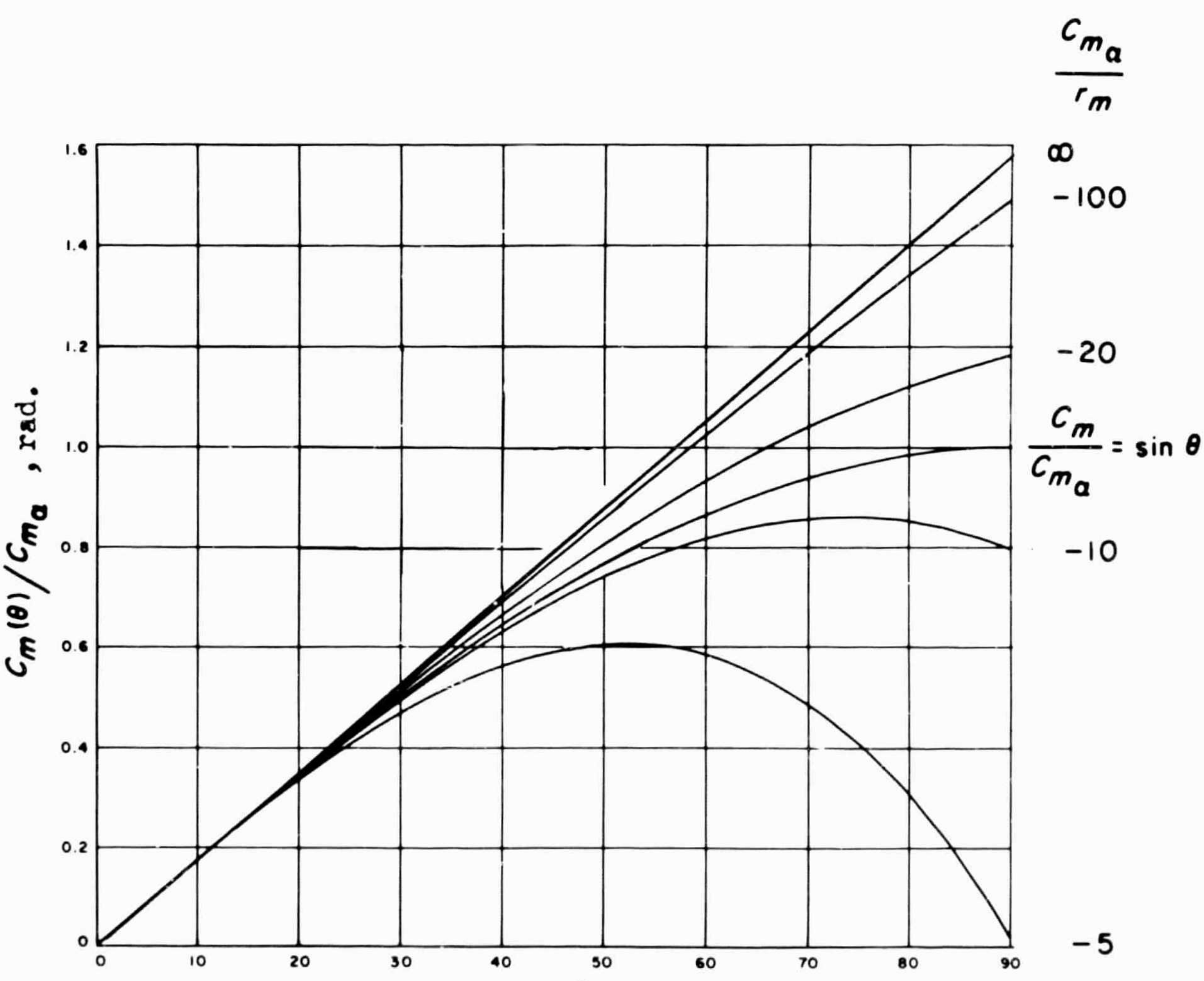

Fig. 56 Shapes of cubic pitching moment curves

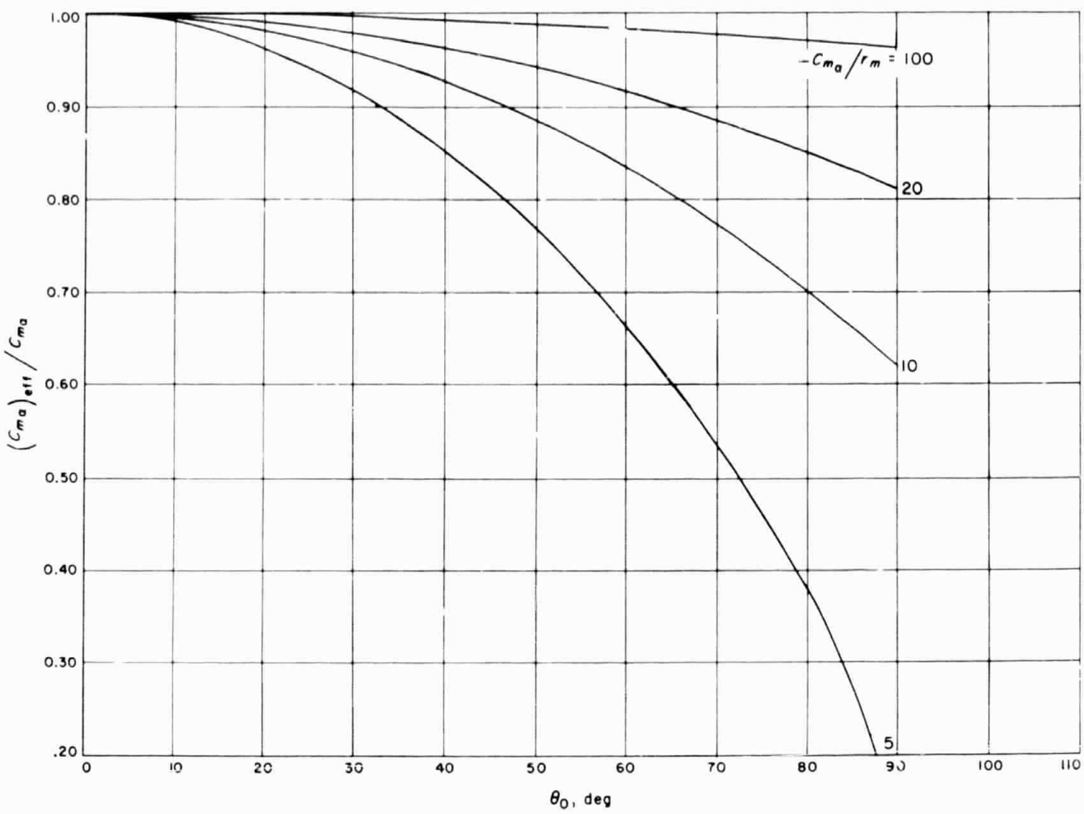

Fig. 57 $(C_{m\alpha})_{eff}/C_{m\alpha 0}$ versus θ_0 with varying $C_{m\alpha}/r_m$

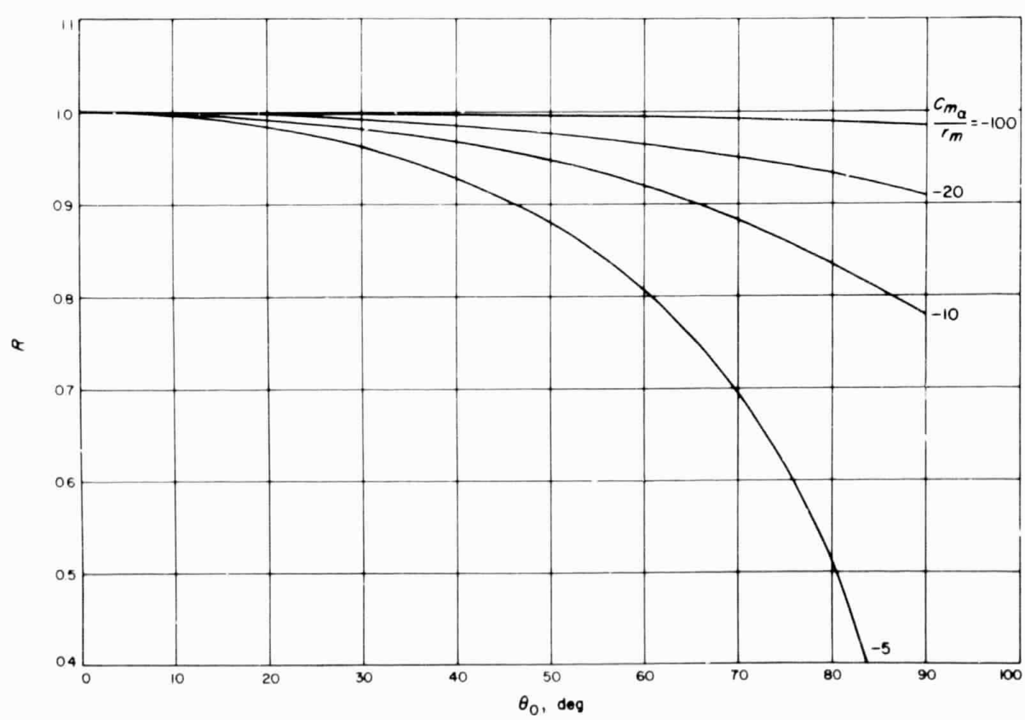

Fig. 58 Correction factor for effect of non-linear pitching moment on dynamic stability data reduction

DISTRIBUTION

Copies of AGARD publications may be obtained in the various countries at the addresses given below.

On peut se procurer des exemplaires des publications de l'AGARD aux adresses suivantes.

BELGIUM BELGIQUE	Centre National d'Etudes et de Recherches Aéronautiques 11, rue d'Egmont, Bruxelles
CANADA	Director of Scientific Information Service Defence Research Board Department of National Defence 'A' Building, Ottawa, Ontario
DENMARK DANEMARK	Danish Defence Research Board Østerbrogades Kaserne, Copenhagen, Ø
FRANCE	O.N.E.R.A. (Direction) 25, Av. de la Division Leclerc Châtillon-sous-Bagneux (Seine)
GERMANY ALLEMAGNE	Zentralistelle für Luftfahrtdokumentation und Information 8 Munchen 27 Maria-Theresia-Str. 21 Attn: Dr. H.J. Rautenberg
GREECE GRECE	Greek National Defence General Staff B.JSG, Athens
ICELAND ISLANDE	Director of Aviation c/o Flugrad, Reykjavik
ITALY ITALIE	Ufficio del Delegato Nazionale all'AGARD Ministero Difesa - Aeronautica Roma
LUXEMBURG LUXEMBOURG	Obtainable through Belgium
NETHERLANDS PAYS BAS	Netherlands Delegation to AGARD Kluyverweg 1, Delft

NORWAY NORVEGE	Norwegian Defence Research Establishment Kjeller per Lilleström Attn: Mr. O. Blichner
PORTUGAL	Delegado Nacional do 'AGARD' Direcção do Serviço de Material da Forca Aerea Rua da Escola Politecnica, 42 Lisboa
TURKEY TURQUIE	Ministry of National Defence Ankara Attn: AGARD National Delegate
UNITED KINGDOM ROYAUME UNI	Ministry of Aviation T.I.L.1, Block A, Station Square House, St.Mary Cray, Orpington, Kent
UNITED STATES ETATS UNIS	National Aeronautics and Space Administration (NASA) Washington, D.C. 20546

Printed by Technical Editing and Reproduction Ltd
Harford House, 7-9 Charlotte St. London. W.1.